# The Interplay of Surface Composition, Mineralogy, and Physical Conditions That Affect the Surface Release Processes and Particle Environment of Mercury

Peter Wurz[1] , Noah Jäggi[1] , André Galli[1] , Audrey Vorburger[1] , Deborah Domingue[2] , Paul S. Szabo[3] ,
Johannes Benkhoff[4] , Océane Barraud[5] , and Daniel Wolf Savin[6]

[1] Space Science and Planetology, Physics Institute, University of Bern, Bern, Switzerland
[2] Planetary Science Institute, Tucson, AZ, USA
[3] Space Sciences Laboratory, University of California, Berkeley, CA, USA
[4] ESA/ESTEC, Noordwijk, The Netherlands
[5] German Aerospace Center (DLR)—Institute of Planetary Research, 12489 Berlin, Germany
[6] Columbia Astrophysics Laboratory, Columbia University, New York, NY 10027, USA

## Abstract

Mercury has a very tenuous atmosphere starting at the surface, which is referred to as a surface-bound exosphere, where there are no collisions between exospheric particles. Having a surface-bound exosphere means that the particles in the exosphere have their origin on Mercury's surface; thus, the composition of the exosphere is connected to the composition of the surface. In situ composition measurements of the exosphere can contribute to the study of the composition of the surface, together with a range of remote sensing techniques (ultraviolet, visible, infrared, X-ray, gamma-ray, and neutron spectroscopy). The external drivers for the particle release from the surface are solar photons, solar wind plasma, and micrometeoroid impacts. These drivers also cause space weathering of the surface, resulting in significant physical and chemical alterations in the regolith, ranging from the very surface to depths up to one meter. Modifications of the surface by space weathering must be considered when interpreting the composition measurements of the exosphere as well as the composition measurements of the surface by the established remote sensing techniques, because their information comes from the space-weathered volume of the surface. Therefore, the particle populations in the exosphere, space weathering, and the composition of the surface are intimately connected and must be studied together. In the following, we will review the connections between the surface and the exosphere of Mercury.

*Unified Astronomy Thesaurus concepts:* Planetary atmospheres (1244); Planetary science (1255)

## 1. Introduction

The planet Mercury, like the Moon, is perceived as a rocky body without any atmosphere. However, Mercury does have a tenuous atmosphere, which is referred to as an exosphere. The pressure at Mercury's surface is approximately $10^{-10}$ mbar, as determined by the Mariner 10 occultation experiment (G. Fjelbo et al. 1976; D. M. Hunten et al. 1988). The eleven elements observed to date in Mercury's exosphere (H, He, O, Na, K, Ca, Mg, Al, Ar, Fe, and Mn) probably constitute only a fraction of Mercury's exosphere because at the surface the total pressure from the sum of these known species is almost 2 orders of magnitudes less than the upper limit for the exospheric pressure of $10^{-10}$ mbar based on Mariner 10 observations (G. Fjelbo et al. 1976; D. M. Hunten et al. 1988; P. Wurz & H. Lammer 2003; A. Milillo et al. 2005; W. E. McClintock et al. 2008; P. Wurz et al. 2010). From measurements of ions in Mercury's environment, the presence of some volatile molecular species in the exosphere (e.g., $H_2$, OH, $H_2O$, $O_2$, and $CO_2$) can be inferred (P. Wurz et al. 2019). Our present understanding of Mercury is mostly due to the MErcury Surface, Space ENvironment, GEochemistry, and Ranging (MESSENGER) mission (S. C. Solomon et al. 2001).

The exobase, the boundary to the thicker atmosphere, is defined as the height above the surface at which upward-traveling molecules experience one collision on average, which means that at this position the mean free path of a molecule is equal to one pressure scale height. At Mercury, at the Moon, and at many planetary bodies, this means that the surface is above the exobase, and we have a surface-bound exosphere. In an exosphere, the particles are moving collision free, on ballistic trajectories, rather than participating in a collision-dominated thermal motion, as in denser lower regions of atmospheres.

There are several processes that release particles from the surface. These include ion, electron, and photon irradiation of the surface, micrometeoroid impact vaporization, and thermal release (including sublimation). These release processes from the surface and subsequent loss processes from the exosphere have been reviewed in detail before (P. Wurz et al. 2022). The exospheric particles released from the surface either fall back to the surface or they are lost to space. Typical lifetimes of exospheric particles are in the approximate range from 100 to 1000 s. Part of the exospheric loss is via ionization, mostly by solar photons; these ions become an important part of the ion population in Mercury's magnetosphere or become pickup ions in the solar wind plasma. The exosphere must be replenished continuously, as there are hardly any permanent gases in it (R. M. Killen & W.-H. Ip 1999; P. Wurz & H. Lammer 2003).

Because Mercury's exosphere is surface bound, the origin of the exospheric species is either from the very surface via a range of release processes or via diffusion of species from the interior to the surface and thermal release. Implanted solar wind, mostly hydrogen and helium, will also contribute to the

exosphere via diffusion (H. Lammer et al. 2022). Thus, there is a direct link between the composition of the exosphere and the elemental and mineralogical composition of the surface. By knowing the elemental and mineralogical composition of the surface, we can predict the composition of the exosphere, or vice versa, by measuring the composition of the exosphere, we can derive information on the composition of the surface and constrain its mineralogy (P. Wurz et al. 2010). Given the scarcity of data on Mercury's surface before the MESSENGER mission, the latter approach has been performed to obtain a global mineralogy of Mercury's surface based on end-member minerals (P. Wurz et al. 2010). Given the abundance of MESSENGER observations, we will review the available data to establish the present understanding of the chemical and mineralogical composition of the surface as input for the chemical composition of the exosphere.

There were several instruments on the MESSENGER spacecraft that contributed to the investigation of the chemical and mineralogical composition of the surface. The Mercury Dual Imaging System (MDIS; S. E. Hawkins et al. 2007) had multispectral wide- and narrow-angle cameras to observe landforms and spectral variations on Mercury's surface in monochrome, color, and stereo. MDIS had 11 different filters and monochrome across the wavelength range from 395 to 1040 nm covering the visible through near-infrared spectral range. The Visible and Infrared Spectrograph (VIRS) of the Mercury Atmospheric and Surface Composition Spectrometer (MASCS; W. E. McClintock et al. 2007) had two wavelength bands of 300–1050 nm and 850–1450 nm. The VIRS measured the reflected visible and near-infrared light at wavelengths diagnostic of iron- and titanium-bearing silicate materials on the surface, such as pyroxene, olivine, and ilmenite. The Gamma-Ray and Neutron Spectrometer (GRNS; J. O. Goldsten et al. 2007) instrument packaged separate gamma-ray spectrometers (GRS) and neutron spectrometers (NS) to collect complementary data on elements that form Mercury's crust. GRS measured gamma-ray emissions in the energy range of 0.1–10 MeV that are emitted by the nuclei of atoms on Mercury's surface that were struck by cosmic rays. GRS recorded geologically important elements such as hydrogen, magnesium, silicon, oxygen, iron, titanium, sodium, and calcium, and naturally radioactive elements such as potassium, thorium, and uranium. NS mapped variations in the flux of fast, thermal, and epithermal neutrons in the energy range from thermal to about 7 MeV emitted from Mercury's surface when struck by cosmic rays. From NS data, the amount of hydrogen in the surface is inferred, which is likely in the form of water molecules and carbon, and other possible trace amounts of Gd, Sm, Fe, and Ti (D. J. Lawrence et al. 2010). The X-Ray Spectrometer (XRS; C. E. Schlemm et al. 2007) mapped the elements on the surface of Mercury by recording the X-ray fluorescence emissions in the 1–10 keV energy range coming from Mercury's surface after solar X-rays hit the surface. The XRS detected X-ray emissions from the elements magnesium, aluminum, silicon, sulfur, calcium, titanium, and iron. The Ultraviolet and Visible Spectrometer (UVVS) of the MASCS recorded UV spectra in three wavelength bands at ultraviolet (115–180 nm), middle ultraviolet (160–320 nm), and visible (250–60 nm) wavelengths. The UVVS determined the composition and structure of Mercury's exosphere from optical emissions of neutral gas and ions in the exosphere. These particles originate from the surface and thus carry some information on its chemical composition.

To determine the chemical and mineralogical composition of the surface, measurements from these instruments are considered. However, these instruments collect information from different depths below the surface, which must be taken into account when comparing their observations.

Sputtering by ion impact (e.g., precipitating solar wind ions, magnetospheric ions) promotes all species present on the surface in a stoichiometric manner into the exosphere; therefore, measuring the composition of sputtered atoms and ions in the exosphere provides important information for the study of the composition of the surface (P. Wurz et al. 2022). Sputtering releases atoms and polyatomic species from the topmost two to three atomic layers of the surface (R. Behrisch & W. Eckstein 2007). Thus, the part of the exosphere resulting from ion-induced sputtering provides information on the elemental composition of the topmost atomic layers of the surface. However, the penetration range of the impacting solar wind ions extends to larger depths, to about 30 nm for protons and alpha particles, contributing significantly to space weathering on these scales (C. M. Pieters & S. K. Noble 2016). For energetic protons of a few MeV, the penetration depth is 0.1 mm. Although particles at these energies do not cause particle release into the exosphere (P. Wurz et al. 2022), they cause space weathering of the surfaces of exposed grains.

Spectroscopy in the visible and infrared spectral regions can be used for the investigation of the mineralogy of the surface. The reflected light in this wavelength range contains information on electronic and vibration states of the minerals; thus, these spectra can be used to infer the mineralogy of the surface with the help of reference spectra of minerals (Section 2.2). For example, pyroxene, olivine, and plagioclase have electronic transitions resulting in absorption bands near 1 and 2 $\mu$m. The information depth of infrared spectroscopy is given by the penetration depth of the radiation into the solid, which is of the order of the wavelength of the reflected light.

The XRS instrument technique is reliant on X-rays emitted from the solar corona that excite electrons in atoms on or very near the surface, within the top few tens of micrometers (L. R. Nittler et al. 2020). Upon the return of an atom to a stable energetic state, a fluorescent X-ray is emitted, with a characteristic energy indicative of the element. Thus, the XRS mapped the element abundances in the top millimeter of Mercury's surface.

Gamma rays observed by GRS are from the decay of radioactive nuclei. They are produced by natural radioactive decay and by Galactic cosmic rays, although the majority of gamma rays emitted from planetary surfaces are produced by the interaction of Galactic cosmic radiation. Gamma rays are formed at depths up to where Galactic cosmic-ray particles are completely stopped, which is up to about one meter. Gamma-ray production in the surface material and their attenuation leaving to free space are dependent on the gamma-ray energy, material density, average atomic number $Z$ of the surface, and the presence of neutron moderators and absorbers. The effective depth from which measurable gamma rays are emitted covers only a few decimeters (P. A. J. Englert 2011).

Galactic cosmic rays absorbed in the surface also cause the production of neutrons, which are measured by the NS. The observed fast neutrons (500 keV to about 7 MeV) were emitted directly into space; other fast neutrons collided with
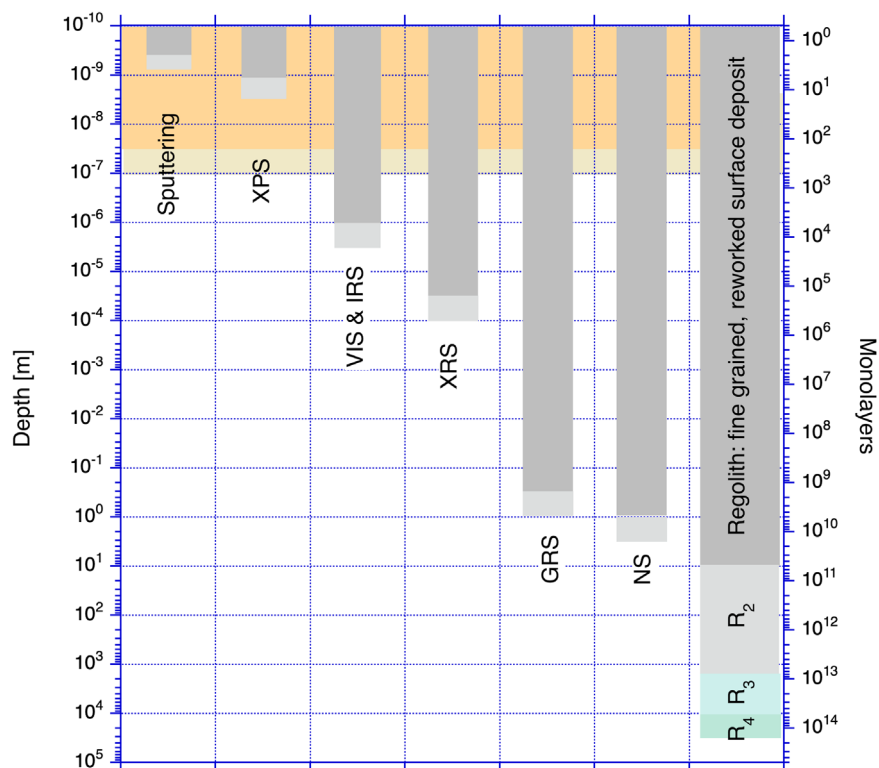
**Figure 1.** Overview of the depth of information for the various techniques used to infer the chemical and mineralogical composition of Mercury's surface together with the approximate structure of the regolith. Sputtering refers to the release of particles from the surface via ion sputtering, XPS is X-ray photo-electron spectroscopy (not used in the MESSENGER mission, but potentially on a future mission), VIS & IRS is the visible and infrared spectroscopy of reflected light, XRS is X-ray spectroscopy, GRS is gamma-ray spectroscopy, and NS is neutron spectrometry. The dark-gray bars give the typical information scale of the technique and the light-gray bars the possible maximum range. The last column gives the approximate vertical structure of the lunar surface (G. H. Heiken et al. 1991), which is expected to be similar on Mercury (A. Y. Zharkova et al. 2020). The regolith sits on top of large-scale ejecta ($R_2$), a structurally disturbed crust ($R_3$), and a fractured crust ($R_4$). The orange background indicates the typical range of space weathering of 30 nm and its maximal extent to about 100 nm depth.

neighboring atoms in the surface material before escaping. If a neutron collides with a light atom (like hydrogen), it loses energy and is detected as a thermal (0.025–1 eV) neutron or epithermal neutron (1 eV to about 500 keV). The ratio of thermal to epithermal neutrons across Mercury's surface is used to estimate the amount of hydrogen (the most likely moderator) or carbon (also a possible moderator), and other elements (J. O. Goldsten et al. 2007). Hydrogen is possibly locked up in water molecules; thus, the neutron maps are interpreted as water contained in the subsurface. From modeling cosmic-ray-induced neutron emission and its transport through the lunar regolith, it was found that the resulting information depth is mostly from the top meter (R. C. Little et al. 2003).

Figure 1 shows the different techniques with which the chemical and mineralogical composition of the surface is investigated. Each technique presents composition information from a different volume under the surface. Sputtering provides composition information from the topmost atomic layers of the surface, whereas the GRS sample from the largest depths. Considering that the regolith grains are chemically heterogeneous on the nanometer to micrometer spatial scale, because of space weathering (C. M. Pieters & S. K. Noble 2016), and because the regolith itself is structurally heterogeneous in depth (G. H. Heiken et al. 1991; X. Zhang et al. 2021), one must be cautious when comparing measurements from different instruments. The depth range where the composition is affected significantly by space weathering, e.g., the formation of nanophase iron in the rims of grains, is 50–100 nm based on C. M. Pieters & S. K. Noble (2016), which is indicated in

Figure 1. Sputter yields and ion implantation by solar wind ion bombardment reaches saturation after a solar wind exposure of a few tens to hundred years. For example, saturation of the total sputter yield of pyroxene was accomplished after a fluence of a few $10^{21}$ ions m$^{-2}$ s$^{-1}$ of 4 keV He ions (H. Biber et al. 2020). Based on laboratory studies, spectral changes in asteroids induced by heavy solar wind ions are estimated to occur after $10^4$–$10^6$ yr (G. Strazzulla et al. 2005), and correspondingly at shorter times at Mercury. In contrast, the surface residence time of typical regolith grains on Mercury is $1.5 \cdot 10^5$ yr, e.g., a 1 cm deep layer of regolith on Mercury will be overturned with 50% probability (Y. Langevin 1997; R. M. Killen et al. 2007). E. S. Costello et al. (2018, 2020) provided a detailed calculation of regolith overturn timescales as a function of depth for Mercury and the Moon. Moreover, some atomic species that are volatile at Mercury's temperatures (e.g., Na, K, and S) and might accumulate in the top 10 cm of the regolith in colder regions at high latitudes in significant amounts, as will be discussed below, will affect the interpretation of the composition measurements, which will be discussed in more detail in Section 4.

There is a possible surface coverage of a fraction to a few monolayers (leftmost column in Figure 1) from exospheric particles falling back onto the surface and sticking to the surface. Such a process has been discussed in detail for a global Na coverage (A. Mura et al. 2009). Thermal migration of Na to colder places, in addition to a variation in composition, was used to explain the higher abundance of Na observed at higher latitudes (P. N. Peplowski et al. 2014). Substantial, and more

permanent, deposits of volatile species have been proposed for high-latitude cold regions in general (e.g., Na and K accumulation in polar areas), and especially for permanently shadowed regions (PSRs). For PSRs, substantial accumulation of water is suspected based on radar, GRS, and NS measurements (D. J. Lawrence et al. 2013; N. L. Chabot et al. 2018a).

The rightmost column in Figure 1 shows the approximate vertical structure of the lunar surface (G. H. Heiken et al. 1991), which is expected to be similar on Mercury but generally thicker (A. Y. Zharkova et al. 2020). For example, the low abundance of boulders on Mercury's surface compared to the Moon is a possible indication of a thicker regolith (M. A. Kreslavsky et al. 2021). However, the high daytime temperature on Mercury enhances and accelerates diffusive sintering of regolith particles, which likely leads to formation of an indurated, mechanically stronger uppermost regolith layer with a possible thickness of a fraction of the diurnal thermal skin thickness, that is, tens of centimeters (A. Y. Zharkova et al. 2020). However, at the level of regolith grains, the regolith of Mercury is expected to be significantly more mature than the lunar regolith, with smaller grain sizes and larger proportions of glassy particles (Y. Langevin 1997). At the Moon (G. H. Heiken et al. 1991), from the surface down to a depth of about 10 m is the regolith proper, the fine-grained, reworked surface deposit from the history of impacts, followed by large-scale ejecta (region $R_2$) down to about 2 km, which is ballistically transported material, coarse-grained, polymict ejecta, and commuted melt sheets, followed by a structurally disturbed crust ($R_3$) down to about 10 km, which is materials (mostly large blocks) displaced by subsurface movement, followed by the fractured crust ($R_4$), with decreasing density of fractures down to 25 km depth. Comparing the information depths of the different techniques with the regolith structure (Figure 1), we see that all of these techniques investigate the regolith itself, hardly probing the crust directly, since the entire lunar surface is covered by regolith. We expect the situation to be similar for Mercury's surface, as discussed above. Some chemical composition signals can come from larger depths via diffusion. On the Moon, cracks in the fractured crust reach down to about 25 km, providing pathways for the escape of volatile species from large depths (e.g., noble gases like radiogenic He and Ar) and allow for enhanced diffusion of volatile species (R. M. Killen 2002). The escaped and diffused volatiles then end up in the exosphere, where they can be observed.

## 2. The Regional Distribution of the Surface Composition and Mineralogy of Mercury

The composition of Mercury's regolith, and its variation across the surface, has been primarily constrained by the observations made by the MESSENGER spacecraft. Because of the highly elliptic orbit of the MESSENGER spacecraft, many results are limited to the northern hemisphere. MDIS and MASCS showed us a surface with an overall low ultraviolet to near-infrared albedo and a small number of spectral units, but diagnostic mineral identifications were not possible (i.e., M. S. Robinson et al. 2008; N. R. Izenberg et al. 2014; S. L. Murchie et al. 2015). The surface of Mercury is heavily altered through space-weathering processes that are known to suppress absorption features, to lower reflectance, and to increase spectral slope (redden the spectrum), thus

complicating interpretations of spectral data (B. Hapke 2001; M. S. Robinson et al. 2008).

Based on MDIS imagery, the surface of Mercury can be spectrally characterized by four major spectral units located within the smooth plains, which are a major geologic unit, and the low-reflectance material (LRM) corresponding to the darkest surface materials, and three minor spectral units (S. L. Murchie et al. 2015). The spectral units in the smooth plains include low-reflectance blue plains, intermediate plains, and high-reflectance red plains (HRP; B. W. Denevi et al. 2009; S. L. Murchie et al. 2015). The three minor spectral units are all comparatively higher in reflectance and include fresh crater materials, diffuse high albedo red spots designated as "faculae" in IAU nomenclature that are mostly interpreted as pyroclastic deposits (e.g., R. J. Thomas & D. A. Rothery 2019), and bright hollows materials (e.g., S. L. Murchie et al. 2015). Most hollows are clusters of rimless depressions with flat floors and surrounded by haloes of high albedo material; they will be discussed in Section 2.2.4. Examination of the color properties show that most of the spectral variation across Mercury's surface is related to changes in spectral slope and reflectance, falling between the two spectral end-members of HRP and LRM (S. L. Murchie et al. 2015). The darkening agents that best match these spectral variations are consistent with three possibilities (or a combination of them): (1) the presence of graphite; (2) iron or iron sulfide altered to nanophase or microphase grains by shock during impact events; or (3) iron-bearing and carbon phases in a late-accreting carbonaceous veneer mixed into the lower crust or upper mantle (S. L. Murchie et al. 2015).

The minor spectral units are correlated with morphologic or geologic units associated with Mercury's volatile inventory. However, to understand this volatile inventory, a concept of Mercury's crust formation and evolution is needed. Conversely, understanding the volatile inventory is key to determining the formation and evolution of the crust. In the following, we will summarize the current understanding of the formation of Mercury's crust; further details can be found in earlier reviews (K. E. Vander Kaaden et al. 2019; D. A. Rothery et al. 2020). The formation and evolution of Mercury are currently constrained only by the abundance of elements, as no clear mineral diagnostics have been identified. The possible identification of graphite in the upper regolith has been used to argue for graphite as the darkening agent to explain the low reflectance in the spectral observations (S. L. Murchie et al. 2015; R. L. Klima et al. 2018), with varying abundances to explain the spectral range. Observations from the GRNS are commensurate with 1–3 wt% graphite in the surface material (P. N. Peplowski et al. 2015, 2016), and measurements of optical reflectance suggest a range of 1–5 wt% (R. L. Klima et al. 2018). Based on spectral modeling, R. Xu et al. (2024) suggest that a combination of less than 1 wt% of microcrystalline graphite and similar amounts of metallic iron is adequate to explain the overall reflectances of various color units on Mercury. There are different hypotheses for the source of this graphite, from an exogenic origin from cometary impacts (M. Syal et al. 2015) to the remnants of a primordial flotation crust (K. E. Vander Kaaden & F. M. McCubbin 2015). Mercury's proximity to the Sun must result in a higher rate of comet bombardment compared to the other terrestrial planets. The higher cometary flux, coupled with a generally higher carbon content in comets, is then argued to

explain the global distribution of carbon (M. Syal et al. 2015). Alternatively, the low Fe in Mercury's mantle (mantle iron content of less than 3 wt% FeO; J. Wade et al. 2021) gave the global magma ocean too low a density to allow anorthite to float, so Mercury could not grow a lunar-like anorthosite primary crust. Thus, graphite crystals, the only phase with sufficiently low density, would have floated to the top due to their lower density compared with the silicate melt, producing a graphite flotation crust (K. E. Vander Kaaden & F. M. McCubbin 2015).

A secondary crust would have formed on top of the primary graphite crust through effusive volcanism from magma generated by subsequent partial melting events in the mantle (K. E. Vander Kaaden & F. M. McCubbin 2015). Cratering of the surface would have mixed the two crustal layers, producing the global distribution of carbon mixed within the crust. Supporting evidence for this scenario is observed as faculae in the pyroclastic deposits seen on Mercury's surface. Based on analysis of Mercury's largest pyroclastic deposit—Nathair Facula, northeast of Rachmaninoff basin—it was concluded that pyroclastic deposits are higher in reflectivity than the global surface and are depleted in carbon and sulfur (S. Z. Weider et al. 2016). A later search in the MASCS data set for pyroclastic deposits identified 68 such deposits with high reflectivity (A. Galiano et al. 2022). While the depletion in carbon and sulfur is only confirmed for Nathair Facula, and the MASCS data support the possibility of a similar depletion at other faculae, it remains uncertain if this is ubiquitous to all volcanic vent regions. The carbon and sulfur depletion would occur during their interaction with oxide silicate materials. The interaction results in explosive volcanism instigated by the exsolution of the carbon and sulfur, where the graphite layer contributes carbon to the rising magma (S. Z. Weider et al. 2016).

The pyroclastic regions are assumed to be depleted in carbon and sulfur, based on examination of the Nathair Facula region, which is the only pyroclastic deposit large enough to be examined by GRNS and XRS (S. Z. Weider et al. 2016; A. N. Deutsch et al. 2021; D. L. Pegg et al. 2021), where the depletion in S is interpreted to indicate the loss of S-bearing volatiles during the explosive volcanic event that created the deposit (S. Z. Weider et al. 2016; L. R. Nittler et al. 2018). The remainder of Mercury's surface is high in sulfur content, up to 4 wt% (L. R. Nittler et al. 2011; S. Z. Weider et al. 2015). The high sulfur content in the surface, in conjunction with the low FeO surface concentration, and the large Fe planetary core argues for a highly reducing environment during formation, assuming sulfur was dissolved in the basalts (F. M. McCubbin et al. 2012; O. Namur et al. 2016a; L. R. Nittler et al. 2018; C. Cartier et al. 2020; C. J. Renggli et al. 2022). Note that the amount of sulfur released by volcanic degassing from erupted magmas increases as the environment becomes more reducing (A. N. Deutsch et al. 2021). In a carbon–oxygen–sulfur system, the volcanic gases are expected to be dominated by such volatiles as CO, $S_2$, $CS_2$, and COS (M. Y. Zolotov 2011; M. Y. Zolotov et al. 2013; C. J. Renggli et al. 2022).

Using MDIS images and laser altimeter data, J. A. P. Rodriguez et al. (2020, 2023) provide evidence for large expanses of a volatile sublayer. Examination of the chaotic terrains antipodal to Caloris basin shows that they are too young to have formed contemporaneously with the Caloris basin formation; their development persisted until

approximately 1.8–2 Gyr after the Caloris basin formation (J. A. P. Rodriguez et al. 2020). Losses of surface elevation at multikilometer spatial scales and widespread landform retention in this chaotic region is indicative of formation by gradual collapse by the slow removal of a volatile-rich layer (J. A. P. Rodriguez et al. 2020). Instances of localized, surficial collapse within these terrains also suggest a complementary devolatilization history by solar heating (J. A. P. Rodriguez et al. 2020). Similar analyses of north polar chaotic terrains suggest a phase of volatile-enriched crustal accretion that predates the Late Heavy Bombardment, about 3.9 Ga, and is more indicative of a depositional origin for the volatile sublayer in contrast to a result from magma ocean differentiation (Rodriguez et al. 2023). In both cases, chaotic terrain formation is linked to the loss of a volatile layer within the crust, even if the source of the volatile layer is debated.

Pyroclastic volcanism provides a mechanism to remove carbon, sulfur, and related volatiles from the crust in localized areas. Chaotic terrains across Mercury's surface indicate the removal of large expanses of volatile-rich layers while hollows suggest the ongoing devolatilization of Mercury's surface. Where do these volatiles go after removal from the surface? They will become part of the exosphere, and either will be lost to space via various escape mechanisms (see the review by P. Wurz et al. 2022), be absorbed or adsorbed back on the surface, or migrate to colder locations at higher latitudes, and might even be collected within cold traps. In the following, we examine their potential retention on the surface in cold traps.

The PSRs at both poles serve as cold traps for many volatiles migrating via the exosphere (D. A. Paige et al. 2013). Measurements from ground-based radar (B. J. Butler et al. 1993; J. K. Harmon 2007; J. K. Harmon et al. 2011) and MESSENGER's GRNS (D. J. Lawrence et al. 2013) indicate the presence of water ice within the PSRs, although sulfur and certain silicates could also explain the radar observations (A. L. Sprague et al. 1995; K. Frantseva et al. 2022). The GRNS measurements are consistent with a two-layer stratigraphy in the radar-bright regions, with an upper layer 10–30 cm thick having 0%–25% water equivalent hydrogen and a lower layer with a thickness of tens of centimeters with 12%–100% water equivalent hydrogen (D. J. Lawrence et al. 2013). The total amount of water ice on the surface of Mercury is estimated to be in the mass range of $10^{14}$–$10^{15}$ kg (A. N. Deutsch et al. 2018). Examination of the PSRs by MESSENGER's Mercury Laser Altimeter (MLA) found that some of the radar-bright deposits appear bright at 1064 nm while others appear dark (G. A. Neumann et al. 2013). Thermal models predict water ice would be stable for geologic timescales at the surface in the MLA-bright regions but would need to lie about 10 cm below the surface to be stable in the MLA-dark regions (D. A. Paige et al. 2013). Radar observations of Mercury during the 2019 inferior conjunction are indicative of variations in the ice purity independent of optical brightness (E. G. Rivera-Valentin et al. 2022). There is general agreement that regions in which the water ice is exposed at the surface are optically bright, and that the optically dark surfaces are consistent with water ice overlain with an insulating layer of complex organic volatiles, tens of centimeters thick, formed as a lag deposit following the surface and near-surface sublimation of water ice (e.g., D. A. Paige et al. 2013; M. K. Barker et al. 2022). However, there has been little

discussion of the mixture of other potential volatiles within these cold traps, nor their interactions with water ice.

What are the other potential volatile species? CO, $S_2$, $CS_2$, and COS have been suggested to be associated with volcanic release. Nonrefractory sulfur compounds are suggested by the devolatilization of hollows and chaotic terrain. Both endogenic and exogenic sources for the water ice have been proposed. Endogenic sources include volcanic activity, crust and mantle outgassing, and space weathering (e.g., K. Frantseva et al. 2022), which can all also be potential sources for other volatile species. Alternatively, or in conjunction with the endogenic sources, is the exogenic delivery of water and organic material from interplanetary dust particles, asteroids, and comets. These sources could deliver sufficient water over about a 1 Gyr timescale to explain the radar and MESSENGER observations (K. Frantseva et al. 2022). It has been suggested that a single cometary impactor, like the one that formed Hokusai crater, a large young impact crater formed during the Kuiperian age, could have delivered all the ice now seen in Mercury's cold traps (C. M. Ernst et al. 2018). The potential delivery of other volatile species from these exogenic sources has not been examined in detail.

Another mechanism for volatile release is space weathering of the surface (P. Wurz et al. 2022; F. Leblanc et al. 2023). The role of solar heating has been discussed above, but solar wind irradiation and micrometeoroid bombardment also play a role in altering the surface chemistry. Solar wind irradiation contributes to the formation of the exosphere by releasing various volatile species, such as sodium and potassium as well as refractory species. Solar wind irradiation and micrometeoroid impact vaporization are the only processes capable of releasing refractory species, such as calcium and magnesium, from the surface to the exosphere (P. Wurz et al. 2022). In addition to kinetic sputtering by solar wind ions, potential sputtering by $He^{++}$ ions of the solar wind results in the selective removal of O atoms from the mineral surface (P. S. Szabo et al. 2020a). Another result of solar wind irradiation is that solar wind ions and electrons are implanted into the surface, forming short-lived volatiles, glasses (especially glassy or amorphous rims), and nanophase materials (C. M. Pieters & S. K. Noble 2016). On the lunar surface, these nanoscale materials are iron; on asteroids, they are iron or iron sulfides. However, the observed low iron content of Mercury's surface with 1–2 wt% FeO derived from the XRS measurements (e.g., L. R. Nittler et al. 2018), which agrees with pre-MESSENGER estimates (P. Wurz et al. 2010), appears to conflict with iron as the dominant nanoscale material. This might be resolved by the information depth of XRS of tens of micrometers compared to the tens of nanometers for the depth range of nanophase iron (see the discussion above). Recent laboratory experiments on Mercury analog material showed that the combination of high surface temperatures and ion irradiation leads to the formation of nanophase iron and, with time, even submicron iron (R. Pang et al. 2024). More experiments are needed to examine the production of nanoscale carbon, sulfur, or sulfides as potential space-weathering products.

While altering the surface chemistry through different mechanisms, micrometeoroid bombardment also produces many of the same products as solar wind irradiation. These include amorphous rims and nanoscale materials. In addition, micrometeoroid bombardment also produces glass components in the regolith via impact melt. These components include agglutinates, which are glass-welded regolith grains. M. J. Cintala (1992)

estimated about 14 times more impact melt would be produced on Mercury's surface compared to the lunar surface, suggesting that there would be little crystalline material within the Hermean regolith. Early estimates based on Mariner 10 observations yield a fraction of glassy regolith particles of 70% (Y. Langevin 1997). Based on spectral modeling, J. Warell et al. (2010) estimated 20%–45% glass content for Mercury's surface, which exceeds the 7%–29% glass found in Apollo and Luna regolith samples (Table 5.1 in G. H. Heiken et al. 1991), but not to a degree that is suggested by the estimated increase by M. J. Cintala (1992) in impact melt production. The typical grain size of the regolith particles on Mercury is estimated to be 30 $\mu$m (J. Warell & D. T. Blewett 2004).

MESSENGER observations suggest a magma ocean formed on proto-Mercury. The cooling rate, and hence the lifetime of surficial melt, was determined from a coupled interior–atmosphere model (N. Jäggi et al. 2021a). Combining the melt lifetime and atmospheric escape flux (by considering plasma heating, photoevaporation, Jeans escape, and photoionization) provides estimates for the total mass loss from early Mercury. The timescale for efficient interior–atmosphere chemical exchange is less than 10,000 yr. Therefore, escape processes only account for an equivalent loss of less than 2.3 km of crust (0.3% of Mercury's mass). According to this model, $\leqslant 0.02$% of the total mass of $H_2O$ and Na is lost. Therefore, cumulative loss cannot significantly modify Mercury's bulk mantle composition during the magma ocean stage. Mercury's large metal core, its silicate mantle, and its volatile-rich surface may instead reflect chemical variations in its building blocks resulting from its solar-proximal accretion environment.

### 2.1. Review of the Global Elemental Composition of Mercury's Surface

Measurements of the elemental composition of Mercury's surface were conducted by the MESSENGER spacecraft, whose payload consisted of three instruments for examining the surface elemental composition: the XRS, GRS, and NS. Elements detected and mapped by the XRS include Mg, Al, Si, S, Ca, and Fe (e.g., L. R. Nittler et al. 2018; L. R. Nittler & S. Z. Weider 2019), whereas those detected and mapped by the GRNS include H, C, O, Na, Al, Si, S, Cl, K, Ca, Fe, Th, and U (e.g., L. R. Nittler et al. 2018; L. R. Nittler & S. Z. Weider 2019). While the XRS and GRNS probe to different depths within the regolith (tens of micrometers and tens of centimeters, respectively; see Figure 1), the detected element abundances, mostly given relative to silicon, are summarized in Table 1 (updated from L. R. Nittler et al. 2018). The results from both instruments for the elements measured in common (Al, Si, S, Ca, and Fe) are generally consistent (e.g., L. R. Nittler et al. 2018; L. R. Nittler & S. Z. Weider 2019), but are somewhat lower for the XRS measurements, suggesting that the overall XRS ratios are underestimated (or the Si abundance is overestimated), or this reflects the difference in global ratios (XRS) compared with northern hemisphere values (GRS). Because of the lower count rates in the GRS instrument, measurements could only be performed near the pericenter of the MESSENGER orbit, which favored the northern hemisphere.

MESSENGER XRS measurements of element ratios are shown in Figure 2 for the entire surface in cylindrical projection maps (L. R. Nittler et al. 2020). Some of the major surface features indicated in Figure 2 are the Caloris basin (CB), the high-Mg region (HMR), the northern smooth plains

**Table 1**
Mercury's Surface Element Composition Ratios by Mass with Respect to Si, or Abundance

| Element (Ratio) [a] | XRS | GRS[b] | NS[b] |
|---|---|---|---|
| K/Th | | 8000 ± 3200 | |
| Mg/Si | 0.436 (0.106) | | |
| Al/Si | 0.268 (0.048) | 0.29 (+0.05–0.13) | |
| S/Si | 0.076 (0.019) | 0.092 ± 0.015 | |
| Ca/Si | 0.165 (0.030) | 0.24 ± 0.05 | |
| Ti/Si | 0.0083 ± 0.0040 | | |
| Cr/Si | 0.00608 ± 0.0001 | | |
| Mn/Si | 0.004 ± 0.001 | | |
| Fe/Si | 0.053 (0.013) | 0.077 ± 0.013 | |
| Na/Si (average) | | 0.12 ± 0.01 | |
| Na/Si (0–60°N) | | 0.107 ± 0.008 | |
| Na/Si (80–90°N) | | 0.198 ± 0.030 | |
| Cl/Si (average) | | 0.0057 ± 0.0010 | |
| Cl/Si (0–60°N) | | 0.0049 ± 0.001 | |
| Cl/Si (80–90°N) | | 0.014 ± 0.005 | |
| O/Si | | 1.2 ± 0.1 | |
| C (wt%) | | 1.4 ± 0.9 | ~1–4 |
| K (ppm, average) | | 1288 ± 234 | |
| K (ppm, range) | | 240–2500 | |
| Th (ppm) | | 0.155 ± 0.054 | |
| U (ppb) | | 90 ± 20 | |

**Notes.** Updated from the Review by L. R. Nittler et al. (2018) L. R. Nittler et al. (2011, 2016), P. N. Peplowski et al. (2011, 2012b, 2014, 2015, 2016), L. G. Evans et al. (2012, 2015), S. Z. Weider et al. (2014, 2015), E. A. Frank et al. (2015), F. M. McCubbin et al. (2017), and L. R. Nittler et al. (2019, 2023)
[a] Ratios are by mass. Numbers in parentheses indicate the standard deviation (σ) of the XRS measurements, reflecting surface variability; the ± symbol denotes the 1σ statistical uncertainty.
[b] GRS and NS data are from the northern hemisphere.

(NSP), now called the Borealis Planitia, and the Rachmaninoff basin (R). The location of the large pyroclastic deposit (Nathair Facula) northeast of the Rachmaninoff basin has an unusually high Ca/S ratio, as indicated in panel (f), interpreted as a low S abundance rather than a high Ca abundance (see Figure 2). The most striking feature of the S/Si and Ca/Si maps is the obvious enhancement of both S and Ca in the HMR. Since the first MESSENGER orbital data were available (e.g., L. R. Nittler et al. 2011), it has been recognized that S and Ca are strongly correlated on Mercury's surface, with the exception at Nathair Facula, suggestive of the possible presence of oldhamite (CaS), which was previously inferred based on modeling and spectroscopic observations of the exosphere (P. Wurz et al. 2010). Based on petrologic modeling, it is more likely a mixture of Ca, Mg, and S, where the Mg:Ca ratio in the laboratory sulfides is about 75:25 under Mercury conditions (K. R. Stockstill-Cahill et al. 2012).

The element composition experiments onboard MESSENGER (GRNS and XRS) revealed a surface high in magnesium, low in iron and titanium, and elevated in volatile elements such as sulfur, carbon, chlorine, potassium, and sodium compared to other terrestrial planets, in addition to variations in aluminum and calcium across the surface (L. R. Nittler et al. 2011; P. N. Peplowski et al. 2011; L. G. Evans et al. 2012; K. R. Stockstill-Cahill et al. 2012; L. R. Nittler & S. Z. Weider 2019). Global element ratios with respect to Si are shown in Table 1, and element abundances detailed for major geochemical terranes on Mercury are given in Table 2. The definition of

the geochemical terranes is given below in Section 2.1.3 and Figure 6 below.

Significant amounts of C, S, Cl, Na, and K have been observed on the surface. Na and K have also been observed in the exosphere, indicating that active processes replenish the volatile species on the surface by providing a superficial surface coating (A. Mura et al. 2009; L. R. Nittler et al. 2011; L. G. Evans et al. 2012, 2015; P. N. Peplowski et al. 2012a, 2015; D. Gamborino et al. 2019).

*2.1.1. Volatile Elements*

The volatile elements found on Mercury's surface can be grouped into highly volatile and moderately volatile species. The highly volatile species, such as H and organics, are found localized to the PSRs in polar impact craters (e.g., N. L. Chabot et al. 2018b; L. R. Nittler et al. 2018). The moderately volatile species, namely Na, S, Cl, and K, are found globally at higher-than-expected abundances (L. R. Nittler et al. 2011; P. N. Peplowski et al. 2011, 2012a, 2014; S. Z. Weider et al. 2012, 2015; J. G. Evans et al. 2015). The abundances of these elements are similar to those derived for Mars (L. R. Nittler et al. 2018). For example, the K/Th and Cl/K ratios presented in Figure 3 show that Mercury's inventory of these volatiles is higher than terrestrial values and more similar to Mars, the most volatile rich of the terrestrial planets (e.g., L. R. Nittler & S. Z. Weider 2019). Sulfur is another moderately volatile element that was also detected at about 2 wt% abundance on average across the surface (see Table 2 and Figure 2), which is about 2 orders of magnitude higher in abundance than the terrestrial crust values of a few 100 s ppm (e.g., L. R. Nittler et al. 2018). This large abundance of S, and low abundance of Fe, has important implications for Mercury's redox conditions (e.g., T. J. McCoy et al. 2018; L. R. Nittler et al. 2018; L. R. Nittler & S. Z. Weider 2019).

The abundances of many of these volatile species are heterogeneous across the surface (see Figure 2 and Table 2). The Na abundance ranges from 2.6 wt% at the equator and at lower latitudes to about 5 wt% at northern latitudes above 75° (P. N. Peplowski et al. 2014), whereas the abundance of Cl varies between 0.14 and 0.35 wt% at the equator and the high northern latitudes, respectively (L. G. Evans et al. 2015). Heterogeneities in K abundance are also noted with enhancements at northern latitudes, and in particular at the warm longitudes rather than the hot ones (see Figure 2 and P. N. Peplowski et al. 2012a; L. R. Nittler & S. Z. Weider 2019), which reflects the temperature evolution of the surface during the highly elliptic orbit of Mercury. The 3:2 spin–orbit coupling of Mercury causes subsequent perihelia occurring at alternating longitudes offset by 180°, the two hot poles at longitudes of 0° and 180°, and similarly the subsequent aphelia occurring at longitudes offset by 180° and the two warm poles at longitudes of 90° and 270°. Also, an increased detection of H by NS associated with the PSRs near the poles is observed (e.g., D. J. Lawrence et al. 2013; L. R. Nittler & S. Z. Weider 2019). Since Na, K, and Cl are volatile at the temperatures of Mercury's surface, they will be redistributed thermally via exospheric transport and migrate to colder locations once they are freed from their mineral host via space weathering, which affects the top meter of the surface (limited by the penetration depth of galactic cosmic rays). Mg is less abundant at the northern latitudes, and Mg is not volatile. The thermal migration is assisted by sputtering, with Mercury-wide transport via the
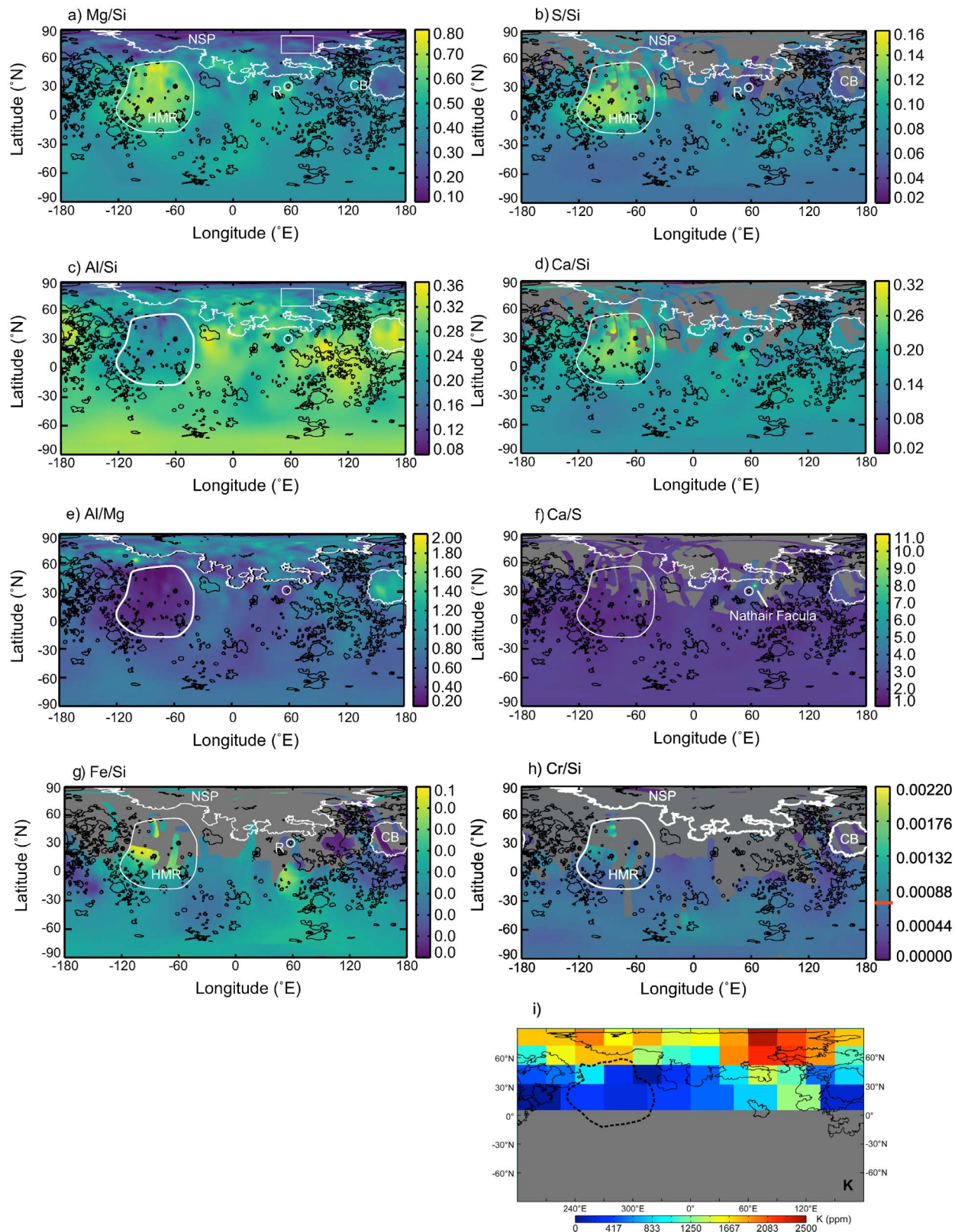
**Figure 2.** Smoothed maps in cylindrical projection of (a) Mg/Si, (b) S/Si, (c) Al/Si, (d) Ca/Si, (e) Al/Mg, (f) Ca/S, (g) Fe/Si, and (h) Cr/Si from MESSENGER XRS data, and (i) K abundance derived from MESSENGER GRS data. Figure adapted from L. R. Nittler et al. (2020, 2023) and P. N. Peplowski et al. (2012a), with permission. Uncertainty maps for these element ratios by mass are given in the original publication (L. R. Nittler et al. 2020). Some major features are indicated by white outlines: CB—Caloris basin; NSP—northern smooth plains (J. W. Head et al. 2011); HMR—high-Mg region (S. Z. Weider et al. 2015); R—Rachmaninoff basin. Smooth plains deposits (B. W. Denevi et al. 2013) are outlined with white or black lines. The white rectangles in panels (a) and (c) indicate the location of the impact craters in the NSP. Gray areas are unmapped for these elements. The location of the large pyroclastic deposit (Nathair Facula) northeast of the Rachmaninoff basin has an unusually high Ca/S ratio, as indicated in panel (f).
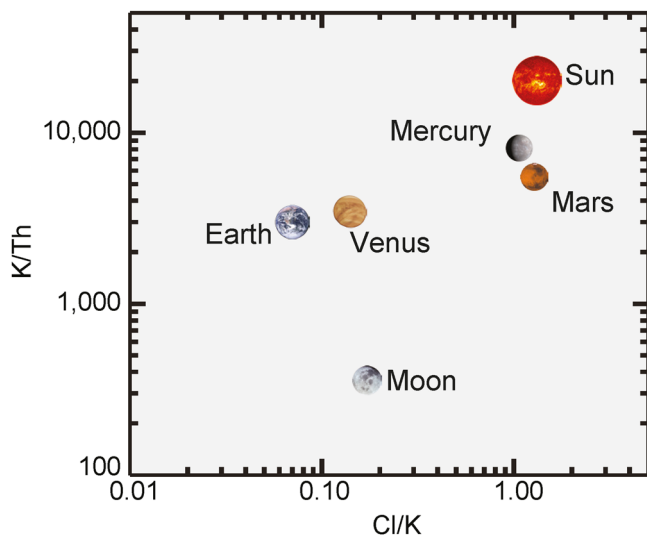
**Figure 3.** The K/Th as a function of Cl/K weight ratios of Mercury's surface as determined from GRNS (P. N. Peplowski et al. 2012a; Evans et al. 2015; L. R. Nittler & S. Z. Weider 2019) compared to values for the other terrestrial planets, the Moon, and the Sun. Figure from L. R. Nittler & S. Z. Weider (2019), with permission.
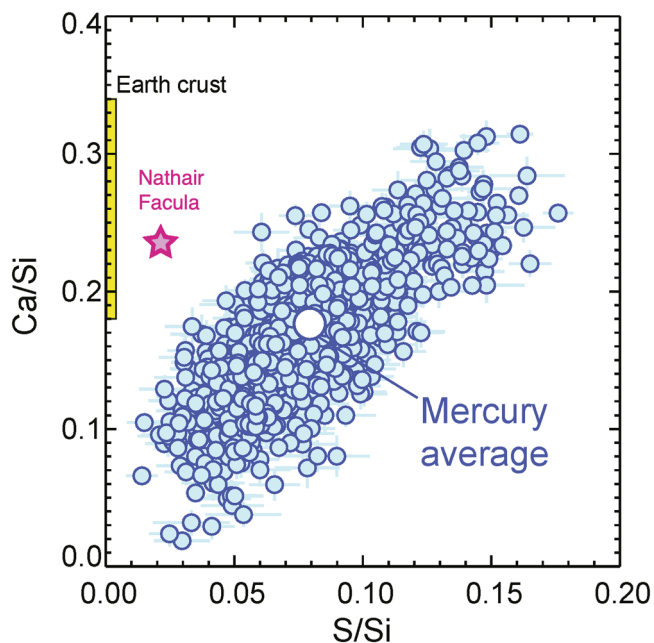


**Figure 4.** Comparison of Ca/Si as a function of S/Si element abundance ratios of Mercury's surface as measured by the XRS (blue circles). The range of these element ratios for Earth's crust are shown by the yellow box. Nathair Facula, a probable pyroclastic deposit northeast of the Rachmaninoff impact basin, is shown by the red star. Figure adapted from L. R. Nittler & S. Z. Weider (2019), with permission.

**Table 2**
Chemical Composition (in wt%) for Geochemical Terranes on Mercury from T. J. McCoy et al. (2018) and for Cr from L. R. Nittler et al. (2023)

| Element | Southern Hemisphere | Northern Latitudes | Low Fast | High Magnesium | Caloris Interior Plains |
|---|---|---|---|---|---|
| O | 39.65 | 42.27 | 41.13 | 37.21 | 41.31 |
| Na | 2.83 | 5.74 | 2.94 | 2.66 | 2.95 |
| Mg | 12.44 | 7.55 | 12.34 | 16.48 | 9.15 |
| Al | 7.79 | 6.04 | 7.05 | 5.32 | 9.44 |
| Si | 28.32 | 30.19 | 29.38 | 26.58 | 29.51 |
| S | 2.07 | 2.11 | 1.76 | 2.92 | 1.77 |
| Cl | 0.14 | 0.45 | 0.24 | 0.13 | 0.15 |
| K | 0.13 | 0.20 | 0.15 | 0.10 | 0.08 |
| Ca | 4.55 | 4.23 | 3.82 | 5.58 | 4.43 |
| Ti | 0.34 | 0.36 | 0.35 | 0.32 | 0.35 |
| Cr | 200 ppm | … | … | 300 ppm | 90 ppm |
| Mn | 0.11 | 0.12 | 0.12 | 0.11 | 0.12 |
| Fe | 1.48 | 0.60 | 0.59 | 2.44 | 0.59 |
| Total | 99.85 | 99.86 | 99.87 | 99.85 | 99.85 |

**Note.** The definition of the geochemical terranes is given in Section 2.1.3 and Figure 6 below.

### 2.1.2. Nonvolatile Elements

The measured Mg, Al, Ca, and Fe abundances are reported relative to Si (see Table 1). On average, Mercury's surface is found to have a higher Mg/Si ratio but lower Al/Si, Ca/Si, and Fe/Si ratios than typical terrestrial and lunar crustal materials (e.g., L. R. Nittler et al. 2018; L. R. Nittler & S. Z. Weider 2019). The Ca/Si ratio is highly correlated with the S/Si ratio (Figure 4), which suggests that the Ca/S ratio is constant globally, which is indeed observed, as can be seen in Figure 2.

The low Fe surface content (in the range of 1–2 wt%) and high S content (up to 4 wt%) are strong evidence that Mercury's interior formed under highly chemically reducing conditions (e.g., L. R. Nittler et al. 2018), as decreasing incorporation of Fe and increasing incorporation of S into silicate melts occurs as the availability of O decreases (D. R. Haughton et al. 1974; T. J. McCoy et al. 1999; S. Berthet et al. 2009; O. Namur et al. 2016b; L. R. Nittler et al. 2018). The major elemental surface composition suggests that the surface is similar to, but not necessarily identical to, a partial melt extracted from highly reduced enstatite chondrite meteorites (T. J. McCoy et al. 1999; T. H. Burbine et al. 2002; L. R. Nittler et al. 2011, 2018). The high Mg content initially suggested that the surface composition was similar to terrestrial komatiites (L. R. Nittler et al. 2011, 2018), but petrologic modeling and experiments based on a more complete suite of measured elements indicate the surface is more similar to norites in terms of mineralogy (K. R. Stockstill-Cahill et al. 2012) and boninites, a primitive andesite characterized by high MgO (>8 wt%) and low TiO$_2$ (<0.5 wt%), in terms of chemistry

Another element present, at unexpectedly high abundances, is carbon. The abundance of carbon in the terrestrial crust is <0.2 wt%, but for Mercury's surface, GRNS gives an average upper limit of <4.1 wt% C (e.g., P. N. Peplowski et al. 2015; L. R. Nittler et al. 2018; L. R. Nittler & S. Z. Weider 2019). This correlates well with reflectance observations in the visible and near-infrared range. Mercury's surface is, on average, darker than the lunar surface (M. S. Robinson et al. 2008). On the Moon, the darkening agent is largely due to Fe- and Ti-bearing minerals, such as ilmenite. The low Fe abundance on
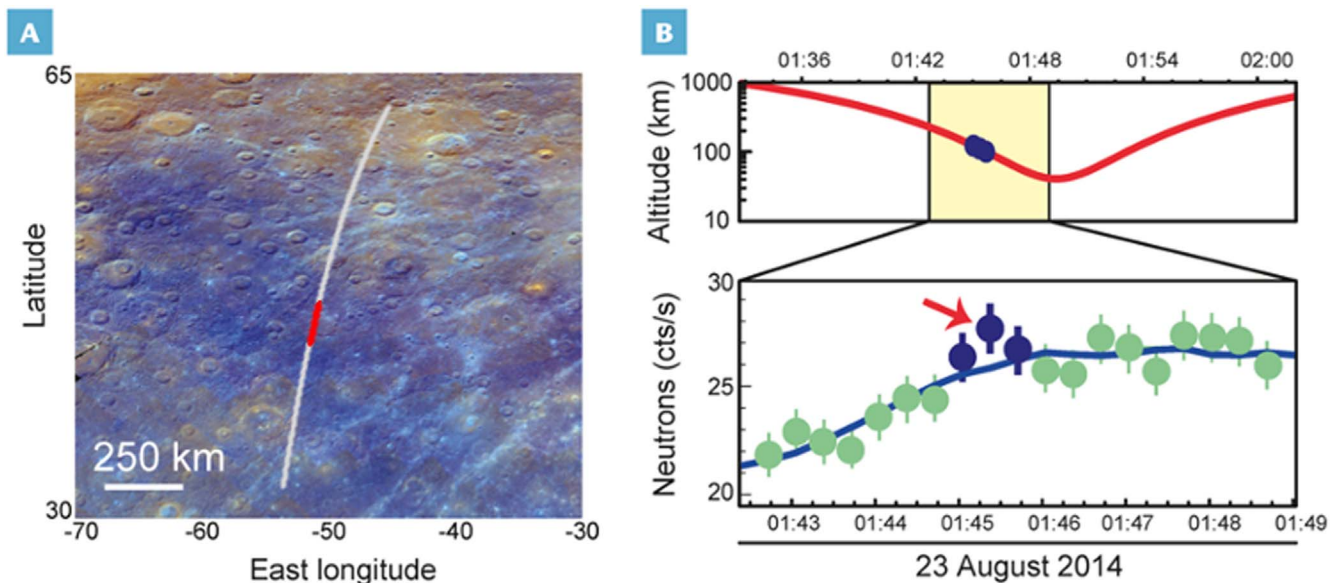
exosphere (A. Mura et al. 2009). An anticorrelation between the K and the Mg abundance over the northern hemisphere was found in the composition data (S. Z. Weider et al. 2015), which has been used to argue against the thermal redistribution of volatiles and in favor of a different composition of the northern terranes (e.g., S. Z. Weider et al. 2015; L. R. Nittler & S. Z. Weider 2019). Of course, a different mineralogy in the northern terranes is very likely (e.g., T. J. McCoy et al. 2018; P. N. Peplowski & K. Stockstill-Cahill 2019), but thermal redistribution of volatiles will also occur.

**Figure 5.** (A) A region of Mercury enriched in LRM (dark blue in this enhanced-color representation, which is based on a mathematical treatment of MESSENGER color imagery). The gray line corresponds to the orbit path shown in panel (B), with the red line corresponding to the blue data points displaying higher count ranges. (B) Spacecraft altitude and low-energy neutron count rate as a function of time (hours, UTC) for a portion of a MESSENGER orbit on 2014 August 23. The blue symbols indicate when the spacecraft was above the LRM area shown in panel (A). The thermal neutron counts (in counts per second) are higher for the LRM than expected from the average trend (blue curve) of values measured outside the LRM (green symbols) for the orbit. This indicates an enhanced abundance of carbon. Figures are from L. R. Nittler & S. Z. Weider (2019), with permission.

Mercury precludes a similar darkening agent. S. L. Murchie et al. (2015) demonstrated that fine-grained graphite would produce the observed low albedo, if it is present at ∼1 wt% globally and at ∼5 wt% within the LRM. As can be seen in Figure 5, NS observations during a low-altitude flyby show an increased count rate of thermal neutrons over the area of low albedo, supporting the inferred enhanced C abundance in LRM (P. N. Peplowski et al. 2016; L. R. Nittler et al. 2018; L. R. Nittler & S. Z. Weider 2019).

### 2.1.3. Heterogenous Distribution—Geochemical Terranes

GRS measurements indicate that the Si and O gamma-ray count rates do not show statistically significant variations in longitude and latitude over Mercury's surface at the two-standard-deviation level (P. N. Peplowski et al. 2012a). However, many elements detected across Mercury's surface do have a heterogenous spatial distribution (Figure 2) and show evidence for distinct geochemical terranes (Figure 6). T. J. McCoy et al. (2018) defined four such geochemical terranes based on three criteria: spatial continuity, spatial extent (>1000 km in the shortest horizontal dimension), and chemical distinction from the average composition (Figure 6). The element chemistry data used by T. J. McCoy et al. (2018) to distinguish the geochemical terranes were the average O/Si ratio from GRS measurements (L. G. Evans et al. 2012), latitude-dependent Na, Cl, and K abundances from the GRS observations (P. N. Peplowski et al. 2012a, 2014; L. G. Evans et al. 2015), the Mg, Al, S, Ca, and Fe abundances from the XRS observations (S. Z. Weider et al. 2015; L. R. Nittler et al. 2020), the total macroscopic neutron absorption cross section (P. N. Peplowski et al. 2015), and average atomic mass (D. J. Lawrence et al. 2017) from the NS measurements. Mineralogies were derived from the elemental abundances based on Cross, Iddings, Pirsson, and Washington (CIPW) normative calculations (W. Cross et al. 1902). In terms of

mineralogy, the rocks are described as gabbros, anorthosites, and norites based on the modeled abundance of plagioclase $((Na,Ca)(Si,Al)_4O_8)$ and the mafic minerals clinopyroxene $((Ca,Mg,Fe)_2Si_2O_6)$ and orthopyroxene $((Mg,Fe,Ca)(Mg,Fe,Al)(Si,Al)_2O_6)$. This nomenclature is commonly applied only to plutonic rocks, as these are fully crystallized. In T. J. McCoy et al. (2018), the nomenclature and its corresponding ternary diagrams are used purely for visualization purposes, given the chemistry of the geochemical terranes (Figure 6 and T. J. McCoy et al. 2018). However, it should be noted that the modeled abundances of these minerals from petrologic calculations includes some broad assumptions, including crystallization under equilibrium conditions, no space-weathering modification of the element abundances, abundant oxygen, and that the measurements represent homogeneous igneous rock. Considering there has been mixing within the regolith and space weathering of the surface, some of these assumptions can be challenged, though they represent a solid, first-order reference for the surface minerology.

T. J. McCoy et al. (2018) used as the average composition of Mercury's surface the composition of the southern hemisphere (Table 2) because the poor spatial resolution of the measurements of element abundances in the southern hemisphere provide a generalized measure of broad swaths of the surface. The southern hemisphere is characterized by high Mg/Si, S/Si, and Na/Si ratios (the last of which is only inferred) and low Al/Si and Ca/Si ratios compared with terrestrial oceanic basalts (L. R. Nittler et al. 2011; P. N. Peplowski et al. 2011; T. J. McCoy et al. 2018). The normative mineralogy of the southern hemisphere is best described as an olivine norite, with norite composed of calcium-rich plagioclase, orthopyroxene, and olivine. Its total alkalis versus silica composition (TAS; see Figure 7) indicates that it lies between a basaltic andesite and andesite.

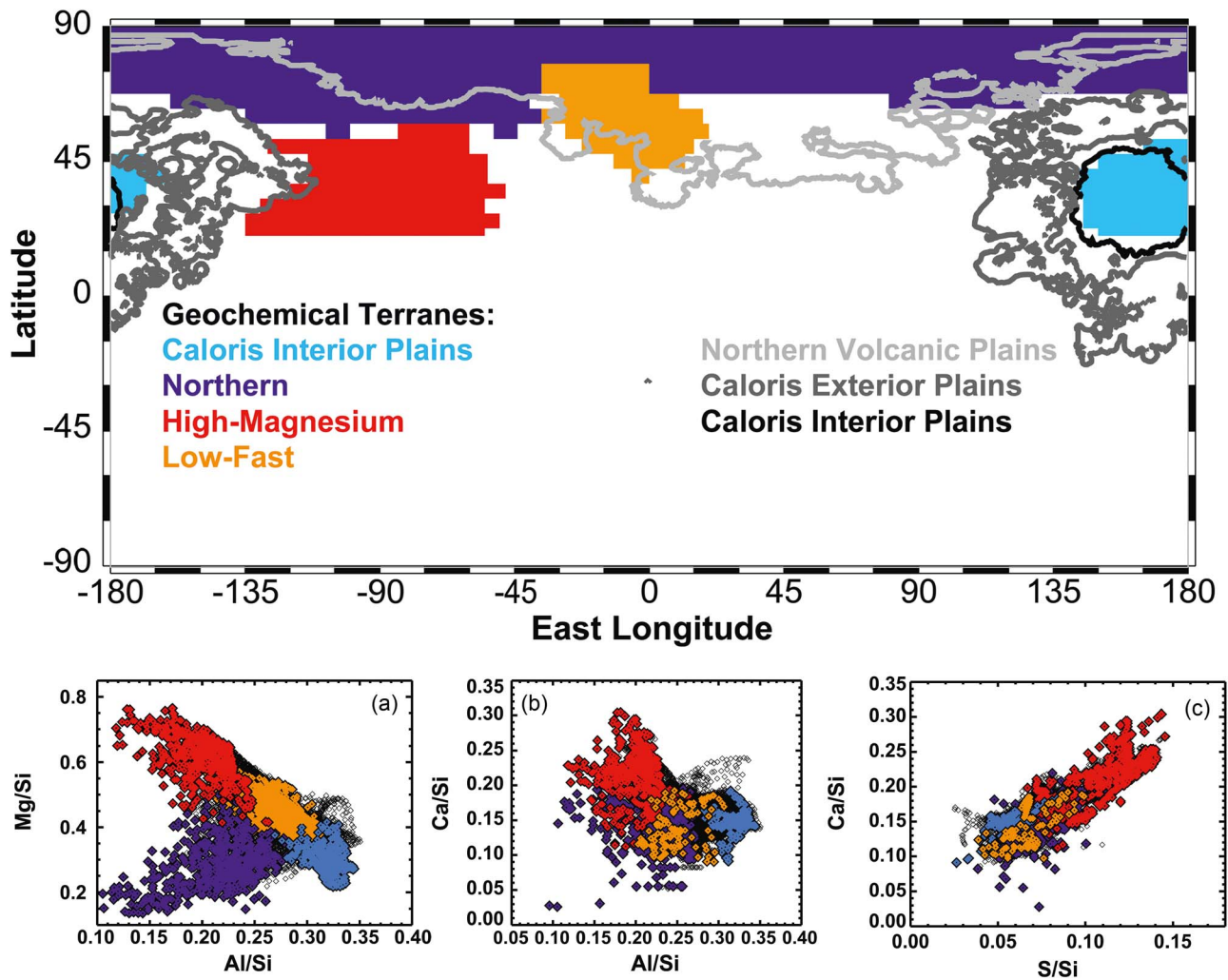The resulting four geochemical terranes are the northern terrane (NT), the Caloris interior plains terrane (CB), the

10

**Figure 6.** Top: map of the locations of the geochemical terranes identified by T. J. McCoy et al. (2018). The boundaries of the geomorphologic plains units from B. W. Denevi et al. (2013) are also shown. Bottom panels: the Mg/Si, Ca/Si, Al/Si, and S/Si element abundance ratios for the different geochemical terranes. In all maps and graphs, red–high-magnesium terrane; purple–northern terrane; blue–Caloris interior plains terrane; yellow–low-fast terrane. Figure adapted from T. J. McCoy et al. (2018), with permission.

high-magnesium terrane (HMR), and the low-fast terrane (LFT). There are indications of other, smaller locations of distinct chemical composition, such as pyroclastic deposits (e.g., Nathair Facula, northeast of Rachmaninoff basin) and LRM, but these are not classified as terranes because of their limited spatial extent (T. J. McCoy et al. 2018). In their analysis, T. J. McCoy et al. (2018) assumed that, in all geochemical terranes, there is enough S available (see Table 2) for the transition metals to form sulfides, so they do not occur as oxides. In that case, the Mg-rich nature of Mercury makes any effusive rock that exceeds 52 wt% $SiO_2$ a boninite.

The NT (Figure 6), which overlaps in part with the NSP (Borealis Planitia), displays a relatively low Mg/Si ratio compared to the other terranes, moderate to low Al/Si, Ca/Si, and S/Si ratios, and substantial enrichment in Na, K, and Cl (see Figure 3 and, e.g., T. J. McCoy et al. 2018; P. N. Peplowski & K. Stockstill-Cahill 2019). Thermal redistribution of these volatiles has been suggested, due to the inverse correlation between high surface temperatures and the K abundance (P. N. Peplowski et al. 2012a) and the similar latitude profiles of Na and K (P. N. Peplowski et al. 2014). As discussed above, part of this increased abundance of volatiles

can be attributed to thermal migration to colder locations, whereas part could reflect different composition of this geochemical terrane; for example, Mg is significantly lower and Al is somewhat lower than in most other geochemical terranes on Mercury. As Figure 7 shows, the element composition of the NT is commensurate with trachytes ($SiO_2$-rich, alkali feldspar-dominated rock with low mafic content, though the formation mechanism is not the same as for terrestrial trachytes), and it also could be classified as a boninite (e.g., T. J. McCoy et al. 2018). This terrane's mineralogy is best described as an olivine-bearing anorthositic gabbro (T. J. McCoy et al. 2018).

The Caloris interior plains terrain displays lower Mg/Si and higher Al/Si ratios (S. Z. Weider et al. 2012), lower K content (P. N. Peplowski et al. 2012a), and a low neutron absorption cross section (P. N. Peplowski et al. 2015; S. Z. Weider et al. 2015; T. J. McCoy et al. 2018). In the low-Mg TAS diagram of volcanic rocks (Figure 7), the composition falls within the andesite field but can also be classified as a boninite (e.g., T. J. McCoy et al. 2018). This terrain is best described as a rock intermediate between anorthosite and norite in composition (T. J. McCoy et al. 2018).
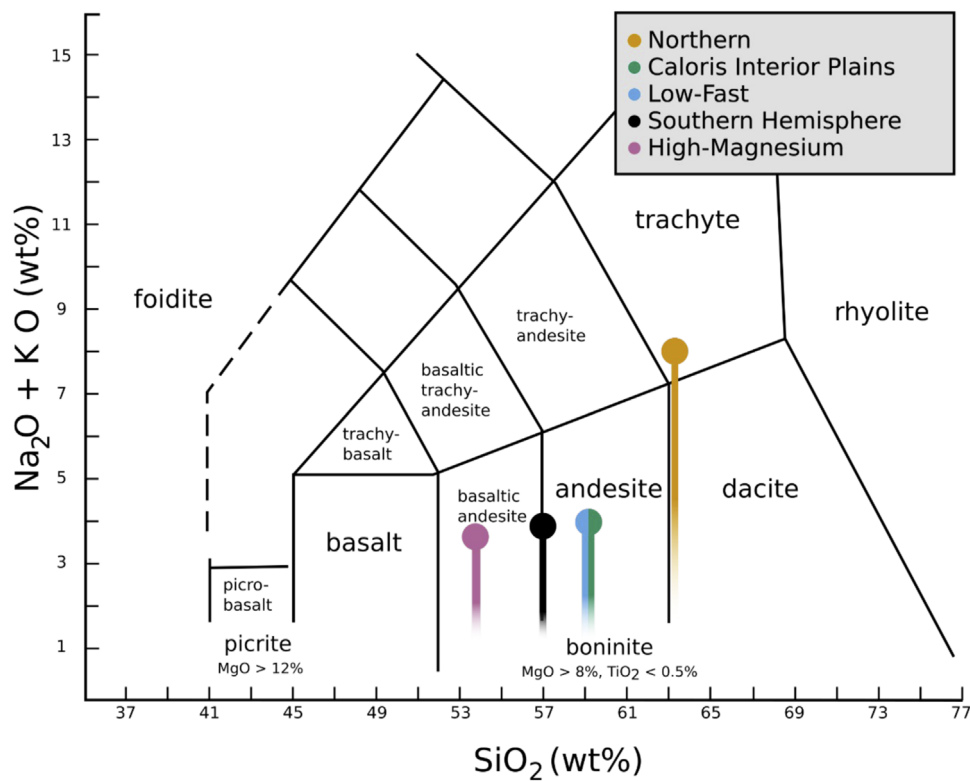
**Figure 7.** Simplified TAS diagram of volcanic rocks with the compositions (dots) of the geochemical terranes after T. J. McCoy et al. (2018). The uncertainties (lines) are based on the possibility that Na and K within Mercury's regolith are not bound within grains and do not represent the rock chemistry. Boninites describes any rock that has $SiO_2 > 52$ wt%, MgO > 8 wt%, and $TiO_2 < 0.5$ wt%.

The HMR displays the highest Mg/Si, Ca/Si, and S/Si ratios and the lowest Al/Si ratio of the investigated terrains (see Figure 2 and, e.g., T. J. McCoy et al. 2018; P. N. Peplowski & K. Stockstill-Cahill 2019) and corresponds to an area of high neutron absorption (P. N. Peplowski et al. 2015; T. J. McCoy et al. 2018). The Si and more so the Al abundances are actually lower in the HMR than elsewhere on Mercury's surface (see Table 2). In the TAS diagram, this terrain falls within the basaltic andesite field and is also classified as a boninite (T. J. McCoy et al. 2018). This terrain's mineralogy is best described as an intermediate between anorthosite and norite (T. J. McCoy et al. 2018).

The LFT is a region that displays low count rates for fast neutrons contained largely within, but not corresponding precisely with, the lower latitudes of the NSP (the Borealis Planitia) (D. J. Lawrence et al. 2017) and generally has low Mg, S, and Ca abundances (e.g., T. J. McCoy et al. 2018). It lies adjacent to the NT (Figure 6) and displays lower Na/Si and Ca/Si and higher Mg/Si ratios than the NT (T. J. McCoy et al. 2018). Chemically, it is very similar to the southern hemisphere and distinguishes itself from the average surface with higher Cl and Ca abundances (T. J. McCoy et al. 2018). In the TAS diagram, it correlates to the low-Mg andesite field, but is also classified as a boninite (T. J. McCoy et al. 2018). This terrain's mineralogy is best described as a norite (T. J. McCoy et al. 2018).

By locating the observations of element abundances (e.g., Figure 2), and from the inferred mineralogy in the TAS diagram shown in Figure 7, one has to consider the possibility that the observed Na is only partially associated with an actual mineral, and partially with the freed Na that is thermally redistributed to colder regions and absorbed in the topmost

10 cm of the regolith as atomic Na (see the discussion in Section 4.1 below). The high Na abundance observed in the northern latitudes above 80°N of 5.74 wt% might be interpreted as a combination of redistributed atomic Na and Na bound in minerals; the latter is about 2.9 wt% elsewhere on Mercury's surface (Table 2 and P. N. Peplowski et al. 2014). If the Na that can be associated with mineralogy is thus lower than the observed element abundance, the NT would instead by classified as a less alkali-rich dacite, which would be more in line with the remainder of the geochemical terranes and the southern hemisphere. This would also solve the problem that the high Na concentration of 5.75 wt% in the northern latitudes presents for the CIPW normative calculation (Cross et al. 1903). Actually, Na thermal redistribution was mentioned as a way to resolve the CIPW problem (T. J. McCoy et al. 2018).

A similar discussion can be done for S, assuming sulfides are the volatile compounds in the hollows formation (see Section 2.2.4). Hollows are found all over Mercury's surface (R. J. Thomas et al. 2014). It has been postulated that, during their formation, substantial amounts of S are released from the hollows into the exosphere and distributed globally via exospheric transport (J. Helbert et al. 2013, R. J. Thomas et al. 2014; C. J. Bennet et al. 2016; D. T. Blewett et al. 2018; O. Barraud et al. 2023). Since most of the S in the exosphere falls back onto the surface, this would result in a global S coverage, which is indeed observed (Figure 2). Additionally, some of the observed S might not be present in the form of minerals (e.g., sulfides) but might be physisorbed sulfur (held by van der Waals forces) in the topmost regolith layer. Since S is much less volatile than Na, having a sublimation temperature of 490 K, it migrates much more slowly to colder areas on Mercury's surface.

## 2.2. Review of Global Surface Mineralogy

### 2.2.1. Understanding of the Global Surface Mineralogy After Mariner 10

With the Mariner 10 mission (F. Vilas et al. 1989), which only imaged about half of the surface, and with ground-based observations of Mercury's surface, which covered the remaining part of the surface, Mercury was found to be heavily cratered and covered with highly space-weathered silicate material (A. Sprague et al. 2007, 2009; B. W. Denevi & M. S. Robinson 2008). The regolith is composed of impact-fragmented planetary crust mixed with subsequent arrivals of material from comets, meteorites, and particles from the Sun. Ground-based observations in the visible and near-infrared range indicate a heterogeneous surface composition with $SiO_2$ abundance ranging from 39 to 57 wt% (F. Vilas 1985; D. T. Blewett et al. 1997, 2002; T. H. Burbine et al. 2002; A. Sprague et al. 2007, 2009). Visible and near-infrared spectra, multispectral imaging, and modeling indicate expanses of a feldspathic, well-comminuted surface with some smooth regions that are likely to be magmatic in origin, with many widely distributed crystalline impact ejecta rays and blocky deposits (D. T. Blewett et al. 2002; A. L. Sprague et al. 2002). Pyroxene spectral signatures have been recorded at four locations. Although Mercury's surface is highly space weathered, there was little evidence for the conversion of FeO to nanophase metallic iron particles as at the Moon (F. Vilas 1985; M. S. Robinson & G. J. Taylor 2001; D. T. Blewett et al. 2002). Near- and mid-infrared spectroscopy indicate clinopyroxene and orthopyroxene are present at different locations. There is some evidence for no- or low-iron alkali basalts and feldspathoids. All evidence available at the time, including microwave studies, point to a surface that is low in iron and low in titanium (A. Sprague et al. 2007). The expected link in composition between the surface and the exosphere was used to infer the possible composition of the surface of Mercury (P. Wurz et al. 2010).

### 2.2.2. Understanding of the Global Surface Mineralogy After MESSENGER

Even though the MESSENGER spacecraft flew both a color camera, MDIS, and an ultraviolet to near-infrared spectrometer, MASCS, no definitive mineralogic absorption features were identified within the wavelength range of the VIRS of MASCS (visible: 300–1050 nm, and near-infrared: 850–1450 nm). Therefore, the mineralogy of Mercury's surface had to be inferred by using the element abundance maps derived from the XRS and GRS measurements, as was discussed above in Section 2.1.3, as a basis for normative calculations of mineralogy, and from experiments using the element composition measured by MESSENGER (see Section 2.2.3 below).

In summary, near-ultraviolet to near-infrared spectroscopic data from MESSENGER provided evidence for $Fe^{2+}$-poor silicate minerals and accessory phases such as graphite (P. N. Peplowski et al. 2016; R. L. Klima et al. 2018) and sulfur or chlorine-bearing minerals (F. Vilas et al. 2016; A. Lucchetti et al. 2018, 2021; O. Barraud et al. 2020, 2023). In addition to the Fe-poor mineralogy, the surface was found to be Mg rich, with moderately volatile-element-rich rocks (L. R. Nittler et al. 2011; P. N. Peplowski et al. 2011, 2014; L. G. Evans et al. 2012, 2015; P. N. Peplowski et al. 2012a; S. Z. Weider et al. 2012, 2014, 2015; P. N. Peplowski &

K. Stockstill-Cahill 2019). Four geochemical terranes were defined to address the heterogeneous distribution of mineralogy, as has been discussed above in Section 2.1.3. The mineralogy of these geochemical terranes is compatible with trachytes, intermediate between andesite and norite, and norite. If the high Na abundances in the NT can only partially be attributed to the minerals, as discussed above, the classification as trachyte might not fit, and classification as dacite would be more appropriate. Based on the elemental composition, the mineralogical classification of these geochemical terranes as boninites is also possible since they cover a large range in composition. However, boninites on Earth are unusual minerals that are formed in the context of subduction, a scenario that is very unlikely on Mercury. The special case of hollows will be discussed in Section 2.2.4 below.

Using the Mg/Si, Al/Si, and K abundance maps, P. N. Peplowski & K. Stockstill-Cahill (2019) performed a principal component analysis to identify seven compositionally distinct geochemical terranes in the northern hemisphere. Based on the element chemistry for each unit, they derived a normative mineralogy for the surface of Mercury that is dominated by plagioclase (39%–63%), pyroxene (24%–44%), and olivine (0%–36%). The plagioclase compositions tend toward albitic ($An_{0-45}$) due to the high abundance of Na, and the pyroxene component is dominated by orthopyroxene (i.e., hypersthene) over clinopyroxenes (i.e., dipside) (P. N. Peplowski & K. Stockstill-Cahill 2019).

### 2.2.3. Laboratory Studies and Modeling of Mercury's Mineralogy

O. Namur & B. Charlier (2017) performed crystallization experiments on magmas with the major element compositions and under reducing conditions expected for Mercury's mantle (with an oxygen fugacity five logarithmic units below the iron-wüstite buffer, i.e., $fO_2 = IW–5$). They investigated several mineralogical provinces: the NSP (Borealis Planitia) and the Caloris smooth plains, dominated by plagioclase, the HMR, strongly dominated by forsterite, and the intermediate plains, comprised of forsterite, plagioclase, and enstatite (Figure 8).

For the geochemical terranes introduced in Section 2.1.3, T. J. McCoy et al. (2018) calculated a hypothetical mineral assemblage from the bulk composition derived from the elemental ratios obtained by MESSENGER based on the CIPW normative calculation (Cross et al. 1903). After allocating all transition metals (Fe, Mn, Ti, Cr, Cl) to sulfides, they derived the abundance of plagioclase, pyroxene, and olivine in Mercury's various geochemical terranes (P. N. Peplowski et al. 2015; S. Z. Weider et al. 2015). These results are shown in Table 3.

Both methods estimate the plagioclase abundance of the surface between 40% and 60%, depending on location (Namur & Charlier 2017; T. J. McCoy et al. 2018). The results show that the HMR has the lowest plagioclase abundance (<40 wt%) while the Caloris interior plains have the highest plagioclase abundance (⩾60 wt%). The olivine abundance varies from 0 to 29.5 wt% across the geochemical terranes. The HMR has the highest abundance of olivine (>25 wt%) and in particular in forsterite, since all olivine is present as forsterite in the approach of McCoy (T. J. McCoy et al. 2018) because all siderophile elements (including Fe) are allocated into sulfur. The pyroxene abundance ranges between ∼25 and 50 wt% according to the geochemical terrane. The sulfide abundance is between 3.7 and 6.8 wt% (T. J. McCoy et al. 2018). The highest sulfide abundance is derived in the HMR while the
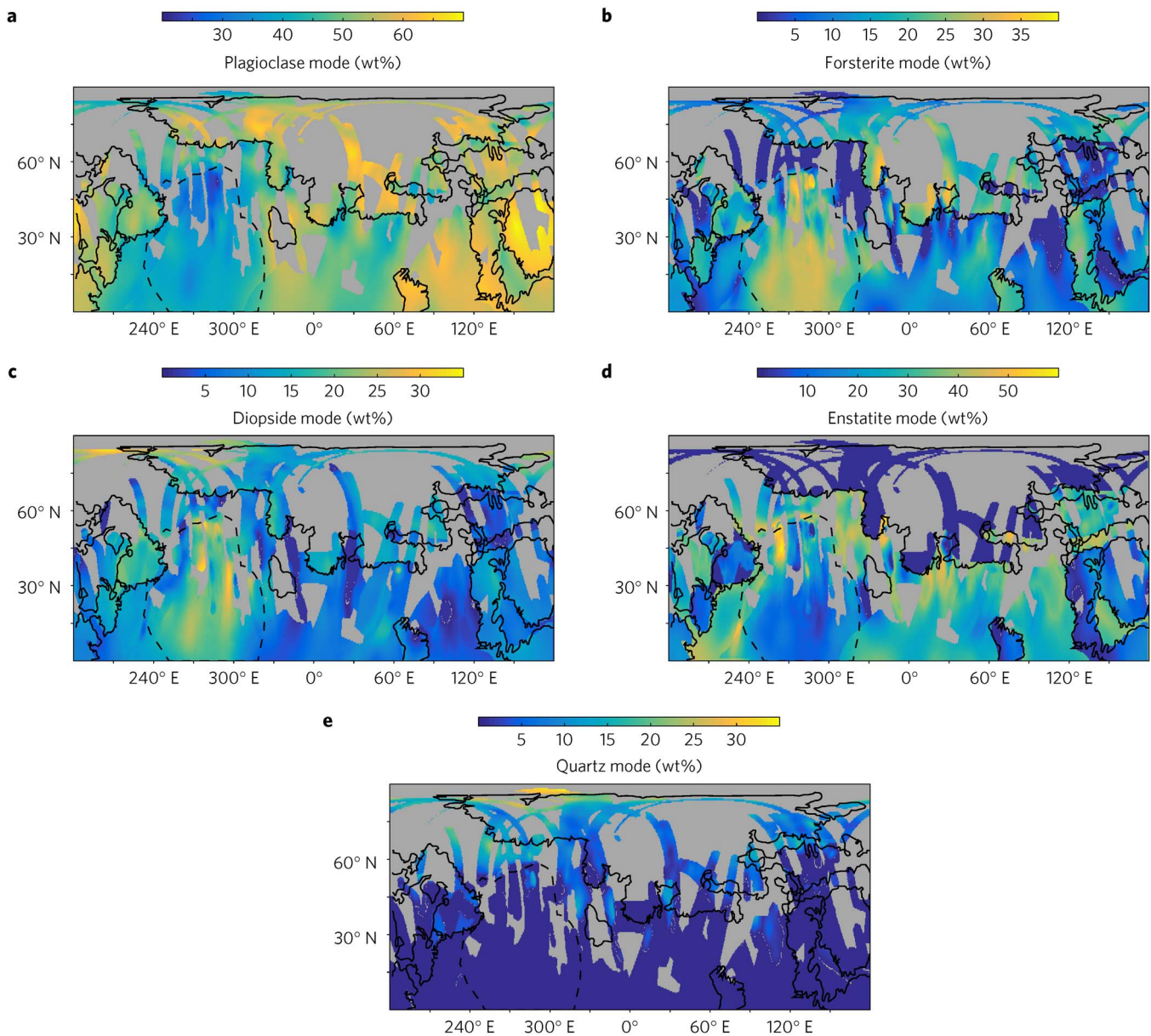
**Figure 8.** Modeled mineralogy and mineral modes for a fully crystalline volcanic crust in the northern hemisphere of Mercury. (a) Plagioclase mode (wt%). (b) Forsterite mode (wt%). (c) Diopside mode (wt%). (d) Enstatite mode (wt%). (e) Quartz mode (wt%). Figure from O. Namur & B. Charlier (2017), with permission.

lowest content is found in the Caloris interior plains and the NSP.

Surface minerology and petrology can be derived from the chemical data either through modeling (e.g., W. Cross et al. 1902; K. E. Vander Kaaden & F. M. McCubbin 2016; S. C. Solomon et al. 2018; P. N. Peplowski & K. Stockstill-Cahill 2019) or through experiments (B. Charlier et al. 2013; O. Namur et al. 2016b; O. Namur & B. Charlier 2017). These studies indicate that Mercury's surface mineralogy is dominated by FeO-poor pyroxene (enstatite and diopside) and Mg-olivine (forsterite), sodium-rich plagioclase, Mg-Ca-Fe-sulfide assemblages (e.g., L. R. Nittler & S. Z. Weider 2019), diopside, and silicate glasses (e.g., A. Morlok et al. 2021). Variations in the amounts of these minerals can account for the different geochemical terranes observed on Mercury (L. R. Nittler & S. Z. Weider 2019). Initial studies have suggested that these mineralogies are similar to komatiitic compositions; however, later work has shown they are more

commensurate with norites, boninites, or andesitic rock types (e.g., S. Z. Weider et al. 2015; K. E. Vander Kaaden et al. 2017; L. R. Nittler & S. Z. Weider 2019; P. N. Peplowski & K. Stockstill-Cahill 2019). Using mineralogies derived from melting experiments, L. R. Nittler et al. (2018) showed that Mercury's bulk chemistry is consistent with enstatite chondrite meteorites where the Si-rich metallic melt component has been removed. There are similarities in the geochemical behavior of aubrite meteorites to experimentally determined magmatic systems on Mercury, making this subset of enstatite-rich meteorites a natural petrologic analog for Mercury (Z. E. Wilbur et al. 2022).

One component of the lunar surface regolith that has been examined in more detail by infrared spectroscopy in the laboratory is the glass component. Endogenic sources of glass include those formed during pyroclastic eruptions and those formed via magma quenching (e.g., A. Morlok et al. 2021). Mercury's surface is also expected to contain a high

**Table 3**
Composition of the Derived Mineralogy (in Modal Abundance) of Geochemical Terranes on Mercury (from T. J. McCoy et al. 2018)

|  | Southern Hemisphere | Northern Latitudes | Low Fast | High Magnesium | Caloris Interior Plains |
|---|---|---|---|---|---|
| Plagioclase | 50.4 | 55.7 | 48.2 | 37.4 | 57.7 |
| Or | 0.8 | 1.3 | 1.0 | 0.6 | 0.5 |
| Ab | 29.2 | 54.3 | 30.7 | 27.0 | 30.7 |
| An | 20.4 | 0.0 | 16.5 | 9.8 | 26.5 |
| Pyroxene | 37.3 | 29.0 | 47.5 | 26.2 | 32.8 |
| Di | 5.4 | 20.0 | 4.8 | 17.8 | 0.0 |
| Hy | 31.9 | 9.0 | 42.7 | 8.4 | 32.8 |
| Olivine | 7.5 | 7.5 | 0.0 | 29.5 | 0.0 |
| Sulfides | 4.7 | 4.3 | 3.7 | 6.8 | 3.7 |
| Accessory | None | None | Qz | None | Qz, Cor |

**Note.** The definition of the terranes is given in Section 2.1.3 and Figure 6. Mineral abbreviations: Or: orthoclase; Ab: albite; An: anorthite; Di: diopside; Hy: hypersthene; Qz: quartz; Cor: corundum.

concentration of impact-derived glasses (e.g., M. J. Cintala 1992; F. Hörz & M. Cintala 1997; Y. Langevin 1997; J. Warell et al. 2010; S. L. Murchie et al. 2015; A. Morlok et al. 2021). In addition to impact-derived glasses, another exogenic source of glass production is space-weathering processes (C. M. Pieters & S. K. Noble 2016). Laboratory experiments with lunar samples and synthetic glasses show that Mg-rich glasses can reproduce several of the mid-infrared spectral features observed by ground-based telescopes (A. Morlok et al. 2021).

Many laboratory studies of Mercury's plausible mineralogy have focused on the thermal infrared spectral range in preparation of Mercury Radiometer and Thermal Infrared Spectrometer (MERTIS) observations (H. Hiesinger et al. 2020) from the BepiColombo spacecraft. The spectral properties vary with temperature, which varies over a large range at Mercury. A review of this work is provided in the companion paper by F. Leblanc et al. (2023).

### 2.2.4. Hollows on Mercury

Several of the geological units observed by MESSENGER are linked to the surface manifestation of volatile species on Mercury. In this context, we discussed explosive volcanism above. There are other geomorphologic features, namely hollows (e.g., D. T. Blewett et al. 2013), red pitted ground (R. J. Thomas et al. 2014), pyroclastic deposits (e.g., L. Kerber et al. 2011), and ejecta (e.g., J. Wright et al. 2020) that have been associated with Mercury's volatile content. Ejecta blocks within the Caloris basin ejecta also display morphologies associated with devolatilization (J. Wright et al. 2020). The morphology of knobs within these ejecta are similar to that of molards, with a subset of knobs displaying hollows (J. Wright et al. 2020). Spectrally red pits, which have been proposed to be of pyroclastic origin (e.g., L. Kerber et al. 2011), are also highly associated with hollows (R. J. Thomas et al. 2014), implying a connection with the presence of volatiles. Glacial-like flows within the Raditladi basin, also characterized by the presence of hollows, add additional support to the exhumation of a highly volatile layer within the crust (Rodriguez et al. 2023) that has been suggested to explain the morphology of chaotic terrains (J. A. P. Rodriguez et al. 2020, 2023).

The abundance of volatile elements within Mercury's surface is particularly surprising, and the study of these geological units allows arguments to be brought about the nature, sources, and inventory of these volatile elements. In this

objective, the study of hollows and pyroclastic deposits showed interesting results.

Hollows are rimless depressions with flat floors and haloes of bright (high albedo) material surrounding them. They are geologically young features, and potentially they are currently active (D. T. Blewett et al. 2013; R. J. Thomas et al. 2014; D. T. Blewett et al. 2018). Hollows were first observed as bright areas within craters imaged by the Mariner 10 spacecraft in 1974, but these images were not of sufficient resolution to discern any detail (D. Dzurisin 1977). The formation of these features is hypothesized to involve the removal or the release of volatiles, either by thermal decomposition, space weathering, including solar heating, or the oxidation and volatilization of graphite (J. Helbert et al. 2013; R. J. Thomas et al. 2016; F. Vilas et al. 2016; D. T. Blewett et al. 2018). Hollows are predominately, though not exclusively, associated with impact features: from crater floors, walls, central peaks and peak rings, and ejecta blankets (D. T. Blewett et al. 2013). They are seen in impact craters and large pits associated with pyroclastic deposits and in low-reflectance spectral units (D. T. Blewett et al. 2013).

The basic formation concept of the hollows is vertical downward growth to an approximately constant depth via volatile removal followed by lateral enlargement by scarp retreat (e.g., D. T. Blewett et al. 2018). The downward growth is controlled either by the depletion of the volatile-bearing layer or by the development of a lag deposit that insulates the volatile substrate from further loss (e.g., D. T. Blewett et al. 2018). The combined surface area of the observed hollows is 57,400 km$^2$ (R. J. Thomas et al. 2014), and their average depth is 24 m (D. T. Blewett et al. 2016), which gives a total volume of about 1260 km$^3$ that is lost during the hollows formation, corresponding to a potential global deposit of up to 2 cm. Assuming the global surface concentrations of S and C (Table 2), the excavated volume could make up a significant fraction of the top 20 m of the surface of Mercury (Y. Wang et al. 2020).

Analyses of the morphology (D. T. Blewett et al. 2016), spatial distribution (D. T. Blewett et al. 2013; R. J. Thomas et al. 2014; 2016), spectral data (D. T. Blewett et al. 2013; F. Vilas et al. 2016; A. Lucchetti et al. 2018, 2021; O. Barraud et al. 2020, 2023; Y. Wang et al. 2020) and laboratory experiments (J. Helbert et al. 2013; C. J. Renggli & P. L. King 2018; I. Varatharajan et al. 2019) suggest that hollows are formed by the loss of volatile species from the surface. Multispectral observations of several hollows by MDIS exhibit a weak absorption band around 630 nm wavelength. This
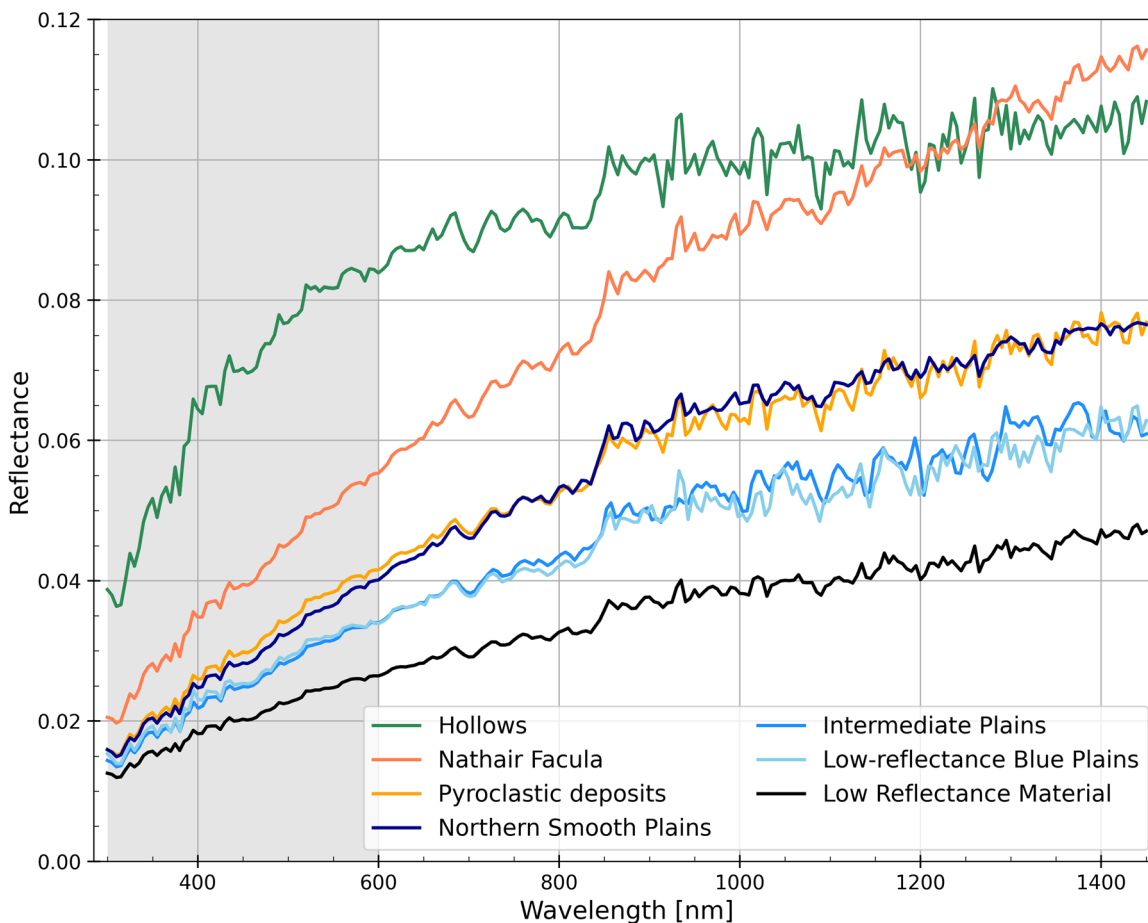
**Figure 9.** Typical reflectance spectra of some major and minor spectral units measured by MASCS/VIRS. Localization of the spectra used for the hollows, LRM, and NSP are detailed in O. Barraud et al. (2020). Spectra used for the Nathair Facula and pyroclastic deposits are from O. Barraud et al. (2021). Hollows exhibit a strong concave curvature between 300 and 600 nm (shaded region) compared to other spectral units.

absorption feature is commonly attributed to the presence of sulfides, chlorides, and/or graphite (F. Vilas et al. 2016; A. Lucchetti et al. 2018, 2021). Reflectance spectra obtained by MASCS show in the near-ultraviolet to visible spectral regions a strong curvature that is unique to hollows material (see Figure 9 and O. Barraud et al. 2020). Comparison with laboratory measurements on surface analog materials (e.g., I. Varatharajan et al. 2019) revealed that sulfides and/or chlorides may be responsible for this peculiar spectral feature (O. Barraud et al. 2023). Based on spectroscopic information from MESSENGER, the most often proposed candidates for the active minerals in the formation of the hollows are magnesium and calcium sulfides (e.g., F. Vilas et al. 2016; A. Lucchetti et al. 2018; O. Barraud et al. 2020, 2023). These observations are corroborated by the element composition of Mercury's surface and by laboratory experiments (J. Helbert et al. 2013; C. J. Renggli et al. 2022). The correlation between Mg and S as well as Ca and S abundances at the surface of Mercury suggests the presence of MgS and CaS (L. G. Evans et al. 2012; C. Cartier et al. 2020). Figures 2 and 4 show the tight correlation of Ca with S, with the Ca/S ratio being constant almost globally. Similarly, a tight correlation between Mg and S is observed (compare panels (a) and (b) of Figure 2); thus, a globally constant Mg/S ratio can also be inferred.

Spectroscopic measurements in the laboratory on CaS and MgS before and after thermal processing at temperatures appropriate to Mercury's dayside display an absorption feature

at or around 600 nm (J. Helbert et al. 2013). These measurements also demonstrated that sulfides can be thermally decomposed at temperatures of approximately 500°C, i.e., below their melting point, which are temperatures consistent with Mercury's surface conditions on the dayside (J. Helbert et al. 2013). In addition, experiments indicate that reactions between magmatic sulfur and silicates under the conditions of Mercury's surface provide materials with the same morphologic characteristic of the hollows (C. J. Renggli et al. 2022). Those experiments suggest that magmatic volatiles are the source of the components responsible for hollows formation. Volcanic activity has been proposed among the possible sources of volatiles based also on MESSENGER observations (D. T. Blewett et al. 2013; O. Namur et al. 2016a). However, other hypotheses, such as LRM excavated by impact cratering (D. T. Blewett et al. 2013; R. J. Thomas et al. 2016; Y. Wang et al. 2020) or differentiation inside impact melts (W. M. Vaughan et al. 2012), have also been proposed as the source of these volatiles.

Pyroclastic deposits are the result of explosive volcanism caused by either magma compositionally dominated by volatiles or by the interaction of magmas with highly volatile-rich crustal components. These deposits on Mercury display different spectral features compared to the hollows, which have approximately twice the average reflectance of Mercury (L. Kerber et al. 2009, 2011; O. Barraud et al. 2020; M. Pajola et al. 2021) and may present common volatile species, as already demonstrated by laboratory experiments

(C. J. Renggli et al. 2022). The extent of pyroclastic deposits is proportional to the amount of volatiles needed for their emplacement (S. Besse et al. 2020; O. Barraud et al. 2021). Depending on the volatile species considered (e.g., $H_2O$, CO, $CO_2$, $H_2S$, $SO_2$), extrusive volatile content derived for Mercury are comparable or higher than those observed on the Earth (regardless of whether the volatile content is an inherent component of the magma or is generated from interactions of the magma with crustal components), which demonstrates again that Mercury is a volatile-rich planet. The volatile species driving explosive activity on Mercury will most likely be a combination of several volatiles, including S and C. As already mentioned, XRS and NS observations show that Nathair Facula, the largest pyroclastic deposit on Mercury, is depleted in S and C compared with the rest of the surface (S. Z. Weider et al. 2016), which suggests that these species have been lost during eruption processes. Spectroscopic observations agree with these results (O. Barraud et al. 2021). Laboratory experiments designed to reproduce the interaction between supersolidus Hermean magmas and graphite at high temperatures and low pressures suggest that interaction between these magmas and graphite leads to a smelting process that reduces the FeO in the melt and releases CO and $CO_2$ gas (K. Iacovino et al. 2023). The results suggest that, if the graphite-smelting processes are active, the gas produced by smelting alone can be responsible for more than 75% of the pyroclastic deposits (K. Iacovino et al. 2023). Moreover, a combination of S-H degassing and $CO–CO_2$ production from smelting can explain all pyroclastic deposits, except Nathair Facula (K. Iacovino et al. 2023).

### 2.2.5. Expected Understanding of the Global Surface Mineralogy from BepiColombo

The Mercury Planetary Orbiter (MPO) of BepiColombo (J. Benkhoff et al. 2021) will be in a close and low-eccentricity orbit around Mercury, providing much better observation conditions of the entire surface of Mercury for infrared spectroscopy by the Scientific Cameras and Spectrometer for the BepiColombo Mission (SIMBIO-SYS) and MERTIS instruments, and for element maps by the X-ray (Mercury Imaging X-ray Spectrometer; MIXS) and gamma-ray (Mercury Gamma-ray and Neutron Spectrometer; MGNS) instruments.

It is expected that, on BepiColombo, the MERTIS instrument (wavelength regions of 7–14 and 7–40 $\mu$m; H. Hiesinger et al. 2020) and the SIMBIO-SYS instrument (visible and near-infrared hyperspectral imaging channel, wavelength range 400–2000 nm; G. Cremonese et al. 2020) will record diagnostic spectral signatures of mineralogy. Spectral information in the mid- and thermal infrared wavelength range provides important insights into the nature of the materials that make up the surface of Mercury. There is also a mass spectrometer for in situ measurements of the chemical composition of the exosphere, the STart from a ROtating Field mass spectrometer (STROFIO) instrument, which is part of the Search for Exospheric Refilling and Emitted Natural Abundances (SERENA) experiment (S. Orsini et al. 2021). MERTIS will provide global mineralogical maps with spatial resolution of about 500 m and for approximately 5%–10% of the surface, a spatial resolution better than 500 m (H. Hiesinger et al. 2020). The visible and near-infrared hyperspectral imaging channel of the SIMBIO-SYS instrument will provide global maps at 480 m px$^{-1}$, with the spectral information and spatial resolution

reaching 120 m px$^{-1}$ in selected areas (G. Cremonese et al. 2020). This is about a tenfold increase in spatial resolution compared to the 5 km spatial resolution available from VIRS/MASCS on MESSENGER (W. E. McClintock et al. 2007).

SIMBIO-SYS is expected to provide information on effusive and explosive deposits and on potential intrusive bodies to infer Mercury magma genesis and consequent crustal formation and evolution. In the near-infrared spectral region covered by SYMBIO-SYS, some of the diagnostic signatures are the slopes of the spectra at wavelengths shorter than 0.75 $\mu$m in addition to spectral features. Examples of the latter are the sulfide absorption band around 0.63 $\mu$m, the orthopyroxene band around 0.9 $\mu$m, absorption features of oldhamite at ~0.495 and 0.951 $\mu$m, the ferrous iron absorption at 1 $\mu$m, and the Ca-rich pyroxene signature at 1.1 $\mu$m. The OH feature at about 2.2 $\mu$m of hydroxyl-bearing minerals, and the chlorites band in the range of 2.2–2.4 $\mu$m, are slightly outside the covered wavelength region (V. Shankar 2015; X. Liancun et al. 2017). A more complete list of spectral features of minerals in the near-infrared spectral region can be found in the reviews of V. Shankar (2015) and X. Liancun et al. (2017).

In the thermal infrared spectral regions covered by MERTIS, some of the diagnostic signatures are the Christiansen feature (CF), an emissivity maximum (EM) centered near 8 $\mu$m for silicates, the Reststrahlen bands (RB), and the transparency feature (TF). Some of the diagnostic signatures covered by MERTIS are the plagioclase CF feature around 8 $\mu$m, which can be used to distinguish plagioclase composition (D. B. Nash & J. W. Salisbury 1991), the TF in the range 12–12.5 $\mu$m, the EM in the range 8.0–8.4 $\mu$m, and the RB in the range 11.0–12.5 $\mu$m (K. L. Donaldson Hanna et al. 2012). The pyroxene features around 5 $\mu$m (C. H. Kremer et al. 2023) are outside the MERTIS wavelength region. Basalt signatures are around 6.5 and 9.5 $\mu$m, the $H_2O$ band at 5.8–7.5 $\mu$m, the OH band at 9.4–23 $\mu$m, and the olivine RB and TF bands at 9.0–50 $\mu$m, which can be used to assess the fosterite fraction (V. E. Hamilton 2010), and the pyroxene TF feature at about 11.5 $\mu$m (A. Sprague et al. 2007). For more information, the papers by H. Hiesinger et al. (2010) and D. A. Rothery et al. (2020) both describe the possible contributions by MERTIS to the investigation of Mercury's mineralogy in detail. Laboratory studies for Mercury using a binary mixture of a volcanic regolith-like sample and oldhamite (CaS) show how the position of the CF is strongly driven by the oldhamite in the mixtures, whereas the positions of the RB minima are mainly dominated by mafic composition (C. Carli et al. 2024). The spectral contrast between the RB and CF is strongly reduced in the mixtures with respect to the end-members, but is sufficient for investigation by MERTIS (C. Carli et al. 2024).

## 3. Sources of Refractory and Volatile Elements in Mercury's Exosphere

There are four processes that release material from the surface into the exosphere: (1) thermal release; (2) photon-stimulated desorption (PSD); (3) ion-induced sputtering; and (4) micrometeoroid impact vaporization (MIV); see the review by P. Wurz et al. (2022) for detailed descriptions of these processes. In the case of ion-induced sputtering, the limited access of solar wind plasma to the surface because of the shielding by Mercury's magnetosphere must be considered (P. Wurz et al. 2022). Thermal release (including sublimation) is relevant for volatile species, e.g., water, $CO_2$, and other

gases. Also, atomic Na and K on the surface have a high enough vapor pressure at the temperatures at Mercury's dayside that their sublimation contributes to the exosphere particle population. PSD causes the release of atoms by electronic excitations in the surface by absorption of ultraviolet photons and is relevant mostly for the release of Na and K from the surface. Electron-stimulated desorption (ESD) operates the same way but by the irradiating electrons causing the electronic excitation and subsequent release. Sputtering is the release of atoms and molecules from the solid surface upon ion impact; sputtering is responsible for releasing the refractory species into the exosphere. The constant flux of micrometeoroids onto Mercury's surface contributes everything to the exosphere that was the volume excavated by impactors, where part of the released material is in larger pieces and part is in the gas phase.

In all observations of Mercury's exosphere, only atomic species have been observed. Similarly, for most of the exosphere modeling, only atomic species have been considered. This has been reviewed in detail earlier (P. Wurz et al. 2022) and is not repeated here. However, there is indirect evidence in the exosphere observations that polyatomic species might be released as well. In the following, we will discuss the evidence for the release of such species during sputtering and MIV based on laboratory experiments, micrometeoroid impact modeling, and inferences from observations.

### 3.1. Sputtering of Mineral Surfaces

#### 3.1.1. Ion-induced Sputtering of Polyatomic Neutral Compounds

The impact of energetic ions or neutral atoms from the solar wind plasma on solid surfaces will cause the release of atoms and molecules from the topmost 2–3 atomic layers of the surface. The solar wind energies are about $1\,keV\,amu^{-1}$, corresponding to solar wind speeds of about $440\,km\,s^{-1}$, which is close to the average of observed solar wind speeds (Y.-M. Wang 1994; F. M. Ipavich et al. 1998; A. R. Breen et al. 2002). This release process is called particle-induced sputtering, or sputtering, and has been studied in detail in surface-state physics for many decades (A. Benninghofen et al. 1987; R. Behrisch & W. Eckstein 2007). Recent reviews on sputtering induced by ion bombardment are provided by R. A. Baragiola (2004) and P. Sigmund (2012), and in the context of Mercury and the Moon, by P. Wurz et al. (2022). At typical solar wind speeds, sputtering occurs in the nuclear interaction regime, where the sputter yield has a maximum at an energy around $1\,keV\,amu^{-1}$ of the impacting ions (Wurz 2012). With the typical sputter yield of minerals and the integrated ion flux onto Mercury's surface of $1.1 \cdot 10^{25}$–$3 \cdot 10^{26}\,s^{-1}$, a global sputter rate of $(0.36$–$9.8) \cdot 10^{-11}\,m\,a^{-1}$ is obtained, which is comparable to the lunar sputter rate of $4 \cdot 10^{-11}\,m\,a^{-1}$ (P. Wurz et al. 2010). For materials of interest here—the rocks and regolith on Mercury's surface— sputtering is the result of the nuclear interaction of the projectile ion with the sample material (G. Betz & K. Wien 1994). Toward lower particle energies, the sputter yield goes to zero because the energy deposited by the impacting ion is not sufficient to overcome the binding energy of atoms at the surface; for energies much higher, the sputter yield also goes to zero because the ions penetrate deeper into the solid without depositing sufficient energy at or near the surface to cause the release of particles. Sputtered particles are emitted from a depth much shallower than the penetration depth of the impacting particles, which ranges from a depth of 30 nm for solar wind He,

to 0.1 mm for energetic protons of a few MeV, and to about 1 m for Galactic cosmic rays with GeV. These define the range of space weathering caused by impacting particles.

Current laboratory investigations of ion-induced sputtering on materials relevant to Mercury and the Moon are discussed in Section 5.2, and modeling of sputtering and space weathering of such materials is discussed in Section 5.3. When studying sputtering in the context of planetary science, most studies have only considered the release of atoms. However, laboratory experiments from the surface physics research domain provided ample evidence that not only atoms are sputtered from metal and insulating surfaces by ion impact, but also polyatomic compounds and clusters. Unfortunately, such studies do not exist on rock-forming minerals. In sputtering of pure metals or metal alloys (although unlikely materials on Mercury's surface), the formation of metal clusters has been observed, with these clusters containing up to tens of atoms (H. Gnaser & W. O. Hofer 1989; K. Franzreb et al. 1991; A. Wucher et al. 1993; M. Wahl & A. Wucher 1994; A. Wucher & M. Wahl 1996; C. Staudt et al. 2000), with the yield of clusters decreasing as the cluster size increases. The fraction of clusters in the sputtered flux is also a function of the total sputter yield, as was observed, for example, for the ratio of sputtered metal dimers to atoms (P. Wurz et al. 1991), with dimer yields expected in the per mil range for solar wind ion energies.

For oxide surfaces, sputtering of metal oxide molecules in the form $M_xO_y$ has been observed, where $x$ and $y$ are integer numbers, with significant sputter yields of these polyatomic compounds (H. Oechsner et al. 1978; A. Wucher & H. Oechsner 1986). Figure 10 shows an example for sputtering of metal oxides where the yield of the compound molecules is even larger than the yield of sputtered atoms (H. Oechsner et al. 1978), even at impact ion energies lower than typical solar wind energies.

#### 3.1.2. Ion-induced Sputtering of Polyatomic Ionized Compounds

In addition to neutral species being sputtered, a large fraction of particles are also sputtered as ions, both positive and negative. For metals, sputtered clusters with sizes of up to several tens of atoms have been observed, both as positive and negative ions (I. Katakuse et al. 1985). Yields of sputtered ions from pure metals are typically low compared to sputtered neutral species, in the range of $10^{-2}$–$10^{-4}$ (A. Benninghoven 1975; Benninghoven et al. 1987). However, laboratory experiments show that the yield of sputtered metal clusters compared to sputtered atoms is much higher for ionized species than for neutral sputter products (H. Gnaser & W. O. Hofer 1989; K. Franzreb et al. 1991).

For metal oxides, which are much more applicable to planetary surfaces, metal oxide compounds in the form $M_xO_y$ are also sputtered as negative and positive ions (A. Benninghoven 1975; C. Plog et al. 1977). Yields for sputtered ions from oxides can be as high as the neutral sputter yields (Benninghoven et al. 1987). Investigations have been performed for many metal oxides. The relative yields of $M_xO_y$ ions vary with element and number of atoms of metal oxide. The most abundant sputtered ion can be either M, MO, or $M_xO_y$ (A. Benninghoven 1975; C. Plog et al. 1977; Benninghoven et al. 1987). The abundance distributions of negative and positive $M_xO_y$ ions are also different, depending on the oxide.
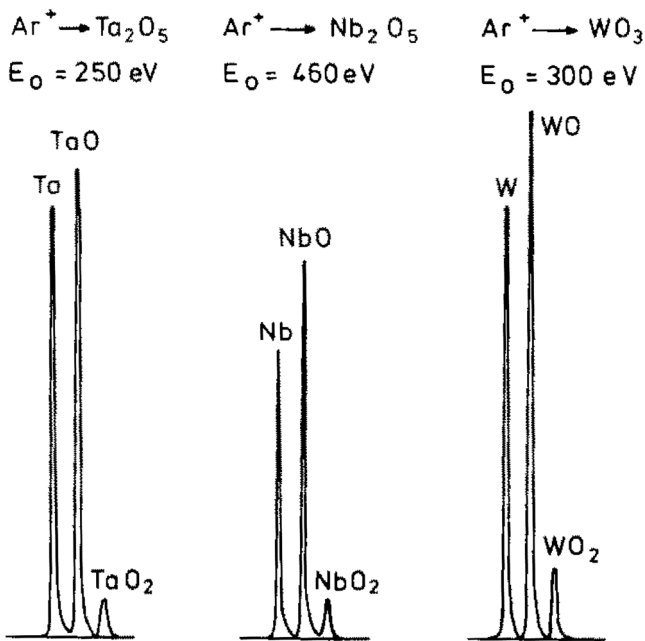
**Figure 10.** Parts of mass spectra of sputtered neutrals from anodic oxide layers on polycrystalline Ta, Nb, and W for perpendicular bombardment with $Ar^+$ ions of different energies (from H. Oechsner et al. 1978, with permission).

Similar results were observed for sputtering of Ca metal samples (C. S. Hansen et al. 1998, 1999). Because Ca metal oxidizes very quickly, an oxide layer formed on top of the metal, and Ca metal clusters and $Ca_xO_y$ oxide molecules were seen in the flux of sputtered particles, each with abundances of about 0.1 compared to the Ca atom sputter yield. For a thick calcium oxide surface, sputtered compounds such as $Ca_xO_y$, with $x = 1$–$4$ and $y = 0$–$4$, as well as $Ca_4O_5$, $Ca_5$, and $Ca_5O_2$ were observed in comparable quantities (C. S. Hansen et al. 1999). Also, for Ca clusters and oxides, the energy distributions show the typical shape of sputtered species, as discussed before (C. S. Hansen et al. 1999). Ca-bearing minerals, like anorthite, diopside, and sulfides, are part of the derived mineralogy on Mercury's surface (see Table 3), and metallic or atomic Ca, which is possibly present on the surface, will be oxidized with about 1000 yr, or will form sulfides from oxygen and sulfur atoms returning from the exosphere.

The ion emission due to solar wind ion impact on lunar analog material was studied in laboratory experiments (R. C. Elphic et al. 1991). The range of relative atomic ion yields covered four decades of variation depending on the sputtered ion species. In addition to atomic ions, the oxide ions $AlO^+$, $SiO^+$, $TiO^+$, and $FeO^+$ were also observed at comparable quantities. These measurements show that the ion yield depends exponentially on the ionization potential of the sputtered species (R. C. Elphic et al. 1991).

### 3.1.3. Energy Distributions of Sputtered Polyatomic Species

The kinetic energy distributions of sputtered neutral metal clusters and neutral oxide molecules are similar to the energy distributions of sputtered neutral atoms; they rise with the energy of the sputtered particle up to a peak around a few eV, at similar or slightly lower energies than for atoms, and then fall off with a power law (H. Gnaser & W. O. Hofer 1989; A. Wucher et al. 1993; M. Wahl & A. Wucher 1994;

R. Behrisch & W. Eckstein 2007). As a general trend, the larger the metal cluster or the oxide molecules, the steeper the falloff at higher energy.

For reference, the energy distribution for atoms sputtered from a solid, $f(E_e)$, with the energy $E_e$ of the sputtered particle, has been given as

$$f(E_e) \propto \frac{E_e}{(E_e + E_B)^3} \qquad (1)$$

and is known as the Sigmund–Thompson energy distribution of sputtered atoms (P. Sigmund 1969; M. W. Thompson et al. 1986); with respect to planetary science (P. Wurz et al. 2022), $E_B$ is the binding energy of the sputtered atom, with $E_B$ usually assumed to be the heat of sublimation. Note that, for high energies of sputtered atoms, the distribution falls off with $E_e^{-2}$. For sputtering of polyatomic species, the energy distribution is given by

$$f(E_e) \propto \frac{E_e}{(E_e + E_B)^k}, \qquad (2)$$

where the exponent $k$ is in the range of four to five for polyatomic species consisting of up to seven atoms (G. Betz & W. Husinsky 2004). Thus, in contrast to sputtered atoms, the energy distribution of sputtered polyatomic species falls off more steeply with $E_e^{-3}$ to $E_e^{-4}$. As an example, Figure 11 shows energy distributions of atoms and clusters sputtered from a Cu metal sample. Unfortunately, such measurements are not available for mineral samples relevant for Mercury or the Moon.

### 3.1.4. Lifetime of Sputtered Neutral and Ionized Polyatomic Species

In sputtering, the impact of an energetic ion on the surface creates a collision cascade along the trajectory of the particle until it comes to rest. The volume covered by this collision cascade can be understood as being locally at high temperatures of a few thousand Kelvins. Thus, the polyatomic compounds released from the surface via sputtering will have substantial internal energies, i.e., by vibration and rotation excitations, expressed as internal temperatures of several 1000 K (R. Behrisch & W. Eckstein 2007; A. Wucher et al. 2008). This internal excitation will result in the unimolecular decay of these polyatomic compounds while they are on their trajectory in the exosphere, and thus limit their lifetime in a planetary exosphere. The decay of these compounds creates a source of atomic species somewhere in the exosphere. Note that this unimolecular decay happens without any external agents, only because of the high internal energy. External agents, like UV photons or particle collisions, will shorten the lifetime of these compounds in the exosphere. Table 4 lists a few examples of measured internal temperatures of sputtered polyatomic compounds; measurements on materials relevant for Mercury and the Moon are not available so far. Lifetimes, $t_n$, resulting from unimolecular decay depend on the actual internal temperatures and the compound itself, and can be estimated for polyatomic compounds consisting of $n$ atoms from (A. Wucher et al. 2008)

$$t_n = \frac{1}{\nu g} \left( 1 - \frac{D_n}{E_{int}} \right)^{1-s}, \qquad (3)$$

where $\nu$ is the typical vibration frequency ($10^{12}$–$10^{13}$ Hz), $g$ is a degeneracy factor, $s = 3n - 6$ is the number of vibrational
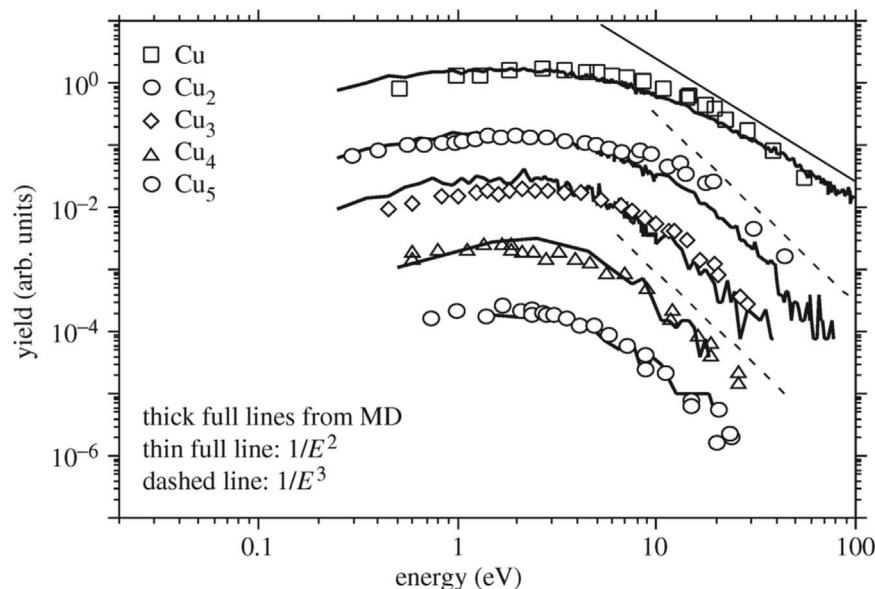
**Figure 11.** Energy distributions (flux) of Cu atoms and Cu clusters up to $Cu_5$ (data points) sputtered with 3.9 keV Ar ions (S. R. Coon et al. 1993) together with simulations for atoms, dimers, trimers, quatromers, and pentamers for 5 keV Ar ions on Cu (111) from a molecular dynamics calculation (solid lines: G. Betz & W. Husinsky 2004). The simulated cluster yields have been normalized to the experimental results. Asymptotic distributions for $E_e^{-2}$ to $E_e^{-3}$ are shown as thin solid and dashed lines, respectively. Figure from S. R. Coon et al. (1993), with permission.

**Table 4**
Examples of Measured Internal Energies (Expressed as Temperatures) of
Sputtered Polyatomic Compounds

| Molecule | Temperature | References |
|---|---|---|
| $S_2$ | 1500 K (vibration) | R. De Jonge et al. (1987) |
| | 300–1600 K (rotation) | |
| $Cs_2$ | 1470 K | P. Fayet et al. (1986) |
| $K_2$ | 1025 K | P. Fayet et al. (1986) |
| $Na_2$ | 1000 K | P. Fayet et al. (1986) |
| $Ag_2$ | 2700 K (vibration) | A. Wucher (1994) |
| | 6700 K (rotation) | |
| AlO | 5000 K (vibration) | O. Varenne et al. (2000) |
| | 13,000 K (rotation) | |
| CH | 4500 K | G. E. Thomas et al. (1975) |

degrees of freedom of the polyatomic compound, $E_{int}$ is the internal excitation energy, and $D_n$ is the dissociation threshold. The lifetime of polyatomic compounds will range between seconds and tens of minutes for typical planetary situations. When a polyatomic compound breaks apart in the exosphere, at some height above the surface, the binding energy will be released to the fragments as additional kinetic energy. This additional energy of the fragments, e.g., atoms, will add to the characteristic energy of these species in the exosphere, thus increasing altitudes of the fragment atoms. The characteristic energy of these species is easily observed as scale height in the exosphere. In optical observations of density profiles of an exosphere, the high scale height, resulting from the high characteristic energy, is often also referred to as the temperature of the species.

The unimolecular decay of polyatomic species released via sputtering or MIV (see below) will not release large amounts of excess energy that could explain the high energies observed for some atomic species. However, photodissociation of polyatomic species can release the necessary energies. R. R. Valiev et al. (2017, 2020) calculated the photodissociation lifetime and excess energy released upon photodissociation for several diatomic species possibly released from the minerals at planetary surfaces. They found that the maximal order of photodissociation cross sections for the alkali metal monoxides reaches about $10^{-17}$ cm$^2$. By comparison, the photodissociation cross sections for alkaline earth monoxides do not exceed the order of $10^{-18}$ cm$^2$. For example, CaO has a low photodissociation cross section, but still potentially large enough to explain some of the Ca observations, which are discussed below.

### 3.1.5. Observations of Molecules and Clusters from Sputtering

Sputtering of polyatomic species has been inferred from observations of atomic species; however, no direct observation of polyatomic species in the exosphere of Mercury or the Moon has been accomplished so far. Atomic Ca was optically observed in Mercury's exosphere by ground-based observations (T. A. Bida et al. 2000). The large-scale height of the observed Ca and the associated mean kinetic energy of the Ca atoms were interpreted due to a high temperature of about 12,000 K being responsible for the scale height, which was attributed to ion sputtering. Exosphere modeling showed that this density profile could indeed be produced by ion sputtering (P. Wurz et al. 2010). Extended ground-based observations found Ca mostly in Mercury's polar exosphere again showed high mean energies that were interpreted as temperatures in the range of 12,000–20,000 K. The observed velocities are more than possible for a ballistic trajectory of a Ca atom from the surface and require a source of additional energy (R. M. Killen et al. 2005). The authors suggested that impact vaporization in the form of CaO and clusters, or ion-sputtering of atoms, molecules, and ions, are the source of the observed Ca in the exosphere, where the CaO and clusters released from the surface subsequently dissociate somewhere along their exospheric trajectory and release the excess energy to the
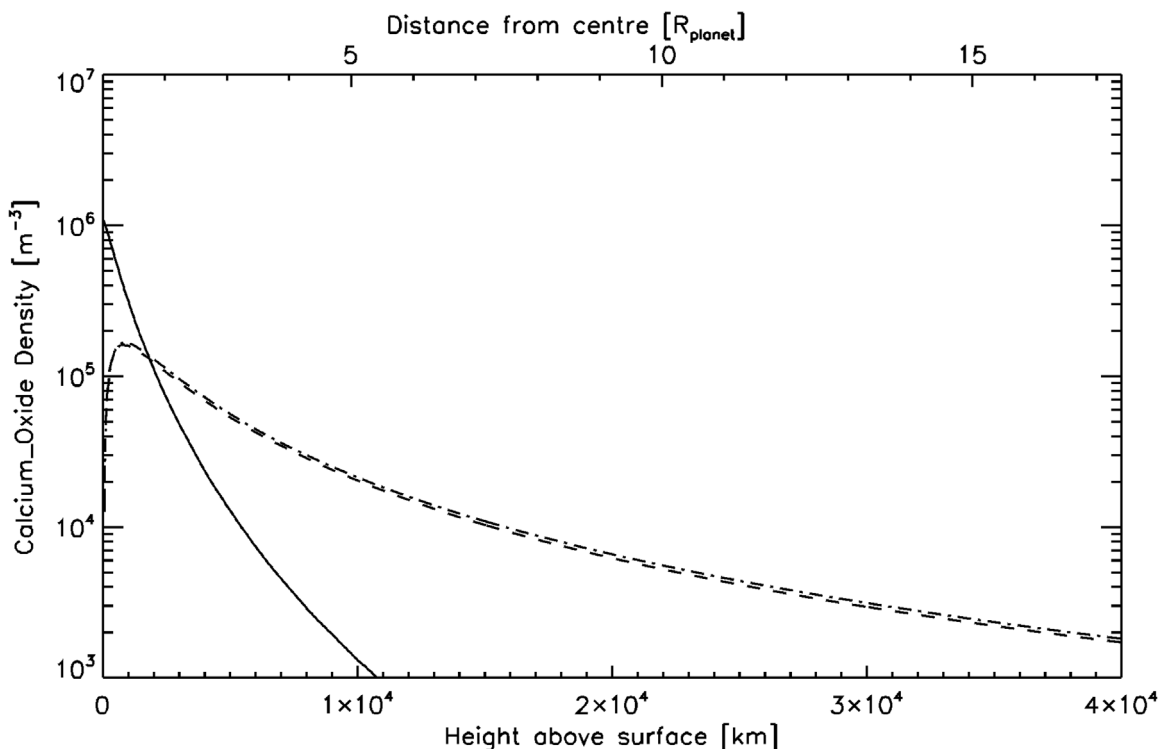
**Figure 12.** Calculation of density profiles in Mercury's exosphere for sputtered CaO (solid line) and its fragments Ca (dashed line) and O (dashed–dotted line) resulting from photodissociation of sputtered CaO along its trajectory in the exosphere.

fragments. From laboratory studies, it is known that, for a Ca oxide surface, the yield of sputtered CaO is about half of the Ca atom yield (C. S. Hansen et al. 1999).

Figure 12 shows a calculation of the exospheric density profile for CaO being sputtered from Mercury's surface using the Monte Carlo code for Mercury's exosphere (P. Wurz & H. Lammer 2003; P. Wurz et al. 2010). Because of unimolecular decay of the hot CaO molecule, it decays along the trajectory into its fragments Ca and O, for which the resulting density profiles are also shown in Figure 12. The density profiles for Ca and O fall off much more slowly with altitude than the CaO, showing that the fragments have higher characteristic energies, which can be interpreted as higher temperatures.

The calculation shown in Figure 12 allows one to compare with the measured density profiles as well as other quantities that have been observed for Ca in Mercury's exosphere, such as the line-of-sight velocity (tangential velocity) and the radial velocity of the Ca atoms (R. M. Killen et al. 2005). Figure 13 shows the comparison of model results for the calculated density (Figure 13, top panel), line-of-sight velocity (Vxy in Figure 13, middle panel), and radial velocity (Vzw in Figure 13, bottom panel) with the observations of R. M. Killen et al. (2005). Even though R. M. Killen et al. (2005) speculated that CaO is released via MIV, sputter release was used in the model for Figure 13, and it is found that the density profiles agree quite well considering the natural variation of the sputtered signal. In particular, the dependence with altitude, interpreted as temperature by the observers, agree nicely. The comparison of the radial velocities shows that the agreement with the calculations for Ca from sputtered CaO is better than for sputtered Ca. This supports the interpretation that sputtered

CaO is the origin of the observed Ca with large-scale heights in the exosphere of Mercury.

### 3.2. Micrometeoroid Impact Vaporization

#### 3.2.1. Particle Release by Micrometeoroid Impact Vaporization

Micrometeoroids impacting on a solid surface at hypervelocities create an impact plume of high temperature and density. Small meteoroids with radii in the range $10^{-8}$–$10^{-2}$ m strike Mercury's surface with velocities in the range of 10 and 40 km/s; larger meteoroids of 1–10 cm size strike Mercury's surface with velocities between 20 and 70 km s$^{-1}$ (M. J. Cintala 1992). The total mass of excavated material from a micrometeoroid impact can be anywhere from $10^3$ to $10^6$ times the mass of the impactor, depending on the sample material properties (see the review by P. Wurz et al. 2022). The impact plume thus consists of mostly surface material, being a mix of broken fragments of minerals or rock, melt, all the way to atoms and molecules.

The exosphere population resulting from MIV is modeled as a thermal release of particles from the impact location with typical average temperatures of the released gas of 3500 K (G. Eichhorn 1976, 1978; P. Wurz et al. 2022). The initial impact plume at the surface is much hotter and very dense, but the observed exosphere is at much larger spatial scales than the actual impact plume and represents the final state of the expansion of the plume. For micrometeoroid impacts on Mercury's surface, the estimated initial parameters of the impact plume are a temperature of $T_0 = 10,000$ K and a pressure of $P_0 = 10,000$ bars (A. A. Berezhnoy & B. A. Klumov 2008). As the impact plume expands, the pressure decays, and it cools off. The pressure varies within the impact plume, and a significant portion has a much lower pressure than the initial
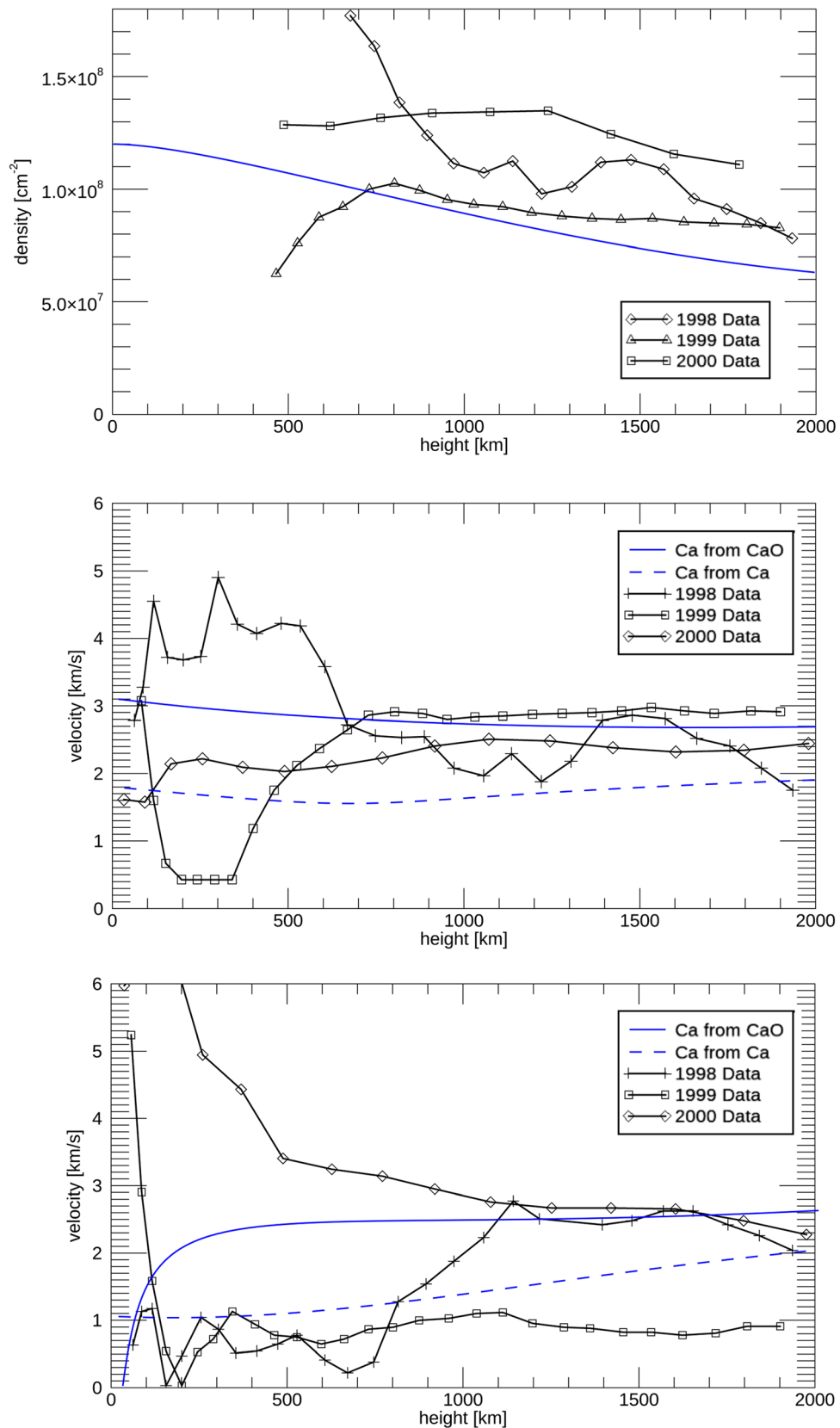
**Figure 13.** Comparison for the calculated density, line-of-sight velocity Vxy, and radial velocity Vzw with the observations. Black lines are for the observed data and blue lines for the modeled data. The data for the three observations are from R. M. Killen et al. (2005).

one. The hydrodynamic timescale of impact plumes for the majority of meteoroid impacts is estimated as $10^{-7}$–$10^{-5}$ s (A. A. Berezhnoy & B. A. Klumov 2008).

For most of the modeling of exospheres, it is assumed that the exospheric species resulting from MIV are atoms. For example, V. Mangano et al. (2007) estimated the probability
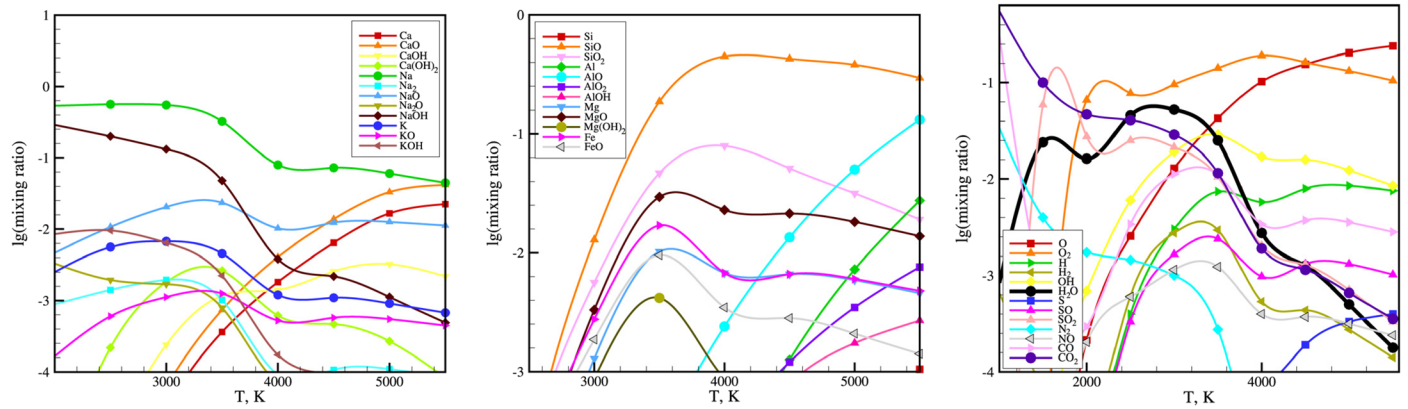
**Figure 14.** Equilibrium fraction of gas-phase species as a function of impact plume cooling for an initial temperature of 10,000 K, an initial pressure of 10,000 bar, and $\gamma = 1.2$. The ratio of matter of planetary (K. A. Goettel 1988) and CI meteorite origin is taken to be 30:1. Left panel: Na-, K-, and Ca-containing species vs. temperature. Middle panel: Si-, Fe-, Mg-, and Al-containing species. Right panel: H-, O-, S-, and N-containing species. Figure adapted from A. A. Berezhnoy & B. A. Klumov (2008), with permission.

that instruments aboard MESSENGER and BepiColombo would detect atoms released via MIV, for which they assumed that MIV produced only metal atoms and not molecular species in the exosphere. However, modeling suggests that micrometeoroid bombardment is also an important source of molecules in the exospheres of Mercury (A. A. Berezhnoy 2018) and the Moon (A. A. Berezhnoy 2010, 2013).

In the initial phase of the impact plume, almost all species will be present in atomic form. With the cooling and expansion of the plume, chemical reactions will take place to form molecules from the species present in the plume. During the early phases of the plume, the density and temperature are high enough for chemical equilibrium, but at a later time and lower temperature, equilibrium is no longer sustained, and finally the chemical reaction will come to a stop. Modeling studies indicate that quenching of the chemical reactions in the plume occurs at about 2500 K and 3 bars (A. A. Berezhnoy & B. A. Klumov 2008). The species present in the expanding plume at that moment, which are metal atoms, metal oxides, and hydroxides, will populate the exosphere.

For Mercury, A. A. Berezhnoy & B. A. Klumov (2008) modeled the evolution of the impact plume by calculating the temperature $T$ and pressure $P$ during expansion, and with this information they calculated the formation and abundance of species considering the set of elements Na, K, Ca, Fe, Al, Si, Mg, Ti, O, H, S, C, and N. At the beginning of the expansion of the impact plume, the chemical composition is in thermodynamical equilibrium because collisions occur frequently and chemical reactions are fast. The equilibrium of the chemical composition of the impact at any moment depends on its temperature and pressure. With the use of quenching theory, the chemical composition of the impact plume can be estimated as it cooled to the point where chemical reactions effectively stopped (A. A. Berezhnoy & B. A. Klumov 2008). The relative fraction of species contributed to the exosphere via MIV depends on the impact velocity, the chemical composition of the surface, the impactor, and the quenching parameters of the chemical composition of the impact-produced plume (A. A. Berezhnoy & B. A. Klumov 2008; A. A. Berezhnoy 2018).

Figure 14 shows the equilibrium fraction of atomic and molecular species in the gas phase as a function of the temperature (A. A. Berezhnoy & B. A. Klumov 2008). During the expansion of the impact plume, it cools, i.e., moving from the high to low temperature in Figure 14 until quenching. The

parameters for quenching define the final chemical composition of species ending up in the exosphere from the MIV event. For example, at quenching, the fractions of Na(atoms)/Na(total) and K(atoms)/K(total) in the impact plume are estimated as 0.7 and 0.4, respectively. The corresponding fractions are much lower for more refractory species, e.g., Mg, Ca, and Al, because these elements form molecules or condense to form solids (in equilibrium MgO, CaO, and $Al_2O_3$, respectively). For temperatures lower than 3500 K, Ca is mainly condensed to the solid state, and the main gas-phase Ca-containing compound is $Ca(OH)_2$. Upon photodissociation, this compound could be the source of the hot Ca observed in Mercury's exosphere (R. M. Killen et al. 2005).

Meteoroid impacts lead to the formation of hot metal atoms with energies of 0.2–0.4 eV (corresponding to temperatures of 2200–4400 K) produced directly during impacts (G. Eichhorn 1976, 1978). Moreover, very hot metal atoms with energies of 1–2 eV (corresponding to 11,000–22,000 K) are predicted to be produced by the subsequent photolysis of oxides and hydroxides in the exosphere of Mercury (A. A. Berezhnoy & B. A. Klumov 2008).

For the MIV release of particles, Table 5 gives the final atomic species in the exosphere, the precursor particles formed in the impact plume, the estimated input fluxes of species to the dayside exosphere of Mercury from the modeling of the impact plume evolution, and the photoionization at Mercury. Condensation of dust grains in the impact plume can significantly reduce the concentrations of impact-produced atoms in the exosphere. Based on modeling, Na, K, and Fe atoms are delivered to the exosphere directly by MIV while Ca, Al, Mg, Si, and Ti atoms are produced by photodissociation of their oxides and hydroxides (A. A. Berezhnoy & B. A. Klumov 2008).

Recently, M. Moroni et al. (2023) performed exosphere Monte Carlo calculations in 3D to simulate the spatial distribution of the Ca-bearing molecule and atomic Ca exospheres resulting from the MIV process. They showed that the observed Ca density at Mercury for one Mercury year (M. H. Burger et al. 2014) can be quantitatively explained by MIV only if the quenching temperature is below 3750 K, so that the CaO in the exosphere is the end product of a photolysis process starting with $Ca(OH)_2$, the dominant compound, followed by Ca(OH), and finally CaO (see Table 5). For the case of a quenching temperature >3750 K, resulting in direct

**Table 5**
Summary of Behavior of the Main Elements During Meteoroid Bombardment of Mercury (A. A. Berezhnoy & B. A. Klumov 2008) Using K. A. Goettel (1988) for Mercury's Composition

| Element | Main Compounds Delivered to the Exosphere via MIV | | Main Mechanisms of Delivery of Atoms to the Dayside Exosphere MIV | Dayside Concentration of MIV-produced Atoms, cm$^{-2}$ | |
| --- | --- | --- | --- | --- | --- |
| | Without Condensation | With Condensation | | Without Condensation | With Condensation |
| Na | Na | Na, NaOH, NaO | Directly by impacts, photodissociation | $4 \times 10^6$ | $4 \times 10^8$ |
| K | K | KOH, K, KO | Directly by impacts, photodissociation | $6 \times 10^4$ | $6 \times 10^6$ |
| Ca | CaO | Ca(OH)$_2$, CaOH, CaO | Photodissociation | $7 \times 10^6$ (reference) | $7 \times 10^6$ (reference) |
| Al | Al$_2$O$_3$ | AlO, AlOH, Al(OH)$_2$ | Photodissociation | $6 \times 10^6$ | $2 \times 10^5$ |
| Fe | FeO, Fe | Fe, FeO, Fe(OH)$_2$ | Directly by impacts, photodissociation | $5 \times 10^5$ | $3 \times 10^7$ |
| Mg | MgO, Mg | MgO, Mg(OH)$_2$, Mg, MgOH | Photodissociation | $2 \times 10^6$ | $8 \times 10^7$ |
| Si | SiO$_2$, SiO | SiO$_2$, SiO | Photodissociation | $2 \times 10^7$ | $2 \times 10^8$ |
| Ti | TiO$_2$ | TiO$_2$ | Photodissociation | $4 \times 10^2$ | $4 \times 10^4$ |
| O | SiO$_2$, SiO | NaOH, O$_2$ | Photodissociation | $2 \times 10^8$ | $6 \times 10^8$ |
| H | CaOH, Ca(OH)$_2$ | NaOH, H$_2$O | Photodissociation | $2 \times 10^6$ | $2 \times 10^8$ |
| S | SO$_2$ | SO$_2$, SO | Photodissociation | $3 \times 10^6$ | $8 \times 10^6$ |
| N | NO, N$_2$ | N$_2$, NO | Photodissociation | $4 \times 10^3$ | $4 \times 10^5$ |
| C | CO$_2$ | CO$_2$, CO | Photodissociation | $10^5$ | $10^7$ |

**Note.** The Ca column density was taken as a reference to avoid estimation of the mass flux of meteoroids onto Mercury.

release of CaO, quantitative agreement with the observations (M. H. Burger et al. 2014) is not achieved.

### 3.2.2. Observations of Molecules and Clusters Released via MIV

The possible presence of molecular species has been inferred from observations several times, though direct detections have not been made so far. M. H. Burger et al. (2012) interpreted the first Ca observations with the UVVS instrument on MESSENGER by modeling the release of Ca from the surface by a thermal process. Observations have shown that Ca is emitted from the surface with high characteristic energies, which was interpreted by the observers as high temperatures of several 10,000 K (T. A. Bida et al. 2000; R. M. Killen et al. 2005, 2009). M. H. Burger et al. (2012) concluded that the origin of this high-energy, asymmetric Ca source is unknown, but best modeled with a thermal source on the surface at a temperature of 50,000 K. From their limited data set, they concluded that the observations were not consistent with MIV, ion sputtering, ESD, or vaporization at dawn of material trapped on the cold nightside, and that substantial molecular Ca production in impact plumes did not contribute to the observations.

Subsequently, M. H. Burger et al. (2014) modeled a larger set of Ca observations recorded with the UVVS instrument on MESSENGER being the result of MIV. They observed very high temperatures of the Ca atoms mean $(6 \pm 1) \cdot 10^4$ K, which cannot be the direct result of meteoritic impact release of Ca atoms, which would be about 4000 K (see above, and the review by P. Wurz et al. 2022). M. H. Burger et al. (2014) argue that the high energy might result from the CaO being released by MIV and dissociated into Ca and O atoms in the exosphere, but they caution that the excess energies of these species upon dissociation are not well understood (M. H. Burger et al. 2014). Later, exospheric Ca observed by MESSENGER while orbiting Mercury could be explained by the combination of MIV and Mercury moving in and out of the interplanetary dust disk plus a cometary dust stream (R. M. Killen & J. M. Hahn 2015). To explain the energetics, the authors postulated that the observed atomic calcium in Mercury's exosphere is the product of Ca-bearing molecules

that are ejected in the impact plume and subsequently dissociated.

Using observations by MESSENGER, a good correlation between Mg atoms in the exosphere and the Mg abundance in the terrain on the underlying surface was found (A. W. Merkel et al. 2018). This observation supports the interpretation that the majority of the material in the exosphere originates from the planet's surface, which is generally assumed for a surface-bound exosphere. However, observations directly connecting the distribution of exospheric density to variations in the regional surface composition have been lacking. The UVVS measurements of Mg were interpreted as the exospheric Mg being the result of MIV (A. W. Merkel et al. 2017, 2018) and that sputtering is an unimportant contributor at these low latitudes between $\pm 30°$. Sputtering was not considered an important contributor for these measurements performed at low latitudes because of the regularity in the year-to-year variations, the lack of short time variations that are typical for solar wind-related signals, and because of the shielding of the solar wind by Mercury's magnetosphere at low latitudes (P. Wurz et al. 2022), but sputtering could be important at higher latitudes. However, the high characteristic energies (large-scale heights), interpreted as high temperatures of the Mg atoms in the range between 5000 to 10,000 K, cannot be the direct result of meteoritic impact release of the Mg atoms. Using the same argument as above to explain the energetics of the observed Mg atoms, it was postulated that MgO is the initial species released from the surface by MIV and that the additional energy arises from the breakup of MgO into atomic constituents (A. W. Merkel et al. 2017).

Fe, Al, and Mn atoms have also been observed in Mercury's exosphere (see Table 6 for details). If meteoroid bombardment is the release process for these atoms into Mercury's exosphere, the main Fe-, Al-, and Mn-containing species predicted to be released via impacts are Fe, FeO, AlOH, AlO, Al(OH)$_2$, and Mn (A. A. Berezhnoy 2018).

In laboratory experiments, spectroscopic studies of hypervelocity impacts of Cu projectiles on polycrystalline dolomite samples, a calcium magnesium carbonate CaMg(CO$_3$)$_2$, were performed (S. Sugita et al. 2003). The optical spectra showed

**Table 6**
Measured or Modeled Abundances of Species in Mercury's Exosphere

| Species | Surface Abundance ($cm^{-3}$) | Total Zenith Column ($cm^{-2}$) |
|---|---|---|
| H | 23; 230[a] | $3 \times 10^{9h}$ |
| $H_2$ | $< 1.4 \times 10^{7n}$ | $< 2.9 \times 10^{15n}$ |
| He | $6.0 \times 10^{3a}$ | $< 3 \times 10^{11h}$ |
| | $7.3 \times 10^{3o}$ | |
| Li | | $< 8.4 \times 10^{7m}$ |
| | | $< 4 \times 10^{7p}$ |
| O | $4.0 \times 10^{4a}$ | $< 3 \times 10^{11h}$ |
| OH | $1.4 \times 10^{3a,d,e,o}$ | $1 \times 10^{10d,e}$ |
| $H_2O$ | $< 1.5 \times 10^{7n}$ | $< 1 \times 10^{12c}$ |
| | $< 2.7 \times 10^{4o}$ | $< 8 \times 10^{14n}$ |
| $^{20}Ne$ | $6 \times 10^3$ day[c,o] | |
| | $7 \times 10^5$ night[c] | |
| Na | $(1.7–3.8) \times 10^{4a}$ | $2 \times 10^{11i}$ |
| | $3.3 \times 10^{3a}$ | |
| Mg | $7.5 \times 10^{3d}$ | $3.9 \times 10^{10d}$ |
| $N_2$ | $< 2.3 \times 10^{7n}$ | $< 9 \times 10^{14n}$ |
| | $< 5 \times 10^{3o}$ | |
| Al | 654[c] | $3.0 \times 10^{9d}$ |
| | | $(1.9–7.7) \times 10^{9q,r}$ |
| Si | $2.7 \times 10^{3d}$ | $1.2 \times 10^{10d}$ |
| $O_2$ | $< 2.5 \times 10^{7n}$ | $< 9 \times 10^{14n}$ |
| | $< 1.6 \times 10^{5o}$ | |
| S | $5 \times 10^{3d}$ | $2.0 \times 10^{10d}$ |
| | $6 \times 10^{5g}$ | $2.0 \times 10^{13g}$ |
| K | $3.3 \times 10^{2b}$ | $2 \times 10^{9b}$ |
| | $5 \times 10^{2h}$ | |
| | 70[o] | |
| $^{40}Ar$ | $< 6.6 \times 10^{6a}$ | $< 9 \times 10^{14b}$ |
| | $4.4 \times 10^{4o}$ | $1.3 \times 10^{9k}$ |
| Ca | | |
| | 387[d] | $< 1.2 \times 10^{9d}$ |
| | $< 239^f$ | $< 7.4 \times 10^{8c}$ |
| | | $1.1 \times 10^{8j}$ |
| Mn | | $4.9 \times 10^{7r}$ |
| Fe | 340[d] | $7.5 \times 10^{8d}$ |
| | | $8.2 \times 10^{8q}$ |
| $CO_2$ | $< 1.6 \times 10^{7n}$ | $< 4 \times 10^{14n}$ |
| | $< 4 \times 10^{3o}$ | |

**Notes.** Detailed references are given in the footnotes.
[a] D. M. Hunten et al. (1988): hot and cold components.
[b] A. E. Potter & T. H. Morgan (1997): measured abundance.
[c] R. R. Hodges (1974): model abundance.
[d] T. H. Morgan & R. M Killen (1997): assumed model abundances.
[e] T. H. Morgan & R. M Killen (1997): model abundances.
[f] A. L. Sprague et al. (1993): measured upper limit.
[g] A. L. Sprague et al. (1995, 1996): prediction.
[h] D. E. Shemansky (1988): Mariner 10 measurements.
[i] R. M. Killen et al. (1990): measured abundance.
[j] T. A. Bida et al. (2000): measured abundance.
[k] R. M. Killen (2002): model abundance.
[l] R. M. Killen & W.-H. Ip (1999): earlier review.
[m] A. L. Sprague et al. (1996): model abundance.
[n] A. L. Broadfoot et al. (1976): measured abundance.
[o] P. Wurz et al. (2019): model abundance.
[p] A. Doressoundiram et al. (2009): measured abundance.
[q] T. A. Bida & R. M. Killen (2017): measured abundance.
[r] R. J. Vervack et al. (2016): measured abundance.

atomic as well as molecular spectroscopic signatures (mostly CaO) of the species in the impact plume at a temperature of about 6000 K (S. Sugita et al. 2003). Depending on the temperature and pressure in the impact plume, the fraction of diatomic molecules ranged from about 20% to below 1%, and a large fraction of the impact vapor, up to 100%, was ionized (S. Sugita et al. 2003).

### 3.3. Particle Desorption by Photons and Electrons

ESD and PSD are caused by an electronic excitation of an atom or molecule on the surface of a mineral by an electron or photon, respectively, impinging on the surface, which leads to an antibonding state and the eventual release of the atom or molecule from the surface (B. V. Yakshinskiy & T. E. Madey 1999, 2000, 2003). In the surface science community, these processes are referred to as desorption induced by electronic transitions and have been investigated for decades. The theoretical description and observations of ESD and PSD with respect to planetary science were summarized in the review paper by P. Wurz et al. (2022). For the discussion here of Mercury's surface composition and atmospheric release processes, the most relevant aspect is that ESD and PSD are mostly relevant for the release of the volatile species Na, K, and S. For other species, desorption is negligible compared with sputtering and MIV (P. Wurz et al. 2022). More specifically, "from laboratory experiments we know that PSD only releases atoms or molecules adsorbed on the surface, i.e., species that are not chemically bound within a mineral" (P. Wurz et al. 2022, p. 20).

Ion release has been observed for both ESD and PSD. Laboratory studies with electrons at energies of tens to hundreds of eV, resembling electrons in Mercury's magnetosphere, showed direct ion release of $H^+$, $H_2^+$, $O^+$, $H_3O^+$, $Na^+$, $K^+$, and $O_2^+$ from silicate glasses, with the H- and O-bearing species originating from water that had been chemisorbed on the sample surface (J. L. McLain et al. 2011). In laboratory studies of the PSD at 355 nm of CaS powder samples, the ejection of $Ca^+$ ions was observed with a cross section of $(3.2 \pm 0.9) \times 10^{-24}\,cm^2$ (C. J. Bennet et al. 2016), which is several decades lower than the PSD of neutral Ca.

In laboratory studies of the PSD of CaS, powder samples at 355 nm were used as a proxy for the mineral oldhamite associated with the hollows on Mercury's surface. The measured velocity distributions of ejected Ca atoms can be fit using a combination of two Maxwell–Boltzmann distributions: one has the sample temperature of 600 K, and a hotter one that has a temperature of roughly 1400 K, the suprathermal distribution. The ratio of the two temperature distributions depends on the laser intensity (C. J. Bennet et al. 2016). Some of these measurements are shown in Figure 15, left column. The cross section for Ca atom desorption at 355 nm was measured as $\sigma(Ca^0) = (1.1 \pm 0.7) \times 10^{-20}\,cm^2$.

In laboratory studies of the PSD at 193 nm of MgS powder samples, a mineral suggested to be present on Mercury's surface, the measured velocities of ejected S atoms can be fit using two Maxwell–Boltzmann distributions, one with the sample temperature of 300 K, and a suprathermal one at about 1000 K, with a roughly 2:1 ratio of the two components that appears to be independent of the laser intensity (M. J. Schaible et al. 2020). Some of these measurements are shown in Figure 15, right column. The cross section for S atom desorption at 193 nm was measured as $\sigma(S^0) = 4 \times 10^{-22}\,cm^2$. The S desorption yields scale linearly with photon flux below about $10^{23}$ photons $cm^{-2}\,s^{-1}$, indicating a
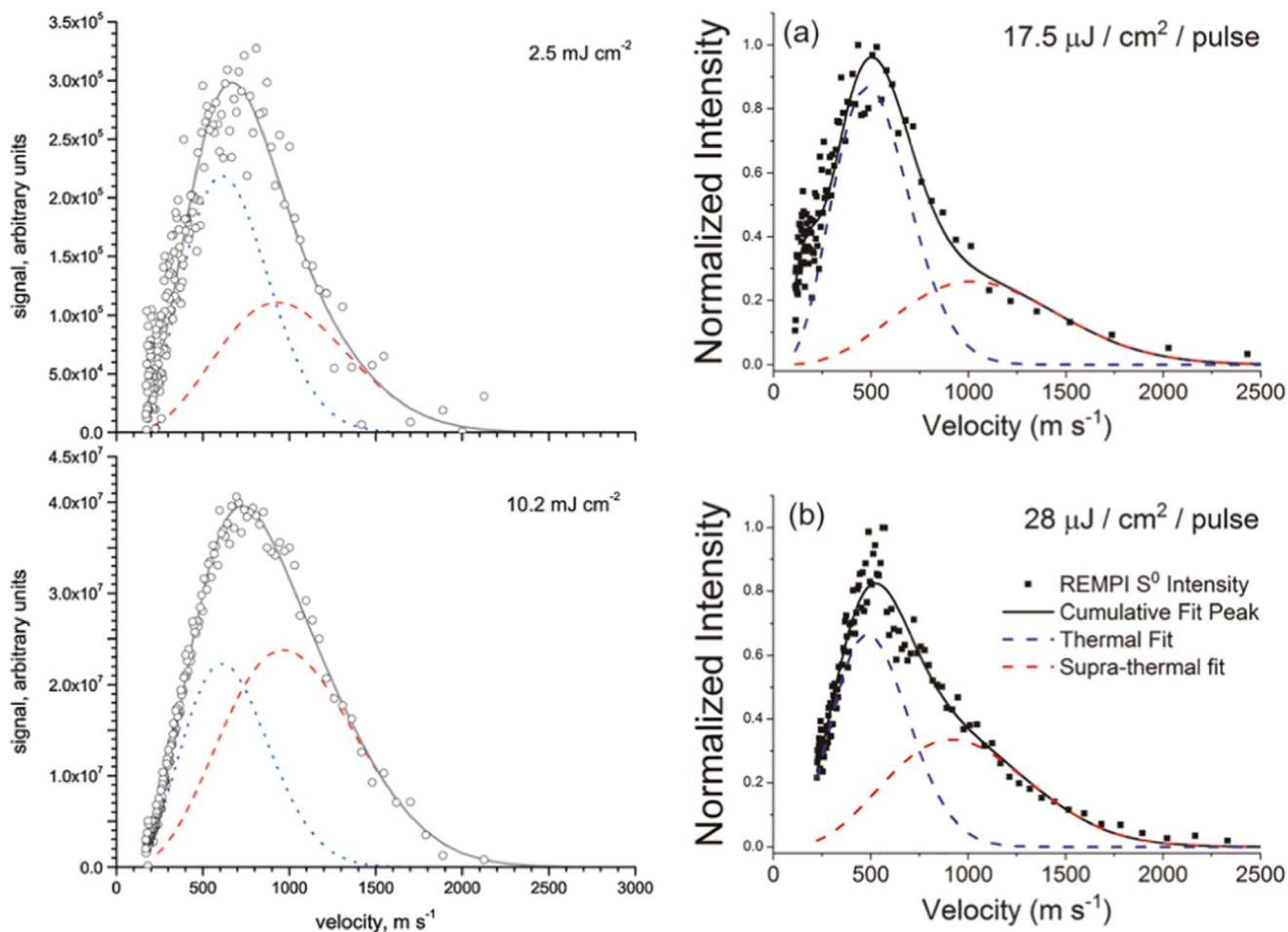
**Figure 15.** Left (from C. J. Bennet et al. 2016, with permission): signal intensity of $Ca^0$ vs. velocity for experiments performed using fluences of (top) 2.5 mJ cm$^{-2}$ and (bottom) 10.2 mJ cm$^{-2}$, respectively (open circles). Also shown are the Maxwell–Boltzmann distributions for the thermal (600 K; blue dotted line) and nonthermal (1389–1494 K; red dashed line) components and the sum of these components (gray line) that were used to fit the observed signal. Right (from M. J. Schaible et al. 2020, with permission): signal intensity of $S^0$ vs. desorption velocity for incident laser powers of (a) 17.5 $\mu$J cm$^{-2}$ and (b) 28 $\mu$J cm$^{-2}$. Also shown are the two Maxwellian velocity distributions used to fit the observed signal: the thermal (300 K; blue dotted line), suprathermal (~1200 K; red dashed line), and the sum of these components (solid black line).

single photon desorption mechanism, as expected for this release process.

M. J. Schaible et al. (2020) measured neutral atom velocity distributions and used them to simulate the trajectories of ejected atoms in a Monte Carlo particle tracing model, and showed that PSD possibly is the primary source of S and Ca in Mercury's exosphere at low (<1000 km) altitudes. Further, they showed that subsequent photoionization of these neutral species in the exosphere, calculated using average UV solar fluxes and tabulated photoionization cross sections, is sufficient to explain the S ion abundances observed by MESSENGER (M. J. Schaible et al. 2020).

Historically, for the velocity distribution of species desorbed via PSD or ESD, usually a Maxwellian or a bi-Maxwellian is assumed. However, D. Gamborino & P. Wurz (2018) showed that a Weibull distribution represents the laboratory data best. Note that the usage of a Weibull distribution has no physical motivation; it just fits the laboratory data best. However, there is no physical justification for using a Maxwellian or even a bi-Maxwellian distribution either, because PSD and ESD are based on electronic excitations and are not thermal processes. Finally, the temperature dependence of PSD measured in the

laboratory turned out to be specific for Na and K. It is unclear how the PSD rates depend on temperature for other species.

The yield of the PSD is not very well known: there are a few laboratory measurements for Na and K, but their dependence on surface temperature is not well constrained, porosity and roughness of the surface (or the grains themselves) may affect the yields, and there might be a dependence on the solar spectrum (see the review by P. Wurz et al. 2022). Even less is known for other species. In addition, most of the models of Mercury's exosphere use a Maxwell–Boltzmann velocity distribution for the released atoms, or a bi-Maxwell–Boltzmann distribution, although neither distribution matches laboratory data (D. Gamborino & P. Wurz 2018). Moreover, there is a competition between sublimation of Na and K (thermal release) and PSD for the release from the surface, since both depend on solar illumination (D. Gamborino et al. 2019). The parameters for thermal release also have their uncertainties, e.g., the heat of sublimation of monolayers, or fractions of a monolayer, of Na or K on the surface of grains and rocks will be different from that of thicker layers. The dissociation process will leave the fragment with some energy. For unimolecular decay, the excess energy is small, but for photodissociation it can be in the range of a few eV. This excess energy to the fragment atoms is an
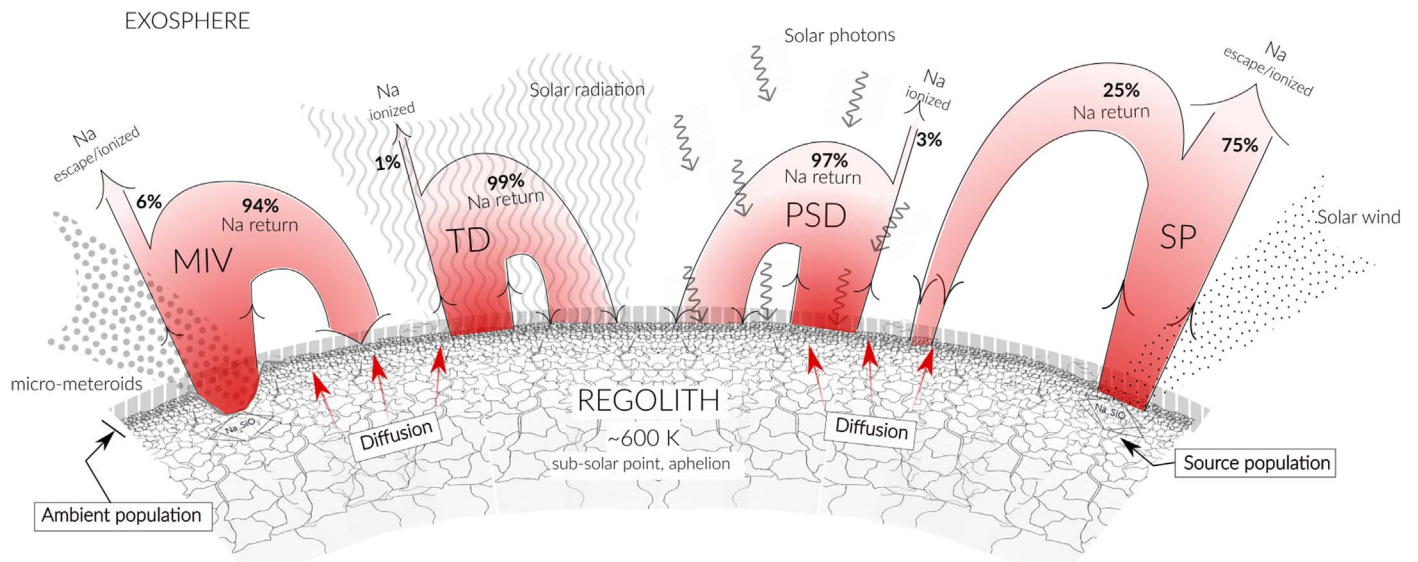
**Figure 16.** Illustration of the different released fluxes of Na due to the different release mechanisms from the mineral compounds in the regolith (the source population) and from the surface (the ambient population). The acronyms of surface release processes are MIV: micrometeoroid impact vaporization; TD: thermal desorption; PSD: photon-stimulated desorption; SP: sputtering. (Figure from D. Gamborino et al. 2019, with permission.)

important parameter, affecting the density profile of these atoms in the exosphere. Unfortunately, this parameter is not well known.

Finally, the composition of the surface remains an uncertainty. The most important input is the elemental composition of the surface since observations in the exosphere are for atoms and their ions. The mineralogy of the surface is an important input parameter, too, because, depending on the release process, the binding of the atoms, or molecule, at the surface or in the mineral is important. Also, the topmost regolith structure (i.e., porosity) is important for trapping and releasing volatiles, like Na and K.

## 4. Exchange of Volatiles Between the Surface and the Exosphere

Volatile species on Mercury's surface and close to its surface are in constant exchange with the exosphere. Mercury, despite its position close to the Sun, is richer in volatiles than previously expected, as found from MESSENGER observations of the surface (L. R. Nittler et al. 2018 and references therein).

For the most studied volatile species, sodium, the processes for release into the exosphere are illustrated in Figure 16. Two surface reservoirs of Na are distinguished (W. H. Smyth & M. L. Marconi 1995; T. H. Morgan & R. M Killen 1997): the ambient population of unbound Na atoms on the surface (the Na atoms adsorbed on the surface) and the source population of Na contained in the minerals. The latter may be liberated from the crystal matrix by space weathering, after which they diffuse through the grains and the regolith to the visible surface (T. H. Morgan & R. M. Killen 1997). The "source atoms" are ionically bonded to the oxygen in a bulk silicate (T. E. Madey et al. 1998) with binding energies larger than 0.5 eV and can only be released directly to the exosphere by high-energy processes such as MIV or sputtering (P. Wurz et al. 2022 and references therein). The released Na atoms that do not escape from Mercury will return to the surface and become ambient particles (B. V. Yakshinskiy & T. E. Madey 1999, 2000, 2004). These ambient particles are thermally accommodated to the

local surface temperature with a binding energy less than 0.5 eV (D. M. Hunten et al. 1988; D. Gamborino et al. 2019). The loss and accretion rates of this ambient population are dominated by low-energy processes such as thermal desorption, PSD, and ESD for all volatile species. PSD and ESD are relevant only for Na and K among all species on Mercury's surface (T. E. Madey et al. 1998; B. V. Yakshinskiy & T. E. Madey 2000; P. Wurz et al. 2022).

### 4.1. Cycling of Na and K Between the Exosphere and the Regolith Surface

Sodium is Mercury's atmospheric species for which we arguably have the most information from observations because Na atoms, together with Ca atoms, exhibit the brightest line emissions in the ultraviolet through visible range of all atmospheric species (Killen et al. 2009), and thus they can be easily observed remotely by ground-based observatories (W. H. Smyth 1986; H. Schleicher et al. 2004; F. Leblanc et al. 2009). However, Na is probably the most complicated atom to understand in the exospheres of Mercury and the Moon, since it is promoted into the exosphere by every known release process (Figure 16) and its ballistic trajectories in the exosphere are modified by solar photon pressure. Therefore, the range of reported Na column densities in the exosphere spans from $<10^{10}\,\mathrm{cm}^{-2}$ to $1.5 \cdot 10^{12}\,\mathrm{cm}^{-2}$ (R. M. Killen et al. 2007). Moreover, even though we know a lot about Na in Mercury's exosphere, we must remember that it is only a minor species in the exosphere, e.g., He is a factor of 1000 more abundant (e.g., P. Wurz et al. 2019).

The spatially inhomogeneous distributed reservoir of atomic Na on the surface forms part of the ambient Na population on the surface (see Figure 16). This reservoir is not chemically bound in the mineral grains, i.e., is not part of Na-bearing minerals, but it is physisorbed in an atomic state on the surface (B. V. Yakshinskiy & T. E. Madey 2000, 2004). The release of the ambient population into the exosphere is dominated by thermal desorption: the layer of Na atoms adsorbed on the surface is depleted and replenished according to surface temperatures (F. Leblanc et al. 2003; D. Gamborino et al. 2019).
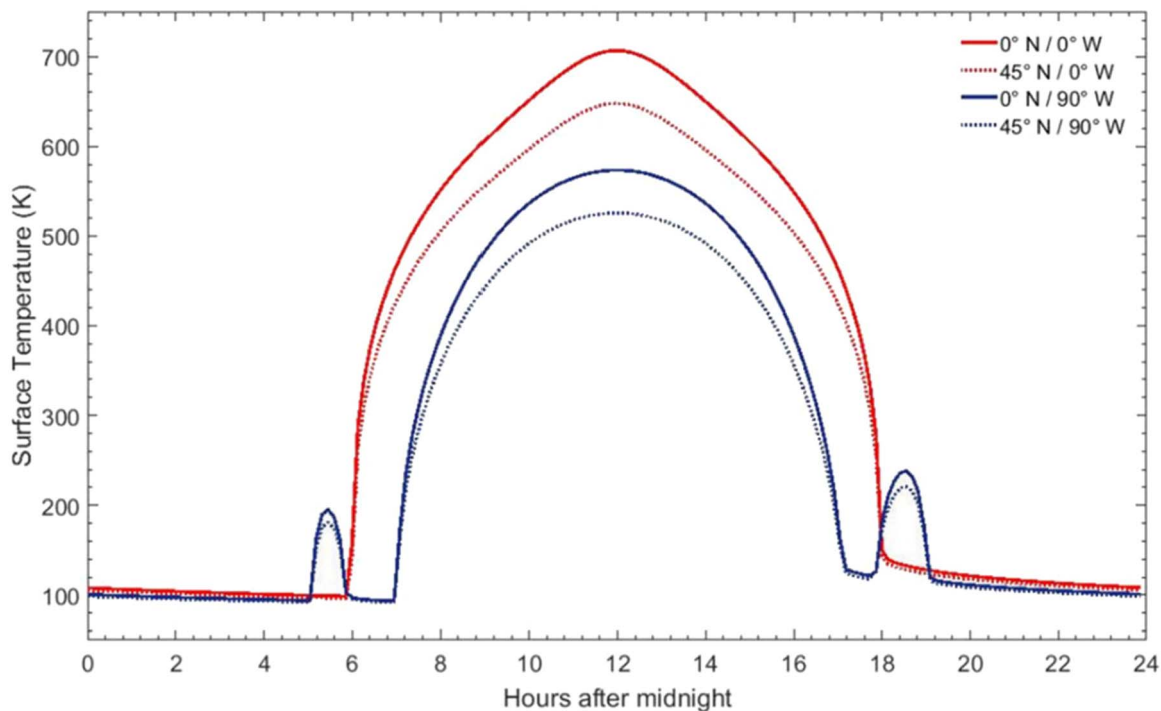
**Figure 17.** Mercury surface temperatures as a function of local time at different latitudes and longitudes. Temperatures at the equator are plotted as solid lines, and at latitudes of 45°N as dotted lines. Red indicates temperatures at 0°W longitude, whereas blue indicates 90°W longitude. During perihelion, Mercury's orbital velocity exceeds its spin rate, which results in a secondary sunrise and sunset at 90° longitude. Figure taken from H. Hiesinger et al. (2020), with permission.

The release of potassium (K) from the surface and its observation in Mercury's exosphere is very similar to Na: K can also be observed by ground-based observatories via scattered sunlight (A. E. Potter & T. H. Morgan 1986). The K abundance in the exosphere correlates reasonably well with the Na abundance (A. E. Potter et al. 2002), indicating the same surface release processes. Details about the Na and K populations in Mercury's and the lunar exosphere are discussed in F. Leblanc et al. (2022). The K radial column density of about $10^9$ cm$^{-2}$ is 2 orders of magnitude lower than the Na column density (A. E. Potter & T. H. Morgan 1997; A. L. Sprague et al. 1990; A. E. Potter et al. 2002) resulting in a high Na/K ratio in the exosphere of 40–140 (R. M. Killen et al. 2007) compared to a Na/K ratio of 20–37 on the surface (see Table 2).

What is the correlation of the elemental and mineralogical composition maps of Mercury's surface (see Section 2) and the volatile reservoirs? The most important correlation is the one between the abundance of the volatiles, e.g., Na and K, on or near the surface (1 m), and the surface temperature; the latter depends on geographic latitude but also, to a minor extent, on the longitude. Figure 17 shows surface temperatures for four selected locations on the surface as a function of local time. The sublimation temperatures for atomic Na and K are 390 K and 335 K, respectively, which is when about $10^{15}$ atoms cm$^{-2}$ s$^{-1}$ are released from a Na- and K-covered surface. The situation is more complicated since the exact physisorbed state of these atoms is unclear, and significant thermal desorption is at somewhat higher temperatures (B. V. Yakshinskiy & T. E. Madey 2004, 2005). However, since the surface temperatures rise to much higher values on the dayside, the resulting released fluxes would be enormous; thus, the thermal release of Na and K is limited by the supply of Na and K to the surface, and not by the sublimation flux, for most of the dayside surface.

Diffusion of alkali atoms in crystalline matter from the interior to the surface is negligible as a source for the near-surface reservoirs compared with diffusion enhanced by defects, cracks, and voids from particle irradiation (cosmic rays and solar energetic particles) and micrometeoroid gardening (A. L. Sprague et al. 1990; P. Wurz et al. 2022). This diffusion, relying on chemical decomposition, crystal defects, and macroscopic cracks, is sometimes called effusion: "Argon easily escapes from a melt, and would become trapped in pockets, from which it could effuse to the surface if cracks open" (R. M. Killen et al. 2002, p. 1228). However, there is annealing of these defects in crystals by high temperatures (Langevin 1997), reducing the effectiveness of this diffusion. Thus, there is a difference in diffusion rates between the Moon and Mercury, because of the lower surface temperatures on the Moon.

High-energy particles produce various types of physical and chemical defects in the surface and thus cause chemical alteration of the surfaces that can free alkali atoms and other volatiles from their chemical bonds within the penetration range of the impacting particles, which is known as chemical sputtering (P. Wurz et al. 2022). The penetration depth is about 30 nm for solar wind protons, 0.1 mm for energetic protons of a few MeV, and about 1 m for galactic cosmic rays with GeV energies (H. Biber et al. 2020; N. Jäggi et al. 2021b; P. Wurz et al. 2022). The liberated alkali atoms will diffuse to the surface and will be released from there to the atmosphere via desorption (thermal, PSD, ESD), in particular at hot regions at low latitudes, and migrate to the colder polar regions by transport via the exosphere. However, the timescale of the diffusion based on crystal defects and macroscopic cracks is difficult to estimate, and diffusion is a strong function of temperature (B. J. Giletti & T. M. Shanahan 1997).

Discrepancies between ground-based observations and MESSENGER measurements of the variability of the sodium
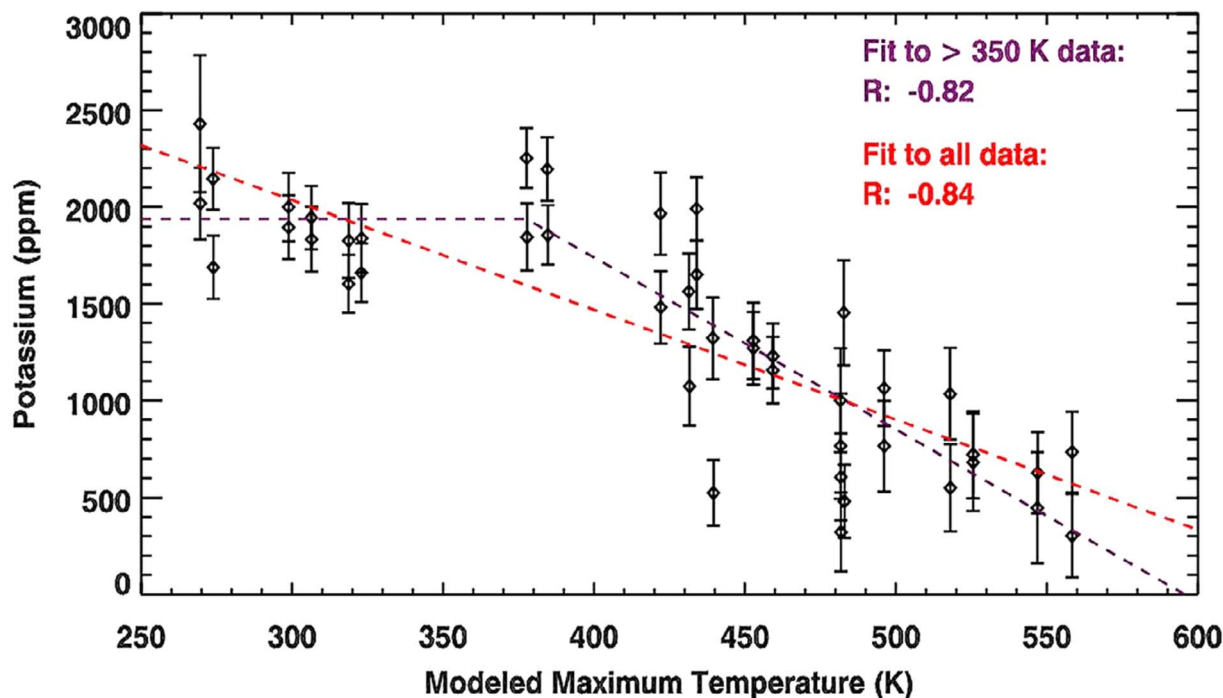
**Figure 18.** K abundances measured by GRS/MESSENGER as a function of the modeled maximum temperature at a depth of 7 cm, including two linear fits for all temperatures (red dashed line) and only for data at temperatures >350 K. Figure taken from P. N. Peplowski et al. (2012a), with permission.

exosphere suggest that current models of the surface–exosphere interaction may be incomplete (M. Sarantos & S. Tsavachidis 2020; F. Leblanc et al. 2022). Using a kinetic model, M. Sarantos & S. Tsavachidis (2020) found that the soil structure of the porous regolith affects the residence time of alkali atoms on the surface and thus the evolution of the alkali reservoir on the surface. For PSD, direct illumination by solar ultraviolet light remains decisive for redesorption of alkali atoms. Kinetic simulations indicate that only grains exceeding 450–500 K release their adsorbed Na atoms from the shadowed parts as the adsorbate mobility increases (M. Sarantos & S. Tsavachidis 2020). The precise threshold temperature for this transition depends on the thermal gradient in the regolith and thus it depends on the structure of the regolith. Consequently, if alkali atoms are adsorbed on a regolith grain between the arrivals of ultraviolet photons, about half of them (and thus half of the alkali exosphere reservoir) remain trapped in the microscopic shadows on the underside of grains and do not contribute to desorption (M. Sarantos & S. Tsavachidis 2020; F. Leblanc et al. 2022).

For the case of potassium, P. N. Peplowski et al. (2012a) found no clear relation between K surface abundance (measured with the GRS on MESSENGER) and large-scale geological terrane types (see Figure 2). On the other hand, the surface abundance of K was found to anticorrelate with the maximum predicted near-surface temperature, either over the full temperature range or above a threshold temperature of roughly 400 K (see Figure 18). The near-surface temperature was taken from a model at 7 cm below the surface, which is compatible with the skin depth of the temperature wave at Mercury, which is of the order of 10 cm (D. Morrison 1969; S. C. Chase Jr. et al. 1976; N. Yan et al. 2006). At larger depths, the temperature is constant at about 400 K, but above it changes from about 100 K on the nightside to about 700 K on

the dayside. The correlation of the K abundance with surface temperature above a threshold of 400 K suggests that condensation of Na and K and sublimation from the shadowed parts of the grains contributes to the release of these alkalis from the top about 10 cm of the regolith layer. Note that the observed threshold temperature (Figure 18) is compatible with the sublimation temperatures of the alkalis. The trapping and thermal release of alkalis in the regolith also suggests that K near the equator and particularly near Mercury's hot poles (P. N. Peplowski et al. 2012a) is being transported via the exosphere and thereby redistributed to cold regions at high latitudes, or is lost to space. An enrichment of K at the warm poles is indeed observed (P. N. Peplowski et al. 2012a). As a consequence of Mercury's 3:2 spin–orbit resonance, the maximum equatorial temperatures are about 130 K higher at the hot poles at longitudes 0°W and 180°W than at the warm poles at longitudes 90°W and 270°W (F. Leblanc et al. 2023). Note that this near-surface layer of about 10 cm is much thicker than the volume probed by XRS and thinner than the volume probed by GRS (see Figure 1). The substantial enrichment for Na and K observed in the northern latitudes can be attributed to the trapping of Na and K in the topmost regolith. The small thermal skin depth means that the surface layer possibly contributing to the K trapping and release correlated with surface temperature is limited.

### 4.2. The Volatile Sulfur

Another important volatile species relevant for the understanding of the interior and surface mineralogy of Mercury is sulfur. It has an average surface abundance of about 2 wt% (see Table 2); previously, a significantly higher sulfur abundance of 4 wt% was reported (L. R. Nittler et al. 2011). Sulfur could be brought from the interior of Mercury to the surface through

volcanic activity in the form of sulfides as slag deposits in Mercury hollows and pyroclastic deposits (see Section 2.1.1). But, contrary to the alkali metals Na and K, S has so far not been directly observed as an atmospheric species. However, the plasma ion measurements from the Fast Imaging Plasma Spectrometer (FIPS) on MESSENGER in the mass range of 32–35 amu were unresolved but were interpreted as containing $S^+$, $O_2^+$, and $H_2S^+$ ions (T. H. Zurbuchen et al. 2008). Modeling of the solar wind sputter release into the exosphere and the subsequent photoionization of exospheric neutral species showed that most of the signal in this mass range can be attributed to $O_2$ and yields an estimated exospheric density of S at the surface of $n_S = 2.76 \cdot 10^5 \, \text{m}^{-3}$ (P. Wurz et al. 2019). This exospheric S would result from sputtering from the surface with an average abundance of S of 0.59 at% in the surface minerals (corresponding to 0.89 wt%; see Figure 2 for a comparison) in the area of the northern polar cap down to about 45° latitude.

Based on laboratory experiments with heated MgS samples, it was suggested that MgS minerals on Mercury's surface could break apart because of high temperature stresses (I. Varatharajan et al. 2019, p. 131): "The most likely explanation for such activity could be that MgS starts to dissociate at high temperatures and therefore releases S to the atmosphere. This dissociation physically changes the surface morphology of the sulfide samples. This observation therefore suggests that thicker deposits of MgS on Mercury's surface might display thermally fractured floors." The search for thermally fractured floors in the hollows and other features in the high spatial resolution images of BepiColombo will open new possibilities in understanding the role of volatiles in surface mineralogy and morphology (see Figure 6 in J. Helbert et al. 2013). Note that MgS used in these experiments may not represent the exact mineralogical makeup of Mercury's surface, but sulfides such as MgS, CaS, and FeS are thought to be representative of the prominent sulfide component of the crust (A. L. Sprague et al. 1995; B. A. Anzures et al. 2020).

Sulfur was found on Mercury's surface on all terrain types (see Figure 2 and S. Z. Weider et al. 2012). Since there is generally good agreement in the average values for those element ratios measured by the XRS and GRS instruments (see Table 1), including the S/Si ratio, these results suggest that Mercury's surface composition is similar at depths of micrometers and tens of centimeters (see Figure 1); thus, most of the observed sulfur is not a superficial surface layer but is present over these depths. There is wide consensus that sulfur is present in the form of sulfides.

We discussed sulfides in detail in connection with hollows in Section 2.2.4. Hollows are found ubiquitously across Mercury's surface (R. J. Thomas et al. 2014), and their formation is probably an ongoing process today, given their young age. Volatile S may be related to the formation of the hollows. It was conjectured that, during the hollows formation, substantial amounts of S were released from these areas into the exosphere, with the S resulting from thermal decomposition of sulfides (J. Helbert et al. 2013). Elemental sulfur and its allotropes are very volatile at Hermean surface temperatures (J. R. Lyons 2008), e.g., $S_2$ has a sublimation temperature of about 390 K. Thus, sulfur will be distributed globally via exospheric transport, and enrichment in sulfur in colder high-latitude regions should result. However, a significant enrichment in sulfur at the poles has not been observed so far; only a

possible S enrichment might be in the HMR (see Figure 2 and Table 2). Since sulfur reacts with nearly all other elements, with the exception of noble gases, it will chemically react when it lands after its exospheric trajectory, forming sulfides on the surface, and further migration of sulfur is thus stopped.

### 4.3. Highly Volatile Gases in Mercury's Exosphere

In contrast to alkali metals or sulfur, the volatiles we are discussing here are, or can be, thermally released already at daytime temperatures on the Moon and Mercury; some do not even condense on the nightside, and some do not even condense in the PSRs. Thus, these volatile species are extremely mobile in Mercury's surface–exosphere system. Many volatile species hardly interact chemically with the surface, such as noble gases, or, for example, $N_2$ and $CO_2$; thus, they reside in the exosphere for a long time until they are lost through photoionization.

For the volatile species Ne, Ar, Xe, $H_2$, O, C, $CO_2$, CO, and $H_2O$, there were only upper limits derived from the Mariner 10 observations (S. Kumar 1976). For Ne and $H_2$, a solar wind origin was assumed, with the latter formed from implanted protons in the regolith (O. J. Tucker et al. 2019). Predictions show daytime surface densities in the exosphere for Ne of $6000 \, \text{cm}^{-3}$ and for $H_2$ of $1.5 \cdot 10^5 \, \text{cm}^{-3}$, respectively, with nighttime enhancements by almost a factor 100 (R. R. Hodges 1974). The presumed Ar detection by Mariner 10 was inconclusive (R. M. Killen 2002), yielding only upper limits on column densities.

There are several volatile gases postulated to exist in Mercury's exosphere, although only upper limits for them have been derived from measurements or modeling thus far (e.g., R. M. Killen & W.-H. Ip 1999; A. Milillo et al. 2005; D. L. Domingue et al. 2007). By analyzing the plasma ion measurements from FIPS on MESSENGER for the complete mass range of 4–45 amu, upper limits for several volatile species in Mercury's exosphere were derived for the MESSENGER flyby III (P. Wurz et al. 2019), which were significantly lower than earlier estimates (R. M. Killen & W.-H. Ip 1999). A list of species that have been observed in Mercury's exosphere, or are inferred to be there, is given in Table 6, which is an update to earlier compilations (R. M. Killen & W.-H. Ip 1999; A. Milillo et al. 2005).

The origin of these volatile species in Mercury's exosphere is varied; possible sources include solar wind capture in the regolith grains (e.g., noble gases) and its processing (e.g., $H_2$ and $H_2O$ formation), diffusion from the interior to the surface (e.g., $^{40}$Ar), release from the surface (thermal, sputtering, PSD, ESD, MIV), and infall of comets and meteoroids. Diffusion from the interior to the surface and release into the exosphere has been discussed in detail for noble gases, in particular for radiogenic $^{40}$Ar, and effusion through the loose regolith can enhance the escape rate (R. M. Killen et al. 2002). Although some of the volatile species do not interact with the surface, neither do they freeze out permanently; they do not form a permanent exosphere because of losses due to atmospheric escape and ionization.

The formation of $H_2$ in the regolith from implanted solar wind was modeled by O. J. Tucker et al. (2019). The global content of $H_2$ in the exosphere results from the incoming solar wind protons, the diffusion and formation of $H_2$ in the regolith grains at the surface, and the subsequent thermal release into the exosphere. The lifetime of $H_2$ in the exosphere is limited by

thermal (Jeans) escape and photoionization. The photoionization lifetime of $H_2$ is about $10^6$ s at Mercury, which is significantly longer than its typical ballistic flight time, which is in the range of $(1-3) \cdot 10^4$ s for perihelion and aphelion, respectively. For thermal escape, a fraction of about 0.05 to 0.1 of the released $H_2$ escapes, compared to 0.006 to 0.01 for the photoionization loss; thus, Jeans escape dominates the $H_2$ loss. Because the time for thermal escape of $H_2$ from the surface is short (hundreds of seconds for subsolar temperatures) compared to the time in the exosphere of the Moon and Mercury, the global distribution of $H_2$ is expected to vary directly with changes in the incident proton flux (C. Grava et al. 2021).

For the Moon, it was suggested a long time ago that water and other hydrocarbons could be formed from implanted solar wind protons via protolysis reactions in lunar grains (E. Zeller et al. 1970). E. J. Gibson Jr. & G. Moore (1972) experimentally demonstrated the formation of water using terrestrial olivine as a lunar analog material. The nanophase metallic Fe of the regolith grains (C. M. Pieters & S. K. Noble 2016) reacts with implanted solar wind protons, and the following reactions result in the formation of hydroxyl and water:

$$Fe = O + H \rightarrow Fe-OH$$
$$2Fe-OH \rightarrow Fe = O + Fe + H_2O$$
$$2Fe-OH \rightarrow Fe-O-Fe + H_2O. \tag{4}$$
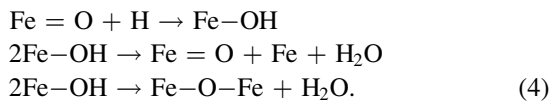
This process involving metal oxides (e.g., $SiO_2$, $TiO_2$, and $Al_2O_3$) was used in modeling the hydroxyl and water production in the lunar regolith by solar wind impact (B. M. Jones et al. 2018). In laboratory studies of irradiating amorphous $SiO_2$ and olivine by protons, the mechanisms and rate of OH bond formation due to proton implantation was derived (M. J. Schaible & R. A. Baragiola 2014). The authors found that the initial conversion rate of implanted protons into hydroxyl species was about 90% of the proton flux, and decreased exponentially with proton fluence.

Spectroscopic observations of the lunar surface were conducted by the Moon Mineral Mapper onboard Chandrayaan-1 ($M^3$) in the wavelength range of 0.43 to 3 $\mu$m, which partly covered the OH/$H_2O$ absorption band (2.7–3.3 $\mu$m). These measurements showed unequivocally that hydroxyl and/or water (in the form of hydrated minerals and/or ice) exist in the lunar regolith at higher latitudes (C. M. Pieters et al. 2009). Similar features were found in the Cassini infrared spectra of the Moon (R. N. Clark 2009), which show a broad absorption at 3 $\mu$m due to adsorbed water and near 2.8 $\mu$m attributed to hydroxyl in the sunlit surface on the Moon. Deep Impact (J. M. Sunshine et al. 2009) observed water ice absorptions at wavelengths of 1.5 and 2.0 $\mu$m on the surface of comet 9 P/Tempel 1. The discovery of widespread distribution of hydroxyl and water on the lunar dayside by different instruments has intensified the debate about the importance of the solar wind in the formation of lunar—and, by analogy, Hermean—water through reactions between solar wind protons with surface minerals (N. Schörghofer et al. 2021).

Transport between the upper regolith layers and the surface can be understood as diffusion and has been discussed above for the example Na. Na atoms that were released into the exosphere and are returning to the surface (see Figure 16 for return fractions) might be effectively trapped in the upper 10 cm of the regolith (M. Sarantos & S. Tsavachidis 2020).

This process might be similar for S, once S is released into the exosphere and returns to the surface.

The only noble gas species detected so far in Mercury's atmosphere is helium (A. L. Broadfoot et al. 1976; D. L. Domingue et al. 2007; R. M. Killen et al. 2007). An obvious source for this helium is implanted solar wind (R. R. Hodges 1974). Probably, the He present on the surface and in the exosphere is dominated by the solar wind source. The solar wind ion flux reaching Mercury's polar cusps is in the order of several $10^8$ to several $10^9$ atoms $cm^{-2}$ $s^{-1}$ depending on solar wind conditions (R. M. Winslow et al. 2012, 2017). Thus, the flux of He deposited to the cusp regions, averaged over one solar cycle, is roughly $3 \cdot 10^{11}$ $m^{-2}$ $s^{-1}$ He atoms, assuming a 5% He abundance in the solar wind. This implies that, already after 100 yr, or nine solar cycles, the solar wind He abundance in the uppermost nanometers of the soil reaches its steady state, as observed in He irradiation experiments (H. Biber et al. 2020). Under typical conditions, the solar wind plasma reaches the surface only at high latitudes; however, the mobility of the regolith grains on the surface (E. S. Costello et al. 2018, 2020) will over time result in He implantation of all grains on the surface. Moreover, coronal mass ejections, which are very frequent during solar active times, can overcome the protective shield of Mercury's magnetosphere, and the whole dayside will be exposed to that plasma (e.g., E. Kallio & P. Janhunen 2003).

H. Biber et al. (2020) performed irradiation and thermal desorption experiments with pyroxene samples subject to a 4 keV $He^{2+}$ ion source. They found that the pyroxene reached saturation of He implantation at roughly $5 \times 10^{16}$ He atoms $cm^{-2}$ or 1.8 wt% of He (for 3.3 g $cm^{-3}$ density of the grains and a penetration depth of 31 nm for 4 keV He ions in pyroxene). Moreover, whereas the implanted He was stable at room temperature (below 300 K), all the He was released from the pyroxene samples when the experiment temperatures exceeded 500 K. This implies that the freshly implanted solar wind He will not be retained in the regolith grains on Mercury's dayside where temperatures exceed 500 K (see Figure 17), but the He will be released to the exosphere where the He will accumulate until the release from the surface matches the loss in the exosphere, mainly via photoionization.

Argon in Mercury's or the lunar exosphere is important for studying how surface-bounded exospheres are shaped by temporary cold trapping of species on the nightside and their release at dawn. $^{40}Ar$ in planetary atmospheres is a measure of potassium abundance in the planet's interior, since $^{40}Ar$ is a product of the radiogenic decay of $^{40}K$ by electron capture with the subsequent emission of a 1.46 MeV gamma ray. Assuming an $^{40}Ar$ diffusion flux of $2 \cdot 10^3$ atoms $cm^{-2}$ from the interior through a fractal distribution of rock sizes to the surface would give a total column abundance of roughly $10^9$ atoms $cm^{-2}$, taking into account that the lifetime of Ar in Mercury's exosphere is only 3.5 days at perihelion and 8 days at aphelion (R. M. Killen 2002). This is similar to the $^{40}Ar$ column abundance in the Moon's exosphere (R. M. Killen et al. 2002). $^{36}Ar$ and $^{38}Ar$ in Mercury's and the lunar exosphere would be of solar wind origin. In the lunar exosphere, $^{36}Ar$ is less abundant by a factor of 15 than $^{40}Ar$, and $^{38}Ar$ is expected to be even lower, indicating that captured solar wind argon is not a large fraction of the atmospheric argon in the lunar exosphere.

## 5. Space Weathering, Its Emulation in the Laboratory, and Its Modeling

The canonical space-weathering processes are radiation of the surface by solar wind ion bombardment and impact modification (melting and gardening) by micrometeorite bombardment (C. J. Bennett et al. 2013; C. M. Pieters & S. K. Noble 2016). Another process, thermomechanical breakdown of rocks and grains, is reviewed in the companion paper (F. Leblanc et al. 2023); thus, this section focuses on the first two processes.

### 5.1. Space Weathering by Impact Gardening

Impact gardening is the process by which meteoritic impacts fracture and stir the outermost crusts of planetary objects with no atmospheres. The formation of regolith on the surface is a direct consequence of these impacts; primarily, it is the result of mechanical weathering. Continued meteoric impacts and bombardment by solar and interstellar charged atomic particles of the unprotected surface over billions of years ground the rock, the regolith of the Mercury, into the progressively finer and fine material. Based on Lunar Reconnaissance Orbiter satellite data of impact ejecta coverage, the top centimeter of the lunar surface is overturned every 80,000 yr (E. J. Speyerer et al. 2016). Particle bombardment and impacts produce amorphous rims on particles, and submicron and nanoscale particles (e.g., B. Hapke 2001; S. K. Noble et al. 2007; D. L. Domingue et al. 2014). Two types of submicroscopic particles have been distinguished: nanophase particles that are <40 nm in size, and larger particles that are >40 nm in size, sometimes referred to as microphase particles (D. T. Britt & C. M. Pieters 1994; S. K. Noble et al. 2007; P. G. Lucey & M. A. Riner 2011; D. T. Blewett et al. 2021). In lunar samples, the nanophase particles occur within the glassy rims that surround grains and agglutinates, and microphase particles occur only within agglutinates (L. P. Keller & D. S. McKay 1997). On the Moon and asteroids, these submicron, nanoscale particles are predominately Fe or FeS. It is unclear, for Mercury's iron-poor surface, what the composition of these particles would be; submicroscopic graphite and troilite are potential candidates (D. Trang et al. 2017).

Aside from space-weathering effects by particle impact, there is also an explicit correlation between particle size and changes in the infrared spectra, as shown in laboratory studies (e.g., B. Udvardi et al. 2017). The authors show that grain size is affecting the intensity and area of infrared bands and band positions. Laboratory studies indicate that the infrared intensity is largest for particle sizes of 2–4 $\mu$m, where for smaller particles the intensity decreases due to the penetration depth of light at infrared wavelengths (B. Udvardi et al. 2017). Laboratory studies in the mid-infrared spectral region in support of the MERTIS instrument on representative minerals (anorthite, enstatite, orthoclase, diopside, labradorite, olivine) showed the degradation of spectral features with a smaller grain size (A. Sprague et al. 2007). Nevertheless, the position and contrast of diagnostic spectral features (CF, RB, and TF) can be used for studying the mineralogy even at grains sizes of <25 $\mu$m (A. Sprague et al. 2007). From laboratory studies, it is known that grain sizes of about 15–30 $\mu$m fit with the observed spectra (J. Warell & D. T. Blewett 2004). For nanoscale (<40 nm) particles, the albedo significantly decreases across the visible and near-infrared range, and the spectral slope changes (redder in the visible to near-infrared, bluer in the ultraviolet to visible; S. K. Noble et al. 2007; P. G. Lucey & S. K. Noble 2008; A. R. Hendrix et al. 2016). For submicron (>40 nm) particles, the reflection and band depths decrease, but no spectral slope changes are observed in either the visible to near-infrared or ultraviolet to visible (S. K. Noble et al. 2007; D. T. Blewett et al. 2021). No studies have been performed in the mid-infrared to examine the effects of submicron, nanoscale particles and their size-dependent spectral effects. However, there have been other studies that show that the spectral effects caused by the material produced by the space-weathering processes can be mimicked by the spectral changes caused by temperature (A. Maturilli et al. 2014) and/or mineral mixing (e.g., G. Serventi et al. 2013; E. Bruschini et al. 2022; F. Leblanc et al. 2023). In addition, because of intense space weathering by meteoritic impacts, a large fraction of agglutinates is expected in Mercury's regolith (M. J. Cintala 1992; Y. Langevin 1997), which have darker, redder, and weaker absorption bands than the corresponding nonagglutinate soil spectra (C. N. Yasanayake et al. 2024).

Space-weathering effects on spectral properties have been modeled using radiative transfer equations (P. G. Lucey & M. A. Riner 2011; D. Trang et al. 2017) to determine submicron, nanoscale particle sizes and abundances. The spectral modeling work of D. Trang et al. (2017) of Mercury's surface examined the presence and distribution of both submicroscopic iron and submicroscopic carbon. Modeling studies found abundances of submicroscopic iron at 3.5 wt% (P. G. Lucey & M. A. Riner 2011) and at 2.5 wt% (D. Trang et al. 2017) above the estimated 1.5 wt% iron abundance from the MESSENGER XRS and GRS (S. Z. Weider et al. 2014, 2015). This may be due to assumptions in the models, temperature effects on spectral properties not accounted for in the models, and the mineral mixtures included in the modeling.

On Mercury, the iron-poor surface coupled with the effects of space weathering served to remove any diagnostic absorption features in the spectral range covered by MASCS to identify and map mineral composition (McClintock et al. 2008; D. T. Blewett et al. 2009; G. M. Holsclaw et al. 2010; M. A. Riner et al. 2010; D. L. Domingue et al. 2014; N. R. Izenberg et al. 2014; K. R. Stockstill-Cahill et al. 2017). Because of the absence of spectral features of silicates in the MASCS observations, no mineralogical mapping of Mercury's surface was possible.

### 5.2. Particle Release by Sputtering

Plagioclases and pyroxenes are the major rock-forming minerals of interest for Mercury. Together with olivine and sulfides (Section 2.2), they are a natural choice as analog material for laboratory investigations of sputtering related to Mercury. Experimental data of sputter yields from minerals relevant to Mercury's surface have been scarce for a long time. Since 2014, several laboratory studies with minerals have been presented, including the pyroxenes enstatite (H. Biber et al. 2022, 2020), wollastonite (P. S. Szabo et al. 2018), and the Ca end-member of plagioclase, anorthite (H. Hijazi et al. 2014, 2017).

The state-of-the-art procedure to obtain sputter yields is by using a quartz crystal microbalance (QCM). This technique is a precise method to measure the absolute mass loss of a sample during sputtering in real time and in situ by using oscillation changes of a quartz resonator. Making use of the piezoelectric properties of quartz, an oscillation is driven in the quartz crystal, whose resonance frequency is monitored. For small mass changes compared to the initial quartz mass, there exists a
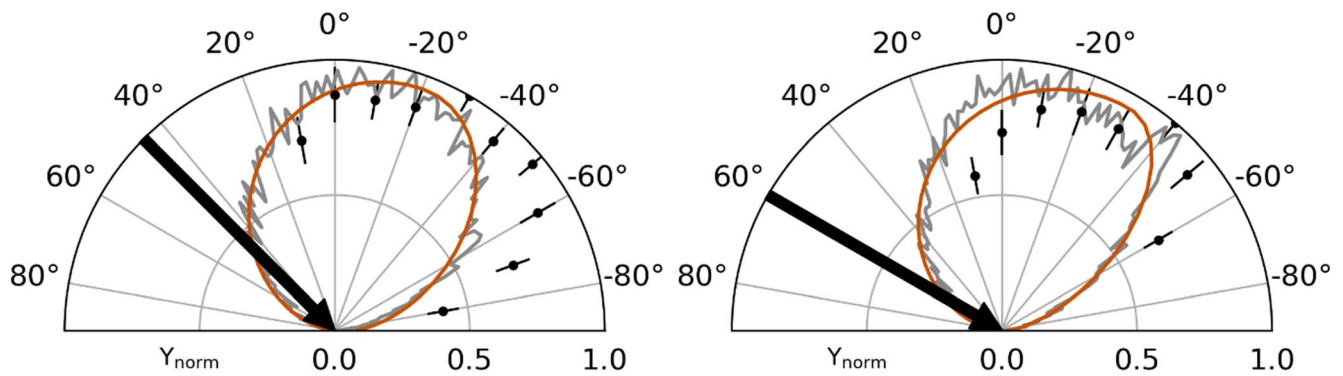
## He → Enstatite (MgSiO₃)



**Figure 19.** Normalized polar distribution of sputtered ejecta generated by 4 keV He$^+$ ions impinging at 45° and 60° on enstatite. The experimental data (black) with 1 standard deviation error bars are from H. Biber et al. (2022), along with modeling results from SDTrimSP (gray) and fit results (orange) based on the model presented in N. Jäggi et al. (2023).

linear relation between the resonator mass and its resonance frequency (G. Sauerbrey 1959). This is still valid for thin layers of material deposited onto the QCM, making the technique applicable for studying the sputtering properties of regolith analogs (as films on a QCM) under ion bombardment. In an extension of this setup, a second QCM is placed facing the irradiated sample to catch the ejecta. By varying the location of the catcher QCM, the angular distribution of sputtered particles can be determined. Furthermore, using a catcher QCM enables experiments with specimens in forms and shapes that cannot be deposited on the primary QCM, such as pressed mineral pellets (C. Cupak et al. 2021; H. Biber et al. 2022, 2021).

The solar wind ions that hit Mercury are composed mostly of H$^+$ (95%–98%) and He$^{2+}$ (2%–5%) (R. A. Aellig et al. 2001; P. Wurz 2005). Modern work on the determination of sputter yields for H$^+$ and He$^{2+}$ started out on thin films (H. Hijazi et al. 2014, 2017; P. S. Szabo et al. 2020a), followed by irradiation experiments on pressed pellets of lunar and Hermean analog materials to realize more realistic surface properties in the sputter experiments (N. Jäggi et al. 2021b; H. Biber et al. 2022). The small sputter yield of H$^+$ ions is often challenging in experiments, especially when only sputtered particles are measured in a pellet-and-catcher setup where mass changes are smaller than those observed directly on a thin-film QCM sample. To obtain a large enough removal of material by sputtering, and thus a large enough change in the quartz oscillation frequency in the QCM detectors, high ion fluxes are required, which might lead to undesirable side effects, e.g., excessive H implantation (M. J. Schaible & R. A. Baragiola 2014).

In the solar wind, there are also traces of heavier, multiply charged ions such as C$^{q+}$ ($q = 4$–6) and O$^{q+}$ ($q = 6$–8), each at an abundance of a few $10^{-4}$ in the solar wind plasma, and heavier ions at even lower abundance (R. von Steiger et al. 2000; P. Wurz 2005). Multiply charged ions have a potential energy that is known to increase the sputter yield in a process called potential sputtering (F. Aumayr & H. Winter 2004). The process has so far not been decisively quantified nor understood for minerals, and only a few data sets exist, notably for He$^{2+}$ and Ar $^{q+}$ ($q = 1$–8) on wollastonite (P. S. Szabo et al. 2018, 2020a) for He$^+$, O$^+$, and Ar$^+$ on augite and wollastonite (P. S. Szabo et al. 2020b), and for He$^{2+}$ and Ar $^{q+}$ ($q = 1$–9) on anorthite (H. Hijazi et al. 2014, 2017).

Sulfide-bearing minerals that are potentially relevant for Mercury (Section 2.2), such as niningerite (MgS) and oldhamite (CaS), bear additional complications in experiments, as discussed in Section 4.2. They have been found to not only release particles by sputtering, but also through damage-driven diffusion, as observed in troilite (FeS; J. M. Christoph et al. 2022). This leads to fast depletion of surface sulfur and is expected to also be relevant for Mercury, but experiments are needed.

Most sputter yields that we present here are limited to the measurement of the amount of mass that is ejected, without differentiating between the different species sputtered. To better understand the ion–surface interaction, information about the properties of the released particles is needed. Depending on a wide range of system parameters, vast differences in energy and angular distributions of emitted particles occur (H. Oechsner 1975; H. H. Andersen et al. 1985; G. Betz & K. Wien 1994). A detailed understanding of the energy and angular distributions is, however, crucial for correctly describing the particles' trajectories in the exosphere of Mercury (P. Wurz et al. 2022). The setup with the QCM as a catcher also allows one to probe the angular distribution of sputtered particles in the polar direction. The first angular distribution data for the mineral enstatite (MgSiO₃) have been reported (H. Biber et al. 2022) and are shown in Figure 19. A new setup to measure absolute sputter yields as a function of the polar and azimuth angles simultaneously has been designed (C. Bu et al. 2024). First measurements have been presented for sputtering of Cu surfaces with 20 keV Kr$^+$ ions for a total fluence of about $1 \cdot 10^{18}$ ions cm$^{-2}$. Comparisons to Static and Dynamic TRIM Sequential and Parallel (SDTrimSP; A. Mutzke et al. 2019) showed significant differences between the simulation and the measurements, e.g., the observed azimuthal asymmetry was not reproduced in the simulation (C. Bu et al. 2024).

### 5.3. Review of Simulation Methods for Sputtering and Space Weathering

To simulate the sputter process of minerals, Monte Carlo (MC) and molecular dynamics (MD) codes are commonly used. MC codes are based on the binary collision approximation (BCA; W. Eckstein 1991) and provide an acceptable
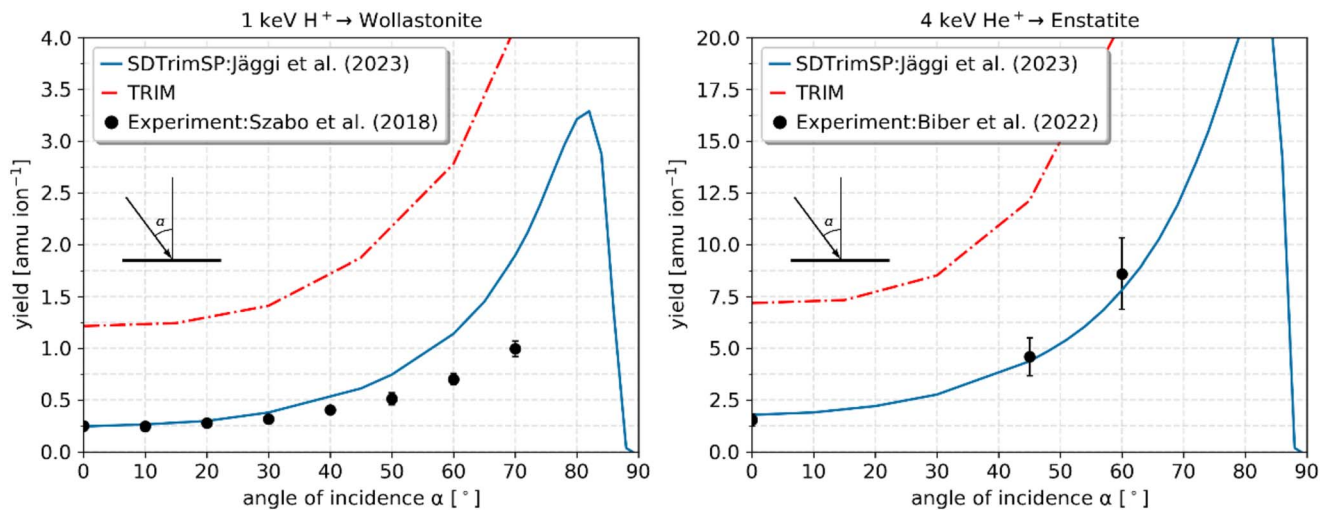
**Figure 20.** Experimental data (black; errors are 1 standard deviation) for $H^+$ on wollastonite, $CaSiO_3$ (P. S. Szabo et al. 2018), and $He^+$ on enstatite (H. Biber et al. 2022) with TRIM results (dashed red line) and the SDTrimSP model data (blue line; N. Jäggi et al. 2023) in comparison.

match to the experimental data regarding the angular and energy distribution of the ejecta while keeping the computational demands low. MD methods consider interatomic forces, which in turn implicate intense computational work and a lesser ease of use due to more parameters necessary to set up the model. A good review of the shortcomings and pitfalls of both MD and BCA models can be found in G. Hobler (2013); however, to produce sufficient data for angular and energy distributions, MC-BCA models are unrivaled when it comes to producing good statistics.

After the development of the first fast MC-BCA model of TRansport of Ions in Matter (TRIM; J. P. Biersack 1980), several more models have been developed, including TRIM.SP (J. P. Biersack & W. Eckstein 1984), MARLOWE (M. T. Robinson 1981), TRIDYN (W. Möller & W. Eckstein 1984; W. Möller et al. 1988), and IMSIL (G. Hobler 1995; S. Lindsey & G. Hobler 2013). We focus here on the still actively developed SDTrimSP code (A. Mutzke et al. 2019). SDTrimSP is an expanded and improved version of the static TRIM.SP and the dynamic TRIDYN and recently received a graphical user interface (P. S. Szabo et al. 2022b).

Sputter yields computed for grazing angles of incidence (angle $>70°$ in Figure 20) are known to often be significantly overestimated compared to laboratory data. This is attributed to any amount of surface roughness causing a reduction of the local impact angle together with processes such as redeposition or shadowing actively preventing material from leaving the surface (U. von Toussaint et al. 2017; R. Arredondo et al. 2019; R. Stadlmayr et al. 2020; P. S. Szabo et al. 2022a). Material properties of a regolith such as porosity or surface roughness could be implemented in codes such as SDTrimSP-3D or TRI3DYN to obtain better agreement with the measurements. An alternative approach was used by H. Biber et al. (2022), where data from a flat surface were fed into the ray-tracing code SPRAY (C. Cupak et al. 2021) together with the parameters of the surface roughness to successfully recreate sputter yields from a rough, pressed pellet. At impact angles close to the surface normal, 1D simulations can already reproduce sputter yield data well.

For an in-depth review of SDTrimSP models, best practices, model assumptions, and how well they recreate laboratory data, we refer to L. S. Morrissey et al. (2023) and N. Jäggi et al. (2023).

The work by N. Jäggi et al. (2023) includes a new model, which represents minerals based on chemical compounds to obtain more accurate mineral densities and uses the tabulated data of said compounds to prescribe surface binding energies (SBEs) in the model. Accurate SBEs are critical for reliable sputter yield predictions. L. S. Morrissey et al. (2022) have shown that the SBE for an element in a mineral can differ significantly from the cohesive energy for the mono-elemental solid, which is the default SBE used by currently available MC-BCA models. For example, the MD SBEs for the Na-bearing silicates expected on the surface of Mercury are about 8 times larger than the Na mono-elemental cohesive energy. The resulting sputter yields are about 10 times smaller, and the peak in the energy distribution of the sputtered atoms is 8 times larger. The latter has a significant impact on the predicted fraction of sputtered Na atoms above the escape velocity of Mercury and the resulting shape of the Na exosphere (R. M. Killen et al. 2022).

N. Jäggi et al. (2023) also find that, independent of the SBE and density assumptions, dynamic computations where the sample composition is allowed to change over time resulting from the ion irradiation were found to best recreate the fluence dependence of laboratory sputter yields. The dependency shows a decreasing yield with the increasing number of deposited ions until a steady state is reached in both the laboratory data and the dynamic computation. At this point, the composition of the sputter yield in the model becomes stoichiometric to the initial composition of the irradiated sample. The time required to reach this equilibrium on Mercury is short. Given Mercury's irradiated cusp areas and an average solar wind flux of $10^{11}$ ions $m^{-2}\,s^{-1}$ (J. M. Raines et al. 2022) and the approximate equilibrium fluence of $10^{21}$ ions $m^{-2}$ (e.g., H. Biber et al. 2020), we obtain equilibrium after about 5 and 130 yr for $H^+$ and $He^{2+}$, respectively.

### 5.4. Review of Regolith Porosity and Its Effect on Sputtering

Sputtering by solar wind ions and magnetospheric ions has been identified as a key process to populate Mercury's exosphere (P. Wurz & H. Lammer 2003). Sputtering will in particular contribute refractory elements to the exosphere and produces populations with larger-scale heights than other release mechanisms as the energies of sputtered atoms are

higher than from desorption processes or MIV (P. Wurz et al. 2022). A reliable description of the sputtering from Mercury's surface is thus needed to understand the exosphere formation. Key to this is an understanding of the microscopic makeup of the regolith surface and how regolith properties affect the sputtering process.

Both in experimental and numerical studies, sputter yields have often been investigated only for an ideally flat surface (e.g., H. Hijazi et al. 2014, 2017; P. S. Szabo et al. 2018; H. Biber et al. 2020). However, the porous structure of the regolith strongly affects the sputtering process and cannot be neglected. Analytical calculations by R. Johnson (1989) and MC simulations by T. Cassidy & R. Johnson (2005) discussed several effects that the porous regolith can have on the sputter process. Deviations from the interaction of ions with flat surfaces are largely caused by two phenomena: local angles of ion impact on the surfaces of grains and redeposition of sputtered atoms at other grains. For an angular dependence of the sputter yield $Y(\alpha)$ $\alpha \cos (\alpha)^{-1.6}$ on the incidence angle $\alpha$ and a cosine distribution of sputtered atoms around the surface normal, T. Cassidy & R. Johnson (2005) found a reduction of the total sputter yield to 0.64 of the value for a flat surface. For this case, their model also predicted that 74% of originally sputtered atoms are redeposited onto another grain and are not able to escape the regolith. This is in good agreement with experimentally observed sputter-induced surface concentration changes on powder samples (see M. Loeffler et al. 2009; C. A. Dukes et al. 2011). T. Cassidy & R. Johnson (2005) also found only small changes regarding the angular and energy distributions of the sputtered atoms. Their simulation results did not depend on the chosen grain shape (spherical, ellipsoidal, or cubic) or the porosity. In this context, the authors stated that their assumptions of a Poisson distribution for the distance, until an ion hits a grain, limited their model to very porous structures. Regolith with lower porosity would have properties closer to a flat surface that are not covered by their model.

Few additional studies about the effects of regolith on sputtering exist. Some other porous structures, such as tungsten fuzz (e.g., D. Nishijima et al. 2011; R. Stadlmayr et al. 2020), various foams (e.g., G. Z. Li & R. E. Wirz 2021), and porosity on a nanoscale (e.g., J. F. Rodriguez-Nieva et al. 2011) have been researched. However, in recent years, several advances in sputtering research have been achieved for more conventional rough surfaces. Improved understanding in this area can also be very helpful for describing the sputtering of regolith grains, especially because the importance of local incidence angles and redeposition also holds for rough surfaces. Research on sputtering of rough surfaces has largely been motivated by plasma–wall interaction in nuclear fusion reactors, where ion bombardment from the fusion plasma affects the lifetime of reactor wall elements (see J. W. Brezinsek Coenen et al. 2017). The different theoretical approaches that have been developed to establish a fundamental understanding of the sputtering process of rough surfaces may also be applicable for sputtering from regoliths. M. Küstner et al. (1998, 1999) presented a simulation method based on combining local incidence angles and a numerical redeposition calculation, which led to good agreement with experimental results. Most efforts have focused on developing 3D BCA codes such as TRI3DYN (W. Möller 2014) and SDTrimSP-3D (U. von Toussaint et al. 2017) that represent extensions of TRIDYN and SDTrimSP with a cuboid voxel geometry of the impacted surface. These codes allow the

simulation of ion impacts on rough surfaces as well as more complex nanostructures (e.g., R. Arredondo et al. 2019; R. Stadlmayr et al. 2020). They include, in a consistent manner, roughness-induced effects such as local incidence angles, redeposition of sputtered atoms, secondary sputtering by locally reflected ions, and even dynamic simulations of the changing target morphology (e.g., R. Arredondo et al. 2020; S. Choupanian et al. 2021). Different approaches that have been applied for simulating sputtering of rough surfaces include BCA codes with fractal geometries (e.g., J. Drobny et al. 2017) or ray-tracing codes such as SPRAY (see C. Cupak et al. 2021).

Several studies regarding the sputtering of rough surfaces have focused on finding well-suited characterization parameters for describing the rough surfaces. The rms roughness represents a commonly used parameter, but it does not include any information on surface slopes that play a significant role for sputtering. Instead, the distribution of surface inclination angles $\delta_m$ has sometimes been preferred for being scale independent (e.g., R. Stadlmayr et al. 2018; R. Arredondo et al. 2019). C. Cupak et al. (2021) found that the mean inclination angle $\delta_m$ of this distribution allows for a much better comparison with experimental sputter yields for different surfaces than the rms roughness. Based on these findings, P. S. Szabo et al. (2022a) suggested an analytical theory for sputtering of Gaussian rough surfaces that only uses $\delta_m$ as a characterization parameter. An approximation of a Gaussian surface with the same value $\delta_m$, similar to the B. Hapke (1984) model of reflection from rough surfaces, led to good agreement with several experimental studies.

Regarding the general understanding of how the surface structure changes the sputter behavior, Figure 21 gives an example of modeling results for the total sputter yield $Y$. The modeled dependence of the sputter yield $Y$ on the incidence angle $\alpha$ relative to the bulk surface normal is shown for 2 keV $Ar^+$ ions impacting a tungsten surface. The sputter yield is clearly affected by surface roughness, here described by the mean surface inclination angle $\delta_m$. Figure 21 includes results from analytical theory (P. S. Szabo et al. 2022a) and SPRAY simulations (C. Cupak et al. 2021). Compared to the flat surface with $\delta_m = 0°$, a small roughness generally increases the sputter yield under small incidence angles due to the local incidence angle effect. For very rough surfaces with large $\delta_m$ values, redeposition of sputtered atoms onto the surface dominates and almost completely suppresses the sputtering. The exact shape of this behavior will depend on the material and projectile species due to angular dependence of the sputter yield (see P. S. Szabo et al. 2022a), which can become very pronounced for systems relevant for solar wind sputtering (e.g., P. S. Szabo et al. 2020a). Under more oblique incidence angles toward the maximum of the angular dependence of a flat surface, the sputter yield continuously decreases, contrary to the behavior of the flat surface (e.g., M. Küstner et al. 1998; R. Arredondo et al. 2019; C. Cupak et al. 2021; P. S. Szabo et al. 2022a). For very rough surfaces with high $\delta_m$ values, secondary sputtering by reflected ions will also contribute to the total sputtering (U. von Toussaint et al. 2017), which is included only for the SPRAY simulations shown in Figure 21. While more studies are still required for conventional rough surfaces as well, it should be considered how advances in this area of research can be used to better describe the sputtering of granular regolith. With several ongoing or planned experimental efforts for studying sputtering from rough and porous planetary analogs (see N. Jäggi et al. 2021b; H. Biber et al. 2022; A. Woodson &
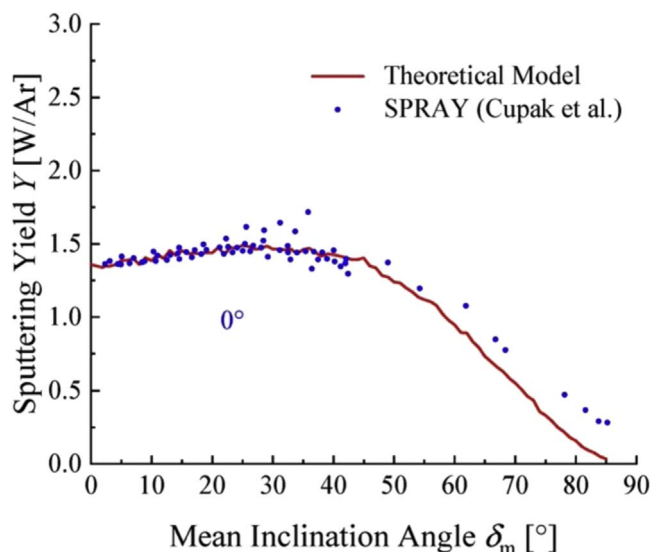
**Figure 21.** Total sputter yield $Y$ for 2 keV $Ar^+$ ions normally incident on a tungsten surface as a function of the mean inclination angle $\delta_m$. The results shown here are from analytical theory (red line, P. S. Szabo et al. 2022a) and are from SPRAY simulations (blue symbols, C. Cupak et al. 2021). The sputter yield $Y$ increases for smaller roughness, before redeposition of the sputtered atoms overtakes and causes the sputter yield to decrease. This image was reproduced from P. S. Szabo et al. (2022a), with permission.

C. Dukes 2022; C. Bu et al. 2024) and the multitude of newly available 3D sputtering codes, the previous findings on sputtering of regolith grains should be revisited and expanded upon. In this context, P. S. Szabo et al. (2022b, 2023) have implemented regolith grain stackings in SDTrimSP-3D to model energetic neutral atom emission from the Moon due to solar wind backscattering from the regolith. This has been shown to reproduce porosity-dependent backscattering yields as well as distributions of emission angles and energies of reflected solar wind protons. However, this has yet to be applied to sputtering from the regolith to better quantify the effects of porosity there.

For future investigations, several key questions that should be addressed become evident:

1. How does the regolith structure affect sputter yields under different incidence angles? Does it also play a role for the angular and energy distributions of sputtered atoms?
2. Which regolith parameters, such as the porosity or the grain shape, play a role in the sputter process?
3. How can the continuously increasing understanding of sputtering of rough surfaces be applied to regolith sputtering, and where do the two scenarios differ?

A key challenge will be the benchmarking of different codes with experimental results. Here, experiments with pressed pellets are important, but irradiation experiments of loose powders should ideally be aimed for as well. An extensive characterization of the samples used should be performed, including the elemental composition as well as roughness or grain shapes and porosity, which provide valuable data on space weathering. All these parameters are relevant to the interaction between ions and the surfaces, and they will affect the sputtering behavior to a certain extent.

## 6. Conclusions

Mercury has a surface-bound exosphere, which can be observed from spacecraft in orbit and by ground-based observatories. A surface-bound exosphere means that the material populating the exosphere originates from the surface, either from the very surface for sputtered particles, or from the upper regolith for some volatiles, or from further below via diffusion and thermal release. The processes that release atoms and molecules from the surface into the exosphere are reasonably well understood (see the review by P. Wurz et al. 2022) as well as diffusion from sources of volatiles below the surface (F. Leblanc et al. 2023). However, the surface itself is the big unknown. To understand the composition of the exosphere, we need to understand the composition of the surface (elemental, mineralogical, relocated material, and others), and the mechanical structure (grain sizes and their distributions, porosity, fractures, and others) as well. Because space weathering of planetary surfaces affects spatial scales ranging from nanometers to kilometers in depth, the composition and structure of planetary surfaces changes with depth as well, and these changes are within the range of sensitivities of the various techniques used for its characterization (see Figure 1). Instruments and measurements based on different physical principles probe different depth ranges; thus, they might "see" a different chemical composition. Moreover, if the coating of the top 10 cm of regolith by thermal activation of Na and K (and possibly S, Mg, and Ca) is correct, we might "see" a volatile-rich surface that is the result of a coating of the regolith.

The MESSENGER mission had a range of instruments to study Mercury's surface from orbit and provided us with a rich data set. For mineralogy investigations, there were the MDIS and MASCS instruments, which revealed a surface with an overall low ultraviolet to near-infrared albedo; however, mineral identifications were not possible because of the lack of diagnostic features in the spectral range covered by these instruments (i.e., M. S. Robinson et al. 2008; N. R. Izenberg et al. 2014; S. L. Murchie et al. 2015). The space-weathering processes on the surface are known to suppress absorption features, to lower reflectance, and to increase the spectral slope (redden the spectrum). This complicates interpretations of spectral data, and for the wavelength range covered by MESSENGER instruments, largely inhibits mineral identifications. The temperature effects on spectral properties add additional complexity to the mineral identification for this surface. Remote sensing investigations using ultraviolet, visible, and infrared spectroscopy receive their spectral information only from the uppermost surface (see Figure 1), which is the weathered surface, and not the unperturbed surface material or crust. This is known as the "astronomers' color problem" (R. A. Kerr 2011). For example, the Hayabusa mission of the Japanese Space Agency brought about 1500 grains of micrometer size from the regolith of asteroid Itokawa to Earth. Their composition analysis clearly showed that the true mineral identity of a grain was masked by a weathering layer on its surface (T. Noguchi et al. 2011), where, below the weathered surface, the composition of these grains was identical to those of thermally metamorphosed LL chondrites (T. Nakamura et al. 2011).

Ground-based measurements of Mercury's surface mineralogy in the infrared wavelength region are difficult because of absorption features within the terrestrial atmosphere, because of

seeing (i.e., atmospheric blurring) and the planet's closeness to the Sun. An additional complication for infrared spectroscopy of Mercury's surface arises from the expected small grain size of the regolith grains on Mercury, approaching the infrared wavelengths, which reduces the spectral contrast (J. Helbert et al. 2007) and which complicates the spectroscopic identification of minerals on the surface. Despite many decades of ground-based infrared spectroscopic observations of Mercury, only a few mineralogical facts of its surface mineralogy are established; see the detailed review by A. Sprague et al. (2007) and the discussion in Section 2.2.1.

The situation should improve greatly with the BepiColombo mission investigating Mercury, starting in 2025 December (J. Benkhoff et al. 2021). For the surface mineralogy, there are two instruments on BepiColombo: the SIMBIO-SYS instrument (visible and near-infrared hyperspectral imaging channel, wavelength range 400–2000 nm; G. Cremonese et al. 2020) and the MERTIS instrument (infrared spectrometer and radiometer, wavelength regions of 7–14 $\mu$m and 7–40 $\mu$m; H. Hiesinger et al. 2020). The increased spectral coverage, increased spectral resolution, and increased spatial resolution of these instruments compared to the MESSENGER instruments should allow for the identification of the mineralogy of Mercury's surface. The SIMBIO-SYS wavelength range allows, for example, to detect sulfides or material derived by sulfur and carbon oxidation at spatial resolutions and spectral coverage higher than the MESSENGER mission. With the wavelength ranges of 7–14 $\mu$m and 7–40 $\mu$m, MERTIS will cover several diagnostic spectral signatures in the mid- and thermal infrared region, the CF, the RB, and the TF, which will enable researchers to identify and map rock-forming silicates and sulfides as well as other minerals. Thus, MERTIS is particularly well suited to study the mineralogy and composition of the Hermean surface, providing a spatial resolution of about 500 m globally and better than 500 m for approximately 5%–10% of the surface. The combination of the two instruments will provide not only mineralogical identifications, but also provide an unprecedented characterization of the extent of both thermal and space-weathering alteration and modification of the regolith.

For the measurement of the chemical composition of the surface, the MESSENGER mission had the GRS, NS, and XRS instruments. These instruments provided the present understanding of the composition of Mercury's surface. BepiColombo has similar instruments for the observation of gamma rays and neutrons, the MGNS, and the MIXS for X-ray imaging. There is also a mass spectrometer for in situ measurements of the chemical composition of the exosphere, the STROFIO instrument, which is part of the SERENA experiment (S. Orsini et al. 2021). Moreover, the MPO of BepiColombo will be in a close and low-eccentricity orbit around Mercury, providing much better observation conditions of the entire surface for infrared spectroscopy by the SIMBIO-SYS and MERTIS instruments and for element maps by the X-ray (MIXS) and gamma-ray (MGNS) instruments. Preparations for the science phase of BepiColombo have started already during the hardware phase, and these plans have been elaborated, for example, for the investigation of the surface composition (D. A. Rothery et al. 2020) and the investigation of the exosphere (A. Milillo et al. 2020).

## ORCID iDs

Peter Wurz ✪ https://orcid.org/0000-0002-2603-1169
Noah Jäggi ✪ https://orcid.org/0000-0002-2740-7965
André Galli ✪ https://orcid.org/0000-0003-2425-3793
Audrey Vorburger ✪ https://orcid.org/0000-0002-7400-9142
Deborah Domingue ✪ https://orcid.org/0000-0002-7594-4634
Paul S. Szabo ✪ https://orcid.org/0000-0002-7478-7999
Johannes Benkhoff ✪ https://orcid.org/0000-0002-4307-9703
Océane Barraud ✪ https://orcid.org/0000-0002-9985-1109
Daniel Wolf Savin ✪ https://orcid.org/0000-0002-1111-6610

## References

Aellig, R. A., Lazarus, A. J., & Steinberg, J. T. 2001, GeoRL, 28, 2767
Andersen, H. H., Stenum, B., Sørensen, T., et al. 1985, NIMPB , 6, 459
Anzures, B. A., Parman, S. W., Milliken, R. E., et al. 2020, GeoCoA, 286, 1
Arredondo, R., Balden, M., Mutzke, A., et al. 2020, NMEne, 23, 100749
Arredondo, R., Oberkofler, M., Schwarz-Selinger, T., et al. 2019, NMEne, 18, 72
Aumayr, F., & Winter, H. 2004, RSPTA, 362, 77
Baragiola, R. A. 2004, RSPTA, 362, 29
Barker, M. K., Chabot, N. L., Mazarico, E., et al. 2022, PSJ, 3, 188
Barraud, O., Besse, S., Doressoundiram, A., et al. 2021, Icar, 370, 114652
Barraud, O., Besse, S., & Doressoundiram, A. 2023, SciA, 9, eadd6452
Barraud, O., Doressoundiram, A., Besse, S., & Sunshine, J. M. 2020, JGRE, 125, e06497
Behrisch, R., & Eckstein, W. 2007, Topics in Applied Physics, Vol. 110 (Berlin: Springer)
Benkhoff, J., Murakami, G., Baumjohann, W., et al. 2021, SSRv, 217, 90
Benninghoven, A. 1975, SurSc, 53, 596
Benninghofen, A., Rüdenauer, F. G., & Werner, H. W. 1987, Secondary Ion Mass Spectrometry (New York: Wiley)
Bennett, C. J., McLain, J. L., Sarantos, M., et al. 2016, JGR, 121, 137
Bennett, C. J., Pirim, C., & Orlando, T. M. 2013, ChRv, 113, 9086
Berezhnoy, A. A. 2010, AdSpR, 45, 70
Berezhnoy, A. A. 2013, Icar, 226, 205
Berezhnoy, A. A. 2018, Icar, 300, 210
Berezhnoy, A. A., & Klumov, B. A. 2008, Icar, 195, 511
Berthet, S., Malavergne, V., & Righter, K. 2009, GeCoA, 73, 6402
Besse, S., Doressoundiram, A., Barraud, O., et al. 2020, JGRE, 125, e2018JE005879
Betz, G., & Husinsky, W. 2004, RSPTA , 362, 177
Betz, G., & Wien, K. 1994, IJMSI , 140, 1
Biber, H., Brötzner, J., Jäggi, N., et al. 2022, PSJ, 3, 271
Biber, H., Szabo, P. S., Jäggi, N., et al. 2020, NIMPB , 480, 10
Biber, H., Szabo, P. S., Jäggi, N., et al. 2021, in 15th Europlanet Science Congress 2021 EPSC2021-526
Bida, T. A., Killen, R. M., & Morgan, T. H. 2000, Natur, 404, 159
Biersack, J. P., & Eckstein, W. 1984, ApPhA , 34, 73
Biersack, J. P., & Haggmark, L. G. 1980, NucIM, 174, 257
Blewett, D. T., Denevi, B. W., Cahill, J. T. S., & Klima, R. L. 2021, Icar, 364, 114472
Blewett, D. T., Ernst, C. M., Murchie, S. L., et al. 2018, Mercury: The View after MESSENGER (Cambridge: Cambridge Univ. Press), 324
Blewett, D. T., Hawke, B. R., Lucey, et al. 2002, M&PS, 37, 1245
Blewett, D. T., Lucey, P. G., Hawke, B. R., et al. 1997, Icar, 129, 217
Blewett, D. T., Robinson, M. S., Denevi, B. W., et al. 2009, E&PSL, 285, 272
Blewett, D. T., Stadermann, A. C., Susorney, H. C., et al. 2016, JGRE, 121, 1798

Blewett, D. T., Vaughan, W. M., Xiao, Z., et al. 2013, JGRE, 118, 1013
Bida, T. A., & Killen, R. M. 2017, Icar, 289, 227
Breen, A. R., Canals, A., Fallows, R. A., Moran, P. J., & Kojima, M. 2002, AdSpR, 29, 379
Britt, D. T., & Pieters, C. M. 1994, GeCoA, 58, 3905
Brezinsek Coenen, J. W., Schwarz-Selinger, T., Schmid, K., et al. 2017, NucFu, 57, 116041
Broadfoot, A. L., Shemansky, D. E., & Kumar, S. 1976, GeoRL, 3, 577
Bruschini, E., Carli, C., Buellet, A.-C., et al. 2022, Icar, 378, 114950
Bu, C., Morrissey, L. S., Bostick, B. C., et al. 2024, JAP, 135, 035302
Burbine, T. H., McCoy, T. J., Nittler, L. R., et al. 2002, M&PS, 37, 1233
Burger, M. H., Killen, R. M., McClintock, W. E., et al. 2012, JGRE, 117, E00L11
Burger, M. H., Killen, R. M., McClintock, W. E., et al. 2014, Icar, 238, 51
Butler, B. J., Muhleman, D. O., & Slade, M. A. 1993, JGR, 98, 15003
Carli, C., Ferrari, S., Maturilli, A., et al. 2024, Mine, 14, 62
Cartier, C., Namur, O., Nittler, L. R., et al. 2020, E&PSL, 534, 116108
Cassidy, T., & Johnson, R. 2005, Icar, 176, 499
Chabot, N. L., Lawrence, D. J., Neumann, G. A., Feldman, W. C., & Paige, D. A. 2018b, in Mercury: The View after Messenger, ed. S. C. Solomon, L. R. Nittler, & B. J. Anderson (Cambridge: Cambridge Univ. Press), 346
Chabot, N. L., Shread, E. E., & Harmon, J. K. 2018a, JGRE, 123, 666
Charlier, B., Grove, T. L., & Zuber, M. T. 2013, E&PSL, 363, 50
Chase, S. C., Jr., Miner, E. D., Morrison, D., et al. 1976, Icar, 28, 565
Choupanian, S., Nagel, A., Möller, W., et al. 2021, Nanot, 33, 035703
Christoph, J. M., Minesinger, G. M., Bu, C., et al. 2022, JGR, 127, e2021JE006916
Cintala, M. J. 1992, JGR, 97, 947
Clark, R. N. 2009, Sci, 326, 562
Coon, S. R., Calaway, W. F., Pellin, M. J., et al. 1993, SurSc, 298, 161
Costello, E. S., Ghent, R. R., Hirabayashi, M., & Lucey, P. G. 2020, JGRE, 125, e2019JE006172
Costello, E. S., Ghent, R. R., & Lucey, P. G. 2018, Icar, 314, 327
Cremonese, G., Capaccioni, F., Capria, M. T., , A., et al. 2020, SSRv, 216, 75
Cross, W., Iddings, J. P., Pirsson, L. V., & Washington, H. S. 1902, JG, 10, 555
Cupak, C., Szabo, P. S., Biber, H., et al. 2021, ApSS, 570, 151204
De Jonge, R., Benoist, K. W., Majoor, J. W. F., et al. 1987, NIMPB, 28, 214
Denevi, B. W., & Robinson, M. S. 2008, Icar, 197, 239
Denevi, B. W., Robinson, M. S., Solomon, S. C., et al. 2009, Sci, 324, 613
Denevi, B. W., Ernst, C. M., Meyer, H. M., et al. 2013, JGRE, 118, 891
Deutsch, A. N., Head, J. W., Chabot, N. L., & Neumann, G. A. 2018, Icar, 305, 139
Deutsch, A. N., Head, J. W., Parman, S. W., et al. 2021, E&PSL, 564, 116907
Doressoundiram, A., Leblanc, F., Foellmi, C., et al. 2009, AJ, 137, 3859
Domingue, D. L., Chapman, C. R., Killen, R. M., et al. 2014, SSRv, 181, 121
Domingue, D. L., Koehn, P. L., Killen, R. M., et al. 2007, SSRv, 131, 161
Donaldson Hanna, K. L., Thomas, I. R., Bowles, et al. 2012, JGRE, 117, E11004
Drobny, J., Hayes, A., Curreli, D., et al. 2017, JNuM, 494, 278
Dukes, C. A., Chang, W-Y., Fama, M., et al. 2011, Icar, 212, 463
Dzurisin, D. 1977, GeoRL, 4, 383
Eckstein, W. 1991, Computer Simulation of Ion-Solid Interactions, Vol. 10 (Berlin: Springer)
Eichhorn, G. 1976, Interplanetary Dust and Zodiacal Light, Vol. 48 (Berlin: Springer), 243
Eichhorn, G. 1978, P&SS, 26, 463
Elphic, R. C., Funsten, I. I. I., Barraclough, H. O., , B. L., et al. 1991, GeoRL, 18, 2165
Englert, P. A. J. 2011, RadAc, 1, 349
Ernst, C. M., Chabot, N. L., & Barnouin, O. S. 2018, JGRE, 123, 2628
Evans, L. G., Peplowski, P. N., McCubbin, F. M., et al. 2015, Icar, 257, 417
Evans, L. G., Peplowski, P. N., Rhodes, E. A., et al. 2012, JGRE, 117, E00L07
Fayet, P., Wolf, J. P., & Wöste, L. 1986, PhRvB, 33, 6792
Fjelbo, G., Kliore, A., Sweetnam, D., et al. 1976, Icar, 29, 439
Frank, E. A., Nittler, L. R., Vorburger, A. H., et al. 2015, LPSC, 46, 1949
Frantseva, K., Nesvorný, D., Mueller, M., et al. 2022, Icar, 383, 114980
Franzreb, K., Wucher, A., & Oechsner, H. 1991, PhRvB, 43, 14396
Gamborino, D., Vorburger, A., & Wurz, P. 2019, AnGeo, 37, 455
Gamborino, D., & Wurz, P. 2018, P&SS, 159, 97
Gibson, E. J., Jr., & Moore, G. W. 1972, LPSC, 3, 2029
Galiano, A., Capaccioni, F., Filacchione, G., & Carli, C. 2022, Icar, 388, 115233
Giletti, B. J., & Shanahan, T. M. 1997, ChGeo, 139, 3
Goldsten, J. O., Rhodes, E. A., Boynton, W. V., et al. 2007, SSRv, 131, 339

Gnaser, H., & Hofer, W. O. 1989, ApPhA, 48, 261
Goettel, K. A. 1988, in Mercury, ed. F. Vilas et al. (Tucson, AZ: Univ. Arizona Press), 613
Grava, C., Killen, R. M., Benna, M., et al. 2021, SSRv, 217, 61
Hamilton, V. E. 2010, ChEG, 70, 7
Hansen, C. S., Calaway, W. F., King, I., B. V., et al. 1998, SurSc, 398, 211
Hansen, C. S., Calaway, W. F., Pellin, M. J., et al. 1999, SurSc, 432, 199
Harmon, J. K. 2007, SSRv, 132, 307
Harmon, J. K., Slade, M. A., & Rice, M. S. 2011, Icar, 211, 37
Hapke, B. 1984, Icar, 59, 41
Hapke, B. 2001, JGR, 106, 10039
Haughton, D. R., Roeder, P. L., & Skinner, B. J. 1974, EcGeo, 69, 451
Hawkins, S. E., Boldt, J. D., Darlington, E. H., et al. 2007, SSRv, 131, 247
Head, J. W., Chapman, C. R., Strom, R. G., et al. 2011, Sci, 333, 1853
Heiken, G. H., Vaniman, D. T., & French, B. M. 1991, Lunar Sourcebook: A User's Guide to the Moon (Cambridge: Cambridge Univ. Press)
Helbert, J., Maturilli, A., & D'Amore, M. 2013, E&PSL, 369, 233
Helbert, J., Moroz, L. V., Maturilli, A., et al. 2007, AdSpR, 40, 272
Hendrix, A. R., Greathouse, T. K., Retherford, et al. 2016, Icar, 273, 68
Hijazi, H., Bannister, M. E., Meyer, H. M., et al. 2014, JGRA, 119, 8006
Hijazi, H., Bannister, M. E., Meyer, H. M., et al. 2017, JGRE, 122, 1597
Hiesinger, H., & Helbert, J. 2010, P&SS, 58, 144
Hiesinger, H., Helbert, J., Alemanno, G., et al. 2020, SSRv, 216, 110
Hunten, D. M., Shemansky, D. E., & Morgan, T. H. 1988, in Mercury, ed. F. Vilas et al. (Tucson, AZ: Univ. Arizona Press), 562
Hobler, G. 1995, NIMPB, 96, 155
Hobler, G. 2013, NIMPB, 303, 165
Hodges, R. R. 1974, JGR, 79, 2881
Holsclaw, G. M., McClintock, W. E., Domingue, D. L., et al. 2010, Icar, 209, 179
Hörz, F., & Cintala, M. 1997, M&PS, 32, 179
Iacovino, K., McCubbin, F. M., Van der Kaaden, K. E., et al. 2023, E&PSL, 602, 117908
Ipavich, F. M., Galvin, A. B., Lasley, S. E., et al. 1998, JGR, 103, 17205
Izenberg, N. R., Klima, R. L., Murchie, S. L., et al. 2014, Icar, 228, 364
Jäggi, N., Gamborino, D., Bower, D. J., et al. 2021a, PSJ, 2, 230
Jäggi, N., Galli, A., Wurz, P., et al. 2021b, Icar, 365, 114492
Jäggi, N., Mutzke, A., Biber, H., et al. 2023, PSJ, 4, 86
Jones, B. M., Aleksandrov, A., Hibbitts, K., et al. 2018, GeoRL, 45, 10959
Johnson, R. 1989, Icar, 78, 206
Kallio, E., & Janhunen, P. 2003, GeoRL, 30, 1877
Katakuse, I., Ichihara, T., Fujita, Y., et al. 1985, IJMSI, 67, 229
Keller, L. P., & McKay, D. S. 1997, GeoCoA, 61, 2331
Kerber, L., Head, J. W., Blewett, D. T., et al. 2011, P&SS, 59, 1895
Kerber, L., Head, J. W., Solomon, S. C., et al. 2009, E&PSL, 285, 263
Kerr, R. A. 2011, Sci, 333, 1081
Killen, R. M. 2002, M&PS, 37, 1223
Killen, R. M., Bida, T. A., & Morgan, T. H. 2005, Icar, 173, 300
Killen, R. M., Cremonese, G., Lammer, H., et al. 2007, SSRv, 132, 433
Killen, R. M., & Hahn, J. M. 2015, Icar, 250, 230
Killen, R. M., & Ip, W-H. 1999, RvGeo, 37, 361
Killen, R. M., Morrissey, L. S., Burger, M. H., et al. 2022, PSJ, 3, 139
Killen, R. M., Potter, A. E., & Morgan, T. H. 1990, Icar, 85, 145
Killen, R. M., Shemansky, D., & Mouawad, N. 2009, ApJS, 181, 351
Klima, R. L., Denevi, B. W., Ernst, C. M., et al. 2018, GeoRL, 45, 2945
Kremer, C. H., Mustard, J. F., & Pieters, C. M. 2023, E&SS, 10, e2023EA002828
Kreslavsky, M. A., Zharkova, A. Y., Head, J. W., & Gritsevich, M. I. 2021, Icar, 369, 114628
Kumar, S. 1976, Icarus, 28, 579
Küstner, M., Eckstein, W., Dose, V., et al. 1998, NIMPB, 145, 320
Küstner, M., Eckstein, W., Hechtl, E., et al. 1999, JNuM, 265, 22
Langevin, Y. 1997, P&SS, 45, 31
Lawrence, D. J., Feldman, W. C., Goldsten, J. O., et al. 2010, Icar, 209, 195
Lawrence, D. J., Feldman, W. C., Goldsten, J. O., et al. 2013, Sci, 339, 292
Lawrence, D. J., Peplowski, P. N., Beck, A. W., et al. 2017, Icar, 281, 32
Lammer, H., Scherf, M., Ito, Y., et al. 2022, SSRv, 218, 15
Leblanc, F., Delcourt, D., & Johnson, R. E. 2003, JGRE, 108, 5136
Leblanc, F., Doressoundiram, A., Schneider, N., et al. 2009, GeoRL, 36, L07201
Leblanc, F., Schmidt, C., Mangano, V., et al. 2022, SSRv, 218, 2
Leblanc, F., Sarantos, M., Domingue, D., et al. 2023, PSJ, 4, 227
Li, G. Z., & Wirz, R. E. 2021, PhRvL, 126, 035001
Liancun, X., Zhizhong, Z., Chunxia, C., & Yang, G. 2017, in Int. Conf. on Progress in Informatics and Computing (PIC), 119
Lindsey, S., & Hobler, G. 2013, NIMPB, 303, 142

Little, R. C., Feldman, W. C., Maurice, S., et al. 2003, JGRE, 108, 5046
Loeffler, M., Dukes, C., & Baragiola, R. 2009, JGRE, 114, E03003
Lucchetti, A., Pajola, M., Galluzzi, V., et al. 2018, JGRE, 123, 2365
Lucchetti, A., Pajola, M., Poggiali, G., et al. 2021, Icar, 370, 114694
Lucey, P. G., & Noble, S. K. 2008, Icar, 197, 348
Lucey, P. G., & Riner, M. A. 2011, Icar, 212, 451
Lyons, J. R. 2008, J. Sulfur Chem., 29, 269
Madey, T. E., Yakshinskiy, B. V., Ageev, V. N., et al. 1998, JGR, 103, 5873
Mangano, V., Milillo, A., Mura, A., et al. 2007, P&SS, 55, 1541
Maturilli, A., Helbert, J., St. John, J. M., et al. 2014, E&PSL, 398, 58
McClintock, W. E., Bradley, E. T., Vervack, R. J., et al. 2008, Sci, 321, 92
McClintock, W. E., & Lankton, M. R. 2007, SSRv, 131, 481
McCoy, T. J., Dickinson, T. L., & Lofgren, G. E. 1999, M&PS, 34, 735
McCoy, T. J., Peplowski, P. N., McCubbin, F. M., & Weider, S. Z. 2018, in
    Mercury: The View after Messenger, ed. S. C. Solomon, L. R. Nittler, &
    B. J. Anderson (Cambridge: Cambridge Univ. Press), 176
McCubbin, F. M., Riner, M. A., Vander Kaaden, K. E., & Burkemper, L. K.
    2012, GeoRL, 39, L09202
McCubbin, F. M., Vander Kaaden, K. E., Peplowski, P. N., et al. 2017, JGRE,
    122, 2053
McLain, J. L., Sprague, A. L., Grieves, G. A., et al. 2011, JGRE, 116, E03007
Merkel, A. W., Cassidy, T. A., Vervack, R. J., Jr, et al. 2017, Icar, 281, 46
Merkel, A. W., Vervack, R. J., , Jr, Killen, R. M., et al. 2018, GeoRL, 45, 6790
Milillo, A., Fujimoto, M., Murakami, G., et al. 2020, SSRv., 216, 93
Milillo, A., Wurz, P., Orsini, S., et al. 2005, SSRv, 117, 397
Möller, W. 2014, NIMPB , 322, 23
Möller, W., & Eckstein, W. 1984, NIMPB, 2, 814
Möller, W., Eckstein, W., & Biersack, J. P. 1988, CoPhC, 51, 355
Morgan, T. H., & Killen, R. M. 1997, P&SS, 45, 81
Morlok, A., Renggli, C., Charlier, B., et al. 2021, Icar, 361, 114363
Moroni, M., Mura, A., Milillo, A., et al. 2023, Icar, 401, 115616
Morrissey, L. S., Schaible, M. J., Tucker, O. J., et al. 2023, PSJ, 4, 67
Morrissey, L. S., Tucker, O. J., Killen, R. M., et al. 2022, ApJL, 925, L6
Morrison, D. 1969, Thermal Models and Microwave Temperatures of the
    Planet Mercury, Special Report 292, Smithsonian Astrophysical
    Observatory
Mura, A., Wurz, P., Lichtenegger, H. I. M., et al. 2009, Icar, 200, 1
Murchie, S. L., Klima, R. L., Denevi, B. W., et al. 2015, Icar, 254, 287
Mutzke, A., Schneider, R., Eckstein, W., et al. 2019, SDTrimSP Version v6.00,
    Max-Planck-Institut für Plasmaphysik, doi:10.17617/2.3026474
Nakamura, T., Noguchi, T., Tanaka, M., et al. 2011, Sci, 333, 1113
Namur, O., Collinet, M., Charlier, B., et al. 2016a, E&PSL, 439, 117
Namur, O., Charlier, B., Holtz, F., et al. 2016b, E&PSL, 448, 102
Namur, O., & Charlier, B. 2017, NatGe, 10, 9
Nash, D. B., & Salisbury, J. W. 1991, GeoRL, 18, 1151
Neumann, G. A., Cavanaugh, J. F., Sun, X., et al. 2013, Sci, 339, 296
Nishijima, D., Baldwin, M., Doerner, R., et al. 2011, JNuM, 415, S96
Nittler, L. R., Boujibar, A., Crapster-Pregont, E., et al. 2023, JGRE, 128,
    e2022JE007691
Nittler, L. R., Starr, R. D., Weider, S. Z., et al. 2011, Sci, 333, 1847
Nittler, L. R., Chabot, N. L., Grove, T. L., & Peplowski, P. N. 2018, in
    Mercury: The View after Messenger, ed. S. C. Solomon, L. R. Nittler, &
    B. J. Anderson (Cambridge: Cambridge Univ. Press), 30
Nittler, L. R., Cartier, C., Charlier, B., et al. 2019, LPSC, 50, 3156
Nittler, L. R., Frank, E. A., Weider, S. Z., et al. 2016, LPSC, 47, 1237
Nittler, L. R., Frank, E. A., Weider, S. Z., et al. 2020, Icar, 345, 113716
Nittler, L. R., & Weider, S. Z. 2019, Eleme, 15, 33
Noble, S. K., Pieters, C. M., & Keller, L. P. 2007, Icar, 192, 629
Noguchi, T., Nakamura, T., Kimura, M., et al. 2011, Sci, 333, 1121
Oechsner, H. 1975, ApPhy, 8, 185
Oechsner, H., Schoof, H., & Stumpe, E. 1978, SurSc, 76, 343
Orsini, S., Livi, S., Lichtenegger, H., et al. 2021, SSRv, 217, 11
Paige, D. A., Siegler, M. A., Harmon, J. K., et al. 2013, Sci, 339, 300
Pajola, M., Lucchetti, A., Semenzato, A., et al. 2021, P&SS, 195, 105136
Pang, R, Li, Y., Li, C., et al. 2024, AcGch, 43, 774
Pegg, D. L., Rothery, D. A., Balme, M. R., & Conway, S. J. 2021, Icar, 365,
    114510
Peplowski, P. N., Evans, L. G., Hauck, I. I., , S. A., et al. 2011, Sci, 333, 1850
Peplowski, P. N., Rhodes, E. A., Hamara, D. K., et al. 2012b, JGRE, 117,
    E00L10
Peplowski, P. N., Evans, L. G., Stockstill-Cahill, K. R., et al. 2014, Icar,
    228, 86
Peplowski, P. N., Klima, R. L., Lawrence, D. J., et al. 2016, NatGe, 9, 273
Peplowski, P. N., Lawrence, D. J., Feldman, W. C., et al. 2015, Icar, 253, 346
Peplowski, P. N., Lawrence, D. J., Rhodes, E. A., et al. 2012a, JGR, 117,
    E00L04

Peplowski, P. N., & Stockstill-Cahill, K. 2019, JGRE, 124, 2414
Pieters, C. M., Goswami, J. N., Clark, R. N., et al. 2009, Sci, 326, 568
Pieters, C. M., & Noble, S. K. 2016, JGRE, 121, 1865
Plog, C., Wiedmann, L., & Benninghoven, A. 1977, SurSc, 67, 565
Potter, A. E., & Morgan, T. H. 1986, Icar, 67, 336
Potter, A. E., & Morgan, T. H. 1997, P&SS, 45, 95
Potter, A. E., Anderson, C. M., Killen, R. M., et al. 2002, JGRE, 107, 5040
Raines, J. M., Dewey, R. M., Staudacher, N. M., et al. 2022, JGR, 127,
    e2022JA030397
Renggli, C. J., & King, P. L. 2018, RvMG, 84, 229
Renggli, C. J., Klemme, S., Morlok, A., et al. 2022, E&PSL, 593, 117647
Riner, M. A., McCubbin, F. M., Lucey, P. G., Jeffrey Talyor, G., &
    Gillis-Davis, J. J. 2010, Icar, 209, 301
Rivera-Valentín, E. G., Meyer, H. M., Taylor, P. A., et al. 2022, PSJ, 3, 62
Robinson, M. T. 1981, Sputtering by Particle Bombardment I (Berlin:
    Springer), 73
Robinson, M. S., Murchie, S. L., Blewett, D. T., et al. 2008, Sci, 321, 66
Robinson, M. S., & Taylor, G. J. 2001, M&PS, 36, 841
Rodriguez-Nieva, J. F., Bringa, E. M., Cassidy, T. A., et al. 2011, ApJL,
    743, L5
Rodriguez, J. A. P., Domingue, D., et al. 2023, PSJ, 4, 219
Rodriguez, J. A. P., Leonard, G. J., Kargel, J. S., et al. 2020, NatSR, 10, 4737
Rothery, D. A., Massironi, M., Alemanno, G., et al. 2020, SSRv, 216, 66
Sarantos, M., & Tsavachidis, S. 2020, GeoRL, 47, e2020GL088930
Sauerbrey, G. 1959, ZPhy, 155, 206
Schaible, M. J., & Baragiola, R. A. 2014, JGRE, 119, 2017
Schaible, M. J., Sarantos, M., Anzures, B. A., et al. 2020, JGR, 125,
    e2020JE006479
Schleicher, H., Wiedemann, G., Wohl, H., et al. 2004, A&A, 425, 1119
Schlemm, C. E., Starr, R. D., Ho, G. C., et al. 2007, SSRv, 131, 393
Schörghofer, N., Benna, M., Berezhnoy, A. A., et al. 2021, SSRv., 217, 74
Serventi, G., Carli, C., Sgavetti, M., et al. 2013, Icar, 226, 282
Shankar, V. 2015, PrEPS, 11, 198
Shemansky, D. E. 1988, MercM, 2, 1
Sigmund, P. 1969, PhRv, 184, 383
Sigmund, P. 2012, TSF, 520, 6031
Smyth, W. H. 1986, Natur, 323, 696
Smyth, W. H., & Marconi, M. L. 1995, APJ, 441, 839
Solomon, S. C., McNutt, R. L., Gold, R. E., et al. 2001, P&SS, 49, 1445
Solomon, S. C., Nittler, L. R., & Anderson, B. J. 2018, Mercury: The View
    after MESSENGER (Cambridge: Cambridge Univ. Press)
Speyerer, E. J., Povilaitis, R. Z., Robinson, M. S., et al. 2016, Natur, 538, 215
Sprague, A., Warell, J., Cremonese, G., et al. 2007, SSRv, 132, 399
Sprague, A. L., Emery, J. P., Donaldson, K. L., et al. 2002, M&PS, 37, 1255
Sprague, A. L., Hunten, D. M., & Grosse, F. A. 1996, Icar, 123, 345
Sprague, A. L., Hunten, D. M., & Lodders, K. 1995, Icar, 118, 211
Sprague, A. L., Kozlowski, R. W. H., & Hunten, D. M. 1990, Sci, 249, 1140
Sprague, A. L., Kozlowski, R. W. H., Hunten, D. M., & Grosse, F. A. 1993,
    Icar, 104, 33
Sprague, Donaldson Hanna, A. L., Kozlowski, K. L., et al. 2009, P&SS,
    57, 364
Stadlmayr, R., Szabo, P. S., Berger, B. M., et al. 2018, NIMPB, 430, 42
Stadlmayr, R., Szabo, P. S., Mayer, D., et al. 2020, JNuM, 532, 152019
Staudt, C., Heinrich, R., & Wucher, A. 2000, NIMPB , 164, 677
Stockstill-Cahill, K. R., Cahill, J. T. S., Domingue, D., Izenberg, N. R., &
    D'Amore, M. 2017, LPSC, 48, 2673
Stockstill-Cahill, K. R., McCoy, T. J., Nittler, L. R., et al. 2012, JGRE, 117,
    E00L15
Strazzulla, G., Dotto, E., Binzel, R., et al. 2005, Icar, 17, 31
Sugita, S., Schultz, P. H., & Hasegawa, S. 2003, JGRE, 108, 5140
Sunshine, J. M., Farnham, T. L., Feaga, L. M., et al. 2009, Sci, 326, 565
Syal, M. B., Schultz, P. H., & Riner, M. A. 2015, NatGe, 8, 352
Szabo, P. S., Biber, H., Jäggi, N., et al. 2020a, ApJ, 891, 100
Szabo, P. S., Biber, H., Jäggi, N., et al. 2020b, JGR., 125
Szabo, P. S., Chiba, R., Biber, H., et al. 2018, Icar, 314, 98
Szabo, P. S., Cupak, C., Biber, H., et al. 2022a, Surfaces and Interfaces, 30,
    101924
Szabo, P. S., Poppe, A. R., Mutzke, A., et al. 2023, JGRE, 128,
    e2023JE007911
Szabo, P. S., Weichselbaum, D., Biber, H., et al. 2022b, NIMPB , 522, 47
Thomas, R. J., Hynek, B. M., Rothery, D. A., & Conway, S. J. 2016, Icar,
    277, 455
Thomas, R. J., & Rothery, D. A. 2019, Eleme, 15, 27
Thomas, R. J., Rothery, D. A., Conway, S. J., & Anand, M. 2014, Icar,
    229, 221
Thomas, G. E., De Kluizenaar, E. E., & Beerlage, M. 1975, ChPhY, 7, 303

Thompson, M. W., Farmery, B. W., & Newson, P. A. 1986, PMag, 18, 361
Trang, D., Lucey, P. G., & Izenberg, N. R. 2017, Icar, 293, 206
Tucker, O. J., Farrell, W. M., Killen, R. M., et al. 2019, JGRE, 124, 278
Udvardi, B., Kovács, I. J., Fancsik, T., et al. 2017, ApSpe, 71, 1157
Valiev, R. R., Berezhnoy, A. A., Gritsenko, I. S., et al. 2020, A&A, 633, A39
Valiev, R. R., Berezhnoy, A. A., Sidorenko, A. D., et al. 2017, P&SS, 145, 38
Vander Kaaden, K. E., & McCubbin, F. M. 2015, JGRE, 120, 195
Vander Kaaden, K. E., & McCubbin, F. M. 2016, GeCoA, 173, 246
Vander Kaaden, K. E., McCubbin, F. M., Byrne, P. K., et al. 2019, SSRv, 215, 49
Vander Kaaden, K. E., McCubbin, F. M., Nittler, L. R., et al. 2017, Icar, 285, 155
Varatharajan, I., Maturilli, A., Helbert, J., Alemanno, G., & Hiesinger, H. 2019, E&PSL, 520, 127
Varenne, O., Fournier, P-G., Fournier, J., et al. 2000, NucIM, 171, 259
Vaughan, W. M., Helbert, J., Blewett, D. T., et al. 2012, LPSC, 43, 1187
Vervack, R. J., Killen, R. M., McClintock, W. E., et al. 2016, GeoRL, 43, 11,545
Vilas, F. 1985, Icarus, 64, 133
Vilas, F., Chapman, C. R., & Matthews, M. S. 1989, Mercury (Tucson, AZ: Univ. Arizona Press)
Vilas, F., Domingue, D. L., Helbert, J., et al. 2016, GeoRL, 43, 1450
von Steiger, R., Schwadron, N. A., Fisk, L. A., et al. 2000, JGR, 105, 27217
von Toussaint, U., Mutzke, A., & Manhard, A. 2017, PhST, T170, 014056
Wade, J., Byrne, D. J., Ballentine, C. J., & Drakesmith, H. 2021, PNAS, 21, e2109865118
Wahl, M., & Wucher, A. 1994, NIMPB, 94, 36
Wang, Y., Xiao, Z., Chang, Y., et al. 2020, JGRE, 125, e2020JE006559
Wang, Y-M. 1994, ApJ, 437, L67
Warell, J., & Blewett, D. T. 2004, Icar, 168, 257
Warell, J., Sprague, A., Kozlowski, R., et al. 2010, Icar, 209, 138
Weider, S. Z., Nittler, L. R., Starr, R. D., McCoy, T. J., & Solomon, S. C. 2014, Icar, 235, 170
Weider, S. Z., Nittler, L. R., Starr, R. D., et al. 2012, JGRE, 117, E00L05
Weider, S. Z., Nittler, L. R., Starr, R. D., et al. 2015, E&PSL, 416, 109
Weider, S. Z., Nittler, L. R., Murchie, S. L., et al. 2016, GeoRL, 43, 3653
Wilbur, Z. E., Udry, A., McCubbin, F. M., et al. 2022, M&PS, 57, 1387
Winslow, R. M., Johnson, C. L., & Anderson, B. J. 2012, GeoRL, 39, L08112
Winslow, R. M., Philpott, L., Paty, C. S., et al. 2017, JGRA, 122, 4960
Woodson, A., & Dukes, C. 2022, LPSC, 2678, 2852
Wright, J., Conway, S. J., Morino, C., et al. 2020, E&PSL, 549, 116519
Wucher, A. 1994, PhRvB, 49, 2012
Wucher, A., & Oechsner, H. 1986, NIMPB , 18, 458
Wucher, A., Staudt, C., Neukermans, S., et al. 2008, NJPh, 10, 103007
Wucher, A., & Wahl, M. 1996, NIMPB, 115, 581
Wucher, A., Wahl, M., & Oechsner, H. 1993, NIMPB, 82, 337
Wurz, P. 2005, in Proc. 11th European Solar Physics Meeting "The Dynamic Sun: Challenges for Theory and Observations" (ESA SP-600), ed. D. Danesy, 44.1
Wurz, P., Fatemi, S., Galli, A., et al. 2022, SSRv, 218, 10
Wurz, P., Gamborino, D., Vorburger, A., et al. 2019, JGRA, 124, 2603
Wurz, P., Husinsky, W., & Betz, G. 1991, ApPhA, 52, 213
Wurz, P., & Lammer, H. 2003, Icar, 164, 1
Wurz, P., Whitby, J. A., Rohner, U., et al. 2010, P&SS, 58, 1599
Xu, R., Xiao, Z., Wang, Y., & Cui, J. 2024, NatAs, 8, 280
Yakshinskiy, B. V., & Madey, T. E. 1999, Natur, 400, 642
Yakshinskiy, B. V., & Madey, T. E. 2000, SuRSc, 451, 160
Yakshinskiy, B. V., & Madey, T. E. 2003, SuRSc, 528, 54
Yakshinskiy, B. V., & Madey, T. E. 2004, Icar, 168, 53
Yakshinskiy, B. V., & Madey, T. E. 2005, SurSc, 593, 202
Yan, N., Chassefière, E., Leblanc, F., et al. 2006, AdSpR, 38, 583
Yasanayake, C. N., Denevi, B. W., Hiroi, T., et al. 2024, JGRE, 129, e2023JE008115
Zeller, E., Dreschhoff, G., & Kevan, L. 1970, ModGe, 1, 141
Zhang, X., Lv, W., Zhang, L., et al. 2021, RemS, 13, 3017
Zharkova, A. Y., Kreslavsky, M. A., Head, J. W., & Kokhanov, A. A. 2020, Icar, 351, 113945
Zolotov, M. Y. 2011, Icar, 212, 24
Zolotov, M. Y., Sprague, A. L., Hauck, S. A., et al. 2013, JGRE, 118, 138
Zurbuchen, T. H., Raines, J. M., Gloeckler, G., et al. 2008, Sci, 321, 90